FORGE

Fate Of Repository Gases

European Commission FP7

The stress-path permeameter experiment conducted on Callovo-Oxfordian Claystone

FORGE Report D5.16

Keywords.

Callov-Oxfordian claystone, argillite, permeability, specific storage, modulus, capillary entry pressure, gas, TPRL.

Bibliographical reference

JF HARRINGTON, DJ NOY & RC Cuss. 2013 Callovo Oxfordian Claystone: processes governing advective gas flow. British Geological Survey Commissioned Report, CR/13/088. EU Report D5.16 82pp.

Euratom 7th Framework Programme Project: FORGE

EURATOM

Fate of repository gases (FORGE)

The multiple barrier concept is the cornerstone of all proposed schemes for underground disposal of radioactive wastes. The concept invokes a series of barriers, both engineered and natural, between the waste and the surface. Achieving this concept is the primary objective of all disposal programmes, from site appraisal and characterisation to repository design and construction. However, the performance of the repository as a whole (waste, buffer, engineering disturbed zone, host rock), and in particular its gas transport properties, are still poorly understood. Issues still to be adequately examined that relate to understanding basic processes include: dilational versus visco-capillary flow mechanisms; long-term integrity of seals, in particular gas flow along contacts; role of the EDZ as a conduit for preferential flow; laboratory to field up-scaling. Understanding gas generation and migration is thus vital in the quantitative assessment of repositories and is the focus of the research in this integrated, multi-disciplinary project. The FORGE project is a pan-European project with links to international radioactive waste management organisations, regulators and academia, specifically designed to tackle the key research issues associated with the generation and movement of repository gasses. Of particular importance are the long-term performance of bentonite buffers, plastic clays, indurated mudrocks and crystalline formations. Further experimental data are required to reduce uncertainty relating to the quantitative treatment of gas in performance assessment. FORGE will address these issues through a series of laboratory and field-scale experiments, including the development of new methods for up-scaling allowing the optimisation of concepts through detailed scenario analysis. The FORGE partners are committed to training and CPD through a broad portfolio of training opportunities and initiatives which form a significant part of the project.

Further details on the FORGE project and its outcomes can be accessed at www.FORGEproject.org.

Contact details:

J.F. Harrington

British Geological Survey
Keyworth
Nottingham
NG12 5GG
UK

Tél.: +441159363100
E-mail: rjfha@bgs.ac.uk

British Geological Survey
NATURAL ENVIRONMENT RESEARCH COUNCIL

Callovo Oxfordian Claystone: processes governing advective gas flow

Minerals and Waste Programme

Commissioned Report CR/13/088

EU Report D5.16

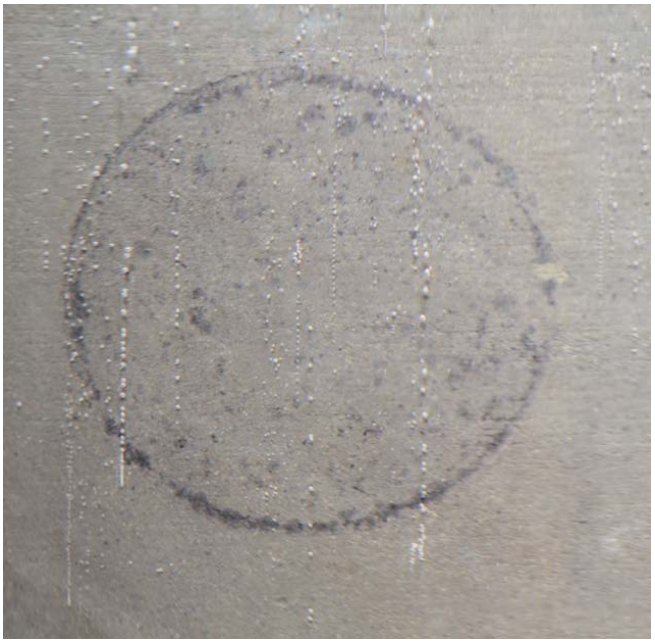

BRITISH GEOLOGICAL SURVEY

MINERALS AND WASTE PROGRAMME

COMMISSIONED REPORT CR/13/088
EU REPORT D5.16

Callovo Oxfordian Claystone: processes governing advective gas flow

JF Harrington, DJ Noy & RJ Cuss

Keywords

Callov-Oxfordian claystone, argillite, permeability, specific storage, modulus, capillary entry pressure, gas, TPRL.

Front cover

Photo of gas discharged from a laboratory sample following gas injection.

Bibliographical reference

JF HARRINGTON, DJ NOY & RC Cuss. 2013 Callovo Oxfordian Claystone: processes governing advective gas flow. *British Geological Survey Commissioned Report*, CR/13/088. EU Report D5.16 82pp.

Copyright in materials derived from the British Geological Survey's work is owned by the Natural Environment Research Council (NERC) and/or the authority that commissioned the work. You may not copy or adapt this publication without first obtaining permission. Contact the BGS Intellectual Property Rights Section, British Geological Survey, Keyworth, e-mail ipr@bgs.ac.uk. You may quote extracts of a reasonable length without prior permission, provided a full acknowledgement is given of the source of the extract.

© NERC2013. All rights reserved

Keyworth, Nottingham British Geological Survey 2013

BRITISH GEOLOGICAL SURVEY

The full range of our publications is available from BGS shops at Nottingham, Edinburgh, London and Cardiff (Welsh publications only) see contact details below or shop online at www.geologyshop.com

The London Information Office also maintains a reference collection of BGS publications, including maps, for consultation.

We publish an annual catalogue of our maps and other publications; this catalogue is available online or from any of the BGS shops.

The British Geological Survey carries out the geological survey of Great Britain and Northern Ireland (the latter as an agency service for the government of Northern Ireland), and of the surrounding continental shelf, as well as basic research projects. It also undertakes programmes of technical aid in geology in developing countries.

The British Geological Survey is a component body of the Natural Environment Research Council.

British Geological Survey offices

BGS Central Enquiries Desk

Tel 0115 936 3143 Fax 0115 936 3276

email enquiries@bgs.ac.uk

Kingsley Dunham Centre, Keyworth, Nottingham NG12 5GG

Tel 0115 936 3241 Fax 0115 936 3488
email sales@bgs.ac.uk

Murchison House, West Mains Road, Edinburgh EH9 3LA

Tel 0131 667 1000 Fax 0131 668 2683
email scotsales@bgs.ac.uk

Natural History Museum, Cromwell Road, London SW7 5BD

Tel 020 7589 4090 Fax 020 7584 8270
Tel 020 7942 5344/45 email bgslondon@bgs.ac.uk

Columbus House, Greenmeadow Springs, Tongwynlais, Cardiff CF15 7NE

Tel 029 2052 1962 Fax 029 2052 1963

Forde House, Park Five Business Centre, Harrier Way, Sowton EX2 7HU

Tel 01392 445271 Fax 01392 445371

Maclean Building, Crowmarsh Gifford, Wallingford OX10 8BB

Tel 01491 838800 Fax 01491 692345

Geological Survey of Northern Ireland, Colby House, Stranmillis Court, Belfast BT9 5BF

Tel 028 9038 8462 Fax 028 9038 8461

www.bgs.ac.uk/gsni/

Parent Body

Natural Environment Research Council, Polaris House, North Star Avenue, Swindon SN2 1EU

Tel 01793 411500 Fax 01793 411501
www.nerc.ac.uk

Website www.bgs.ac.uk
Shop online at www.geologyshop.com

Foreword

This report is the product of a study by the British Geological Survey (BGS) undertaken on behalf of the French radioactive waste management company Agence Nationale pour la Gestion des Déchets Radioactifs (Andra) and the European Union 7th framework Euratom Programme under the auspices of the Fate of repository Gases (FORGE) project, to examine the hydraulic and gas transport properties of the Callovo-Oxfordian argillite.

Acknowledgements

This study was undertaken using the facilities of the BGS Transport Properties Research Laboratory (TPRL) and the Scanning Electron Microscopy Laboratory. Funding for the study was provided by the French radioactive waste management operator, Andra, the European Union (FORGE Project) and the British Geological Survey through its well-founded laboratory programme and the Geosphere Containment project (part of the BGS core strategic programme). The authors would like to thank Dr Jeremy Rushton who undertook the petrographic analysis presented in Section 2.2.1 and Mr Humphrey Wallis and colleagues within the Research & Development Workshops at BGS.

Contents

Foreword i

Acknowledgements i

Contents i

Summary viii

1 Introduction 1
  1.1 Objective of study 1

2 Experimental system 1
  2.1 Test conditions 3
  2.2 Test material 3
  2.3 Calibration 8
  2.4 Experimental procedure 8

3 Data reduction and modelling approaches 8
  3.1 Hydraulic flow 9
  3.2 Gas flow 9

4 Provisional results and numerical modelling 10
  4.1 Callovo-Oxfordian Clay sample 1 (Cox-1) 10
  4.2 Callovo-Oxfordian Clay sample 2 (CoX-2) 43
  4.3 Callovo-Oxfordian Clay sample 3 (CoX-3) 55

5 Modelling of the gas data 64
  5.1 An initial model for sample 1 66

5.2 A model for sample 1 fitted to gas breakthrough at backpressure filter..... 66
5.3 A model for sample 1 fitted to gas outflow rates. 66
5.4 A model for sample 2 fitted to backpressure guard ring arrival time..... 72
5.5 A model for sample COx-2 fitted to injection guard ring arrival time..... 74

6 Implications for process understanding 77

7 References 81

FIGURES

Figure 2-1 Schematic diagram of the pressure vessel and sample assembly for the BGS guard-ring permeameter. The pressure vessel is a custom-built stainless steel vessel rated to 70 MPa. The cylindrical clay specimen is sandwiched between two stainless steel end-caps, each with two filters recessed into the load-bearing surface, and jacketed in heat shrink Teflon to exclude the confining fluid. 2

Figure 2-2 Discing of the core during early attempts to prepare a suitable test plug. As core preparation techniques evolved this problem was virtually eliminated. 4

Figure 2-3. Sub-sampling of the core barrel (by dry cutting using a diamond encrusted blade) prior to preparation of the specimen by diamond coring and surface grinding. 5

Figure 2-4 Photo looking longitudinally along the core showing a number of linear features crossing the core. 6

Figure 2-5 The linear feature is approximately 2mm across, dark grey in the central portion with orange-brown edges. Outside the orange-brown zone is a thin ‘bleached’ zone and outside this the sediment has a slightly darker grey colour for a further 1-2mm. Locally the edge between the dark grey interior and orange-brown zone is marked by a thin white zone. The edges of the dark grey interior are darker grey and iridescent. The box shows the area of the SEM image shown in Figure 2-6. 7

Figure 2-6 The central high brightness portion comprises finely granular iron sulphide (pyrite). The adjacent zones of intermediate brightness correspond to the orange-brown zones and record compositions rich in iron and oxygen (ED analysis), suggesting the presence of iron oxide / hydroxide. The embayment of the central portion suggests that it is the edges of the sulphide that have been altered and dissolved. The box, located on the boundary between these zones, shows the area of the SEM image shown in Figure 2-7. 7

Figure 2-7 Detail of the edge of the iron sulphide (pyrite) inner zone, showing the presence of a thin band of strontium sulphate. This has formed as <10 micron euhedral and subhedral crystals. These are scattered amongst pyrite framboids, in contrast to the densely granulated inner structure of the linear feature.....8

Figure 4-1 Flux response for backpressure and confining circuits during the initial the equilibration stage [1]. Positive flows for red and blue lines represent flux into the specimen. The negative flow for the green line denotes flux out of the pump system suggestive of time dependent swelling. 10

Figure 4-2 Cumulative flow from backpressure and confining systems from test stages [2] and [3]. The backpressure response shows well defined transients associated with drainage of the argillite as confining stress is increased. 12

Figure 4-3 Comparison on model output to test data for the first step of the consolidation test, stage [2]. 14

Figure 4-4 Comparison on model output to test data for the second step of the consolidation test, stage [3]. 14

Figure 4-5 Comparison of observed guard ring pressures with the model simulation of the hydraulic test.....15

Figure 4-6 Comparison of observed flow rates from the injection and back pressure filters with the model simulation of the hydraulic test.....15

Figure 4-7 Comparison of observed guard ring pressures with the model simulation of the hydraulic test, using a model with isotropic clay and leakage over the axial surfaces. 16

Figure 4-8 Comparison of observed flow rates from the injection and back pressure filters with the model simulation of the hydraulic test.....17

Figure 4-9 Pressure data from the injection, backpressure, and guard-ring filters during the gas injection test.....18

Figure 4-10 Gas flow rates at the injection and backpressure filters during the gas injection test. The large spikes in injection flux relate to the compression of the gas phase during constant flow rate test stages.....19

Figure 4-11 Backpressure flow rate and injection gas pressure plotted against elapsed time for test stages [6] through [9]. Note a small but measureable increase in discharge rate following the rise in gas pressure. The rapid increase in flow at around 171.5 days is indicative of major gas breakthrough. 20

Figure 4-12 Backpressure flow rate and injection gas pressure plotted against elapsed time for test stages [6] through [7]. Linear regression of the data suggests flux is decreasing during stage [7]. 21

Figure 4-13 Cross-plot of gas pressure and equivalent hydraulic conductivity versus discharge rate during test stages [6], [7] and the initial section of [9]. Projection of the flux data to the zero flow condition suggests a gas entry pressure of around 0.9 MPa (see Figure 4-14). Equivalent hydraulic conductivities are of a similar magnitude to those observed during hydraulic testing. 22

Figure 4-14 Cross-plot of IGR versus excess injection gas pressure. Extrapolation of the line suggests a gas entry pressure of approximately 1.3 MPa. 23

Figure 4-15 Pressure data from the injection, backpressure, and guard-ring filters during the stage [6]. The asymmetry of the injection guard-ring response observed during the first 12.6 days of the test is atypical of hydraulic behaviour, as is the spontaneous increase in IGR pressure at 12.6 days.....23

Figure 4-16 Pressure from the injection, backpressure, and guard-ring filters during the step-wise increase in pressure from stages [6] to [7]. The rate and shape of the IGR transient is atypical of hydraulic behaviour.....24

Figure 4-17 Evolution of IGR pressure during stage [7]. The spontaneous drops in pressure at days 57 and 78 are symptomatic of unstable pathways flow. 24

Figure 4-18 Evolution of guard-ring pressure during test stage [9]. Correlation lines [i], [ii] and [iii], indicate the start of stage [9], the initiation of the spontaneous negative pressure transient for the IGR filter and the inflection in the IGR pressure curve. 25

Figure 4-19 Evolution of guard-ring pressure during gas breakthrough. Correlation lines [i], [ii] and [iii] relate to increases in filter pressure at the injection and backpressure guard-rings and an increase in discharge rate respectively.....26

Figure 4-20 Cross-plot of flow in and out the sample plotted against excess gas pressure. The intersection of the lines provides an estimate for the gas breakthrough pressure. The hysteresis between ascending and descending flow cycles is evident in the data. 27

Figure 4-21 Flow and strain data from a triaxial test performed on COx (Cuss and Harrington 2012). Plot A shows the slow time dependent evolution in flux out of the core, while plot B, shows the sample dilating in response to changes in gas outflow....28

Figure 4-22 STP flow rate into and out of the specimen during test stage [9]. The inflow data has been cropped during the early part of the test due to problems with leakage from the injection system. 29

Figure 4-23 Evolution of guard-ring pressure during test stage [9]. The dash line indicates the point at which flux out of the specimen increases. The dynamic behaviour exhibited by the backpressure guard-ring can only be explained by the existence of highly unstable gas pathways. 30

Figure 4-24 STP flow rate into and out of the specimen and gas injection pressure plotted against elapsed time during test stage [9] through [15]. 30

Figure 4-25 STP flow rate into and out of the specimen and gas injection pressure plotted against elapsed time during test stage [16] through [19]. 31

Figure 4-26 Downstream guard-ring response during gas testing. The saw-tooth pressure response observed in later data is symptomatic of unstable gas pathways. 31

Figure 4-27 STP flow rates into and out of the sample. The red shaded areas at the beginning of each stage delineate the sections of the transient response used to estimate saturation. 33

Figure 4-28 Cross-plot of excess gas pressure against estimated water saturation based on mass balance. Estimates for the water saturation are derived from mass balance of the STP data presented in Figure 4-27. STP volumes have been corrected back to experimental conditions assuming a capillary threshold pressure of 2.0 MPa. However, the data predicts unrealistically high desaturations which cannot be reconciled with post-test measurements of sample saturation. 34

Figure 4-29 Outflow from backpressure filter and cumulative flow from confining pump (from day 322 onwards) plotted against elapsed time. While the correlation is rather crude the data suggests an underlying trend of volume increase as outflow (and pressure) increase and volume decrease when outflow (and pressure) fall. 34

Figure 4-30 Shut-in response for test COx-1. The protracted nature of the shut-in response is a function of the initial gas volume and the non-linearity in the gas flow law. However, a good numerical fit to the data is obtained allowing a prediction of the capillary threshold pressure to be made.....35

Figure 4-31 Hydraulic response following the initial gas injection cycle. Flow in asymptotes at a value very close to that of the pre-gas injection stage (red line). The offset in the outflow data probably relates to minor leakage. 36

Figure 4-32 Guard ring response during second hydraulic test. While the slow pressurisation of the injection guard ring (IGR) is caused by the presence of residual gas within the filter, the asymptote is very close to the previous value. This suggests little if any change in hydraulic anisotropy. The downstream guard ring pressure (BGR) appears insensitive to the hydraulic gradient with its response probably dominated by the presence of residual gas. 37

Figure 4-33 Comparison of observed guard ring pressures and flow rates with the model simulation of the post-gas injection hydraulic test on sample COx-1. 37

Figure 4-34 Evolution in flow into and out of sample COx-1 to examine self-sealing characteristics of the Callovo Oxfordian Clay during stage [25]. 38

Figure 4-35 Evolution in pressure within sample COx-1 following the reinjection of gas, stage [25]. The inflections in the guar ring response are symptomatic of the opening and closing of unstable gas pathways. 39

Figure 4-36 Evolution in flow into and out of the sample as gas pressure gradient is increased across the sample. 39

Figure 4-37 Evolution in pressure for sample COx-1 from 140 days onwards. Injection pressure guard ring tracks gas pressure while backpressure guard-ring appears insensitive to the change in gas pressure gradient. 40

Figure 4-38 Steady state flow rates plotted against excess gas pressure for both gas injection cycles, stage [6] to [21] and [25] to [27] respectively. 41

Figure 4-39 Out flow and volumetric strain plotted against time. Volumetric strain is estimated from the pre-test volume of the sample (Table 2-1) and the change in confining system volume. Negative strain represents dilation of the sample. 42

Figure 4-40 Volumetric strain plotted against STP flow rate for COx-1 showing a clear correlation between major gas flow and expansion (dilation) of the sample. 42

Figure 4-41 Gas discharged from sample COx-1 following submersion and gentle heating in a glycerol bath. [1] = injection face; [2] = backpressure face. 43

Figure 4-42 Cumulative flow from backpressure system from test stages [1] through [3] for sample COx-2. The backpressure response shows well defined transients associated with drainage of the argillite as confining stress is increased. The cumulative flow data has been edited between day 20 and 31 to correct for a pump problem. 44

Figure 4-43 Comparison on model output to test data for the first step of the consolidation test on sample 2. 45

Figure 4-44Figure 4-44 Comparison on model output to test data for the second step of the consolidation test on sample 2. 45

Figure 4-45 Comparison of observed guard ring pressures with the model simulation of the hydraulic test on sample 2. 46

Figure 4-46 Comparison of observed flow rates from the injection and back pressure filters with the model simulation of the hydraulic test on sample 2. 47

Figure 4-47 Comparison of observed guard ring pressures with a model simulation of the hydraulic test on sample 2 using a two layer representation of the sample. 48

Figure 4-48 Comparison of observed flow rates from the injection and back pressure filters with a two layer model simulation of the hydraulic test on sample 2. 48

Figure 4-49 Plot showing initial slug flow through specimen COx-2 during test stage [6]. 49

Figure 4-50 Plot showing the evolution in guard ring pressures and outflow due to changes in gas pressure gradient. The spike in data observed at around 257 days stems from the failure of the laboratory air conditioning system. However, it is clear from the GR response that this had no permanent effect on the behaviour of the claystone. 50

Figure 4-51 Detailed plot of guard ring and injection pressure evolution as gas begins to migrate through the sample.....50

Figure 4-52 Sample COx-2: material response during gas entry and subsequent breakthrough. Zone index: A = dewatering of IGR filter; A-B = migration of gas across the sample; C = out flow dominated by drainage of water BGR filter; D = as BGR filter is drained of water gas pressure increases; E = gas breakthrough occurs. 51

Figure 4-53 Sample COx-2: Out flow and volumetric strain plotted against time. Volumetric strain is estimated from the pre-test volume of the sample (Table 2-1) and the change in confining system volume. Negative strain represents dilation of the sample. The grey dotted line indicates the point at which confining stress was increased, stage [22]. 52

Figure 4-54 Sample COx-2: material response as gas pressure gradient and thereafter confining pressure are increased. 52

Figure 4-55 Evolution of flow and pressure after gas testing. Positive flux indicates flow out of the sample. Injection and backpressure filter pressures were maintained constant at 4.5 MPa during this stage of testing. 53

Figure 4-56 Cross plot of outflow against backpressure guard ring from day 60 to 120, showing cyclic behaviour between flow and GR pressure as the sample degasses. 54

Figure 4-57 The material components and mesh of the quarter cylinder flow model used for simulation of the hydraulic test for sample COx-3.....56

Figure 4-58 Comparison of an isotropic permeability model with flow data for sample COx-3. 56

Figure 4-59 Comparison of an isotropic permeability model with guard ring pressure data for sample COx-3. 57

Figure 4-60 Comparison of an anisotropic permeability model with flow data for sample COx-3. 57

Figure 4-61 Comparison of an anisotropic permeability model with guard ring pressures for sample COx-3. 58

Figure 4-62 Comparison of an anisotropic permeability model with end surface leakage to flow data for sample COx-3. 58

Figure 4-63 Comparison of an anisotropic permeability model with end surface leakage to guard ring pressures for sample COx-3. 59

Figure 4-64 Comparison of an isotropic permeability model with end surface leakage to flow data for sample COx-3. 59

Figure 4-65 Comparison of an anisotropic permeability model with end surface leakage to guard ring pressures for sample COx-3. 60

Figure 4-66 Evolution in pressure within sample COx-3 and outflow during test stages [6 to 10]. The small emergent flux is symptomatic of a low gas breakthrough pressure. 60

Figure 4-67 Evolution in pressure within sample COx-3 and outflow during test stages [11 to 13]. 61

Figure 4-68 Cyclic behaviour between backpressure guard ring and outflow response indicating pathways formation and closure in response to changes in local gas pressure. 62

Figure 4-69 Cross plot of outflow versus backpressure guard ring from day 225 to 260. The underlying cyclic behaviour between flow and pressure becomes clear, with the arrow indicating the direction of the response. 62

Figure 4-70 Evolution in guard ring pressure and outflow during stage [13], test COx-3. 63

Figure 5-1 The main elements and calculational mesh used for the TOUGH2 models of the gas injection test. Cylindrical symmetry about the z-axis is assumed. ...65

Figure 5-2 Relative permeability data compared to the models presented in sections 5.1, 5.2, and 5.3 below. 65

Figure 5-3 Initial model pressures compared to guard-ring data from sample 1. 67

Figure 5-4 Initial model flow rates compared to the injection and backpressure filter data from sample 1. 68

Figure 5-5 Pressures from a model fitted to the gas breakthrough time at the backpressure filter compared to test data from sample 1. 69

Figure 5-6 Flow rates at the injection and backpressure filters from a model fitted to the gas breakthrough time compared to test data from sample 1.....70

Figure 5-7 Pressures from a model fitted to the gas flow rates at the backpressure filter compared to test data from sample 1. 71

Figure 5-8 Flow rates at the backpressure filter from a model fitted to the gas flow rates compared to test data from sample 1. 72

Figure 6-1 Contour plots of gas saturation (SG) at two times from the model of Section 5.3. 78

Figure 6-2 Axial profiles of gas saturation (S_g) and relative permeability of the gas phase (k_{rg}) at two times from the model of Section 5.3.....79

Figure 6-3 Data from Angeli et al. (2009), showing a significant change in radial strain prior to and during gas breakthrough for a test performed on Draupne shale taken from the Troll East Field in the Norwegian Section of the North Sea. The change in P-wave velocity following breakthrough is symptomatic of gas penetration of the fabric due to the change in compressibility of the CO_2 compared with that of the original porewater. 80

TABLES

Table 2-1 Provisional basic physical properties of the test specimens from pre-test measurements of water content from off-cut material adjacent to the core. An assumed specific gravity for the mineral phases of 2.70 $Mg.m^{-3}$ (Zhang et al. 2007) was used in these calculations. 5

Table 4-1 Experimental history for specimens COx-1 and COx-2 showing the initial test stages. CO = consolidation stage; CPH = constant pressure hydraulic stage; PRH = pressure recovery hydraulic stage; CPG = constant pressure gas stage; CFG = constant flow rate gas stage, PDG = pressure decay gas stage. 11

Table 4-2 Provisional consolidation data for test specimen during test stages [2] and [3]. The start value for void ratio [1] is based on the pre-test measurement. Values for Young's modulus are based on a Poisson's ratio of 0.3 (Wileveau and Bernier, 2008). Values in parentheses are derived from finite element modelling.....12

Table 4-3 Summary of the steady-state gas results for test stages [9] through [27]. Analysis of the flux data indicates breakthrough pressure for initially water saturated conditions in the range 1.9 to 2.2 MPa.....33

Table 4-4 Provisional consolidation data for test specimens COx-1, -2 and -3 during test stages [2] and [3]. The start value for void ratio [1] is based on the pre-test measurement. Values for Young's modulus are based on a Poisson's ratio of 0.3 (Wileveau and Bernier, 2008). Values in parentheses are derived from finite element modelling. Data for test COx-2 and -3 are provisional as testing is on-going at the time of writing. 44

Summary

This report describes the status of an ongoing experimental study to measure the two-phase flow behaviour of the Callovo-Oxfordian argillite from the Bure underground research laboratory (URL) in France. Funding for this study has been provided by the French radioactive waste management operator, Andra, the European Union (FORGE Project) and the British Geological Survey through its well-founded laboratory programme and the Geosphere Containment project (part of the BGS core strategic programme).

The primary objectives of the study are to measure: (i) the hydraulic conductivity and intrinsic (absolute) permeability; (ii) the (threshold) capillary displacement pressure; (iii) the effective gas permeability and relative permeability to gas for a range of conditions; and (iv) the post-test gas saturation. Hydraulic testing was undertaken using a synthetic interstitial fluid. Helium was used in gas testing. Both tests described in part in this document, were performed on specimens orientation perpendicular to the bedding plane.

Cylindrical specimens of Callovo-Oxfordian clay are subject to an isotropic confining stress simulating *in situ* conditions, with fluids injected through the base of the specimen. Initial results are divided into three components: resaturation and consolidation; hydraulic properties (measured using a synthetic interstitial fluid); gas behaviour (using helium, a safe substitute for hydrogen, as the test permeant).

Analysis of the consolidation data based on the total volume of fluid expelled yields reasonable high values for the drained bulk modulus ranging from 1490 MPa to 2262 MPa. This reflects the indurated nature of the material and suggests little, if any, damage has occurred between field sampling and laboratory testing. Commensurate values for Young's modulus were found to range from 1764 MPa to 2629 MPa. Finite element coupled deformation and porewater flow modelling of the consolidation data yielded axial permeabilities ranging from 2.5 to 4.0×10^{-21} m^2, with radial permeability in the range 6.6 to 10.6×10^{-21}. It should be noted that as confining stress increased, axial and radial permeability both decreased slightly. Estimates for specific storage (based on Young's modulus and Poisson's ratio) were found to vary from 7.2×10^{-6} m^{-1} to 8.9×10^{-6} m^{-1}.

Uncoupled finite element porewater flow models were created to simulate the hydraulic tests. It was found that anomalous guard-ring pressures strongly suggest the occurrence of leakage flows across the axial surfaces. The modelling showed that in these circumstances the hydraulic anisotropy could not be reliably determined but good estimates for the axial component of permeability could be obtained. Samples COx-1 and COx-2 yielded values of 1.8×10^{-21} m^2 and 1.6×10^{-21} m^2 respectively for permeability perpendicular to bedding. Sample COx-3 gave a value of 4.5×10^{-21} m^2 for permeability parallel to bedding. Averaging the values from the first two samples gives an estimate of 2.65 for the anisotropy. Specific storage was found to range from 5.4 to 6.0×10^{-6} m^{-1}.

The gas pressure gradient across sample COx-1 was slowly increased in a step-wise manner from 6.5 MPa to 12.0 MPa over a 600 day period. A small emergent flux was noted (common to many tests) during the early stages of testing, which was found to vary with the magnitude of the gas pressure. While analysis of the data suggests this is aqueous in nature, post-test analysis of the sample indicated no measureable desaturation, indicating the fluid was not from the original porosity of the claystone. However, data from COx-2 clearly illustrates slug flow occurred at the onset of gas testing which may account for part of the emergent flux. Displacement of water by gas from the guard ring filters may also contribute to these flows. However, further work is required to differential these potential sources in order to better define the origin of the flux and the initiation of gas breakthrough.

In COx-1, estimates for the gas entry pressure close to the inlet were found to vary between 0.9 MPa and 1.3 MPa. These values are low and probably reflect localised features within the argillite. In contrast data from COx-2 yielded a high gas entry pressure of 5.6 MPa which may be more representative of intact (undamaged) COx material. However, further work is required to confirm this hypothesis. While identifying the gas entry pressure for test COx-3 was not the primary objective, data suggest the gas entry pressure was between 1 and 3 MPa.

The relatively low gas entry values of COx-1 suggest the discrete features are discontinuous and that gas is unable to propagate across the sample. Further increments in pressure were required to initiate gas breakthrough which occurred, in the case of COx-1, between 1.9 and 2.2 MPa.

In all test samples, analysis of flux and pressure data indicates dynamic flow behaviour and time-dependent propagation of gas pathways across the specimens. These pathways appear unstable, evolving both spatially and temporally within the claystone.

Increments in gas pressure clearly show the slow temporal evolution of gas permeability within the specimens, with flux taking from 20 (COx-1) to 250 days (COx-2) to attain a quasi-steady state. These differences may reflect heterogeneities within each sample with 'damaged' material/clay containing conductive features, attaining steady state more quickly than intact material. This time dependency can be explained by time-dependent drainage (porous medium concepts) or pressure induced dilatancy and accompanied drainage, depending on the mechanism invoked. However, spontaneous increases/decreases in both guard-ring pressures and downstream flux occur throughout testing and are difficult to reconcile with standard porous medium concepts and with post-test measurements of desaturation. Initial attempts to define a saturation verses gas pressure function yielded totally unrealistic data.

Triaxial measurements by Cuss and Harrington (2012) clearly measure time-dependent deformation processes occurring in COx during the onset of gas flow. Similar volumetric responses (i.e. increases in sample volume) were observed for all isotropic samples though the magnitude and detail of the response varied between specimens. In both COx-1 and COx-2 data suggests some form of stress relaxation may occur during steady-state, though the cause for this response remains unclear. However, the underlying mechanisms controlling the interaction between the stress state variable (stress, gas and porewater pressure) remains unclear and further work is required to better understand these relationships.

Preliminary mapping of the 'drainage/imbibition' response of the claystone in test COx-1 indicates hysteresis in the flow response between ascending and descending flow histories. Analysis of the post-test saturation for specimen observed no measurable desaturation. As such, the underlying cause for this apparent hysteresis is unclear but may relate to time-dependent processes associated with the creation and subsequent closure of dilatant gas pathways.

Estimates for the apparent capillary threshold value (i.e. the point at which gas ceases to be mobile within the clay), were obtained for test COx-1 by non-linear extrapolation. This yielded a value of around 1.0 MPa, close to the original gas entry pressure.

Measurement of the hydraulic properties after extensive gas testing yielded similar values for hydraulic permeability. However, specific storage was found to increase considerably, probably due to the presence of residual gas.

Repeat gas injection measurements to examine self-sealing behaviour (after hydraulic testing) indicated hysteresis between drainage/imbibition responses was almost nullified by reinjection of water and that under these conditions the previous gas injection history has little permanent impact on the structure and fabric of the clay.

Degassing experiments to examine localisation of gas flow within the core (as inferred by the flux and guard ring pressure responses), indicated a lower density of gas pathways on the injection face compared to that of the backpressure end. Intuitively, this is to be expected and is symptomatic of an expanding network of pathways which fan out as they propagate through the

core. While this method of observation is not fully quantitative, it strongly suggests gas flow is localised within the clay, an observation supported by the non-uniform distribution of flow and the anisotropy in the strain measurements reported by Cuss and Harrington (2012).

Preliminary numerical modelling of the gas data has been undertaken using TOUGH2 and a series of characteristic function parameters based on the van Genuchten formulation. However, initial attempts to model the data in its entirety, have to date, proved elusive. By alteration of the residual saturation and gas permeability functions, it is possible to fit sections of the data to the model predictions. However, this is often to the detriment of other experimental data. Consistent functional fits to the guard-ring pressure responses have not been possible, although fits to discrete sections of the data can be achieved. Following multiple simulations it can be seen that standard porous medium models that reproduce the time of gas breakthrough give flow rates much lower than that observed. In contrast, models that generate flow rates comparable with the data breakthrough much earlier than observed.

While the exact mechanism(s) controlling gas entry and the evolution of permeability within the argillite remain unclear at this stage of testing, the inability of standard porous medium models to adequately describe the data, combined with the complex and time-dependent evolution of parameters observed above, suggest that dilatancy plays a significant role in the movement of gas through the Callovo-Oxfordian argillite. Gas flow appears focused along a localised network of pathways, with no measureable water displacement. Based on the experimental observations, a new conceptual model for gas flow has been developed, where the advective movement of gas is accompanied by measurable dilation of the clay. In these experiments, gas flow is along pressure-induced preferential pathways, where permeability is a dependent variable related to the number, width and aperture distributions of these features.

1 Introduction

Movement of repository gases through argillaceous host rocks will occur by the combined processes of molecular diffusion (governed by Fick's Law) and bulk advection. In the case of a repository for radioactive waste, corrosion of ferrous materials under anoxic conditions will lead to the formation of hydrogen. Radioactive decay of the waste and the radiolysis of water will produce additional gas. If the gas production rate exceeds the rate of diffusion of gas molecules in the pores of the clay barrier, it is possible that a discrete gas phase could form (Horseman et al. 1996; Galle, 2000; Ortiz et al. 2002). Gas would continue to accumulate until its pressure becomes sufficiently large for it to enter the engineered barrier or host rock. There is now a general consensus that in the case of plastic clays and in particular bentonite, classic concepts of porous medium two-phase flow are inappropriate and continuum approaches to modelling gas flow may be questionable depending on the scale of the processes and resolution of the numerical model. The mechanisms controlling gas entry, flow and pathway sealing in general clay-rich media are not yet fully understood. The "memory" of dilatant pathways within a mudrock could impair barrier performance.

To investigate these issues the British Geological Survey (BGS), was approached by the French radioactive waste management company Agence Nationale pour la Gestion des Déchets Radioactifs (Andra), to perform a series of laboratory-scale tests on preserved samples of the Callovo-Oxfordian argillite, a candidate host rock for the storage of radiaoctive waste material in France. This work was undertaken within the auspices of the "Transfert de Gaz" initiative. Funding for the study was provided by Andra and the BGS through its well-founded laboratory programme and the Geosphere Containment project (part of the BGS core strategic programme). This programme of work has now been combined with a second study on gas transfer mechanisms funded through the European Union 7th framework Euratom Programme under the auspices of the Fate of repository Gases (FORGE) project.

1.1 OBJECTIVE OF STUDY

The objective of the proposed study is to define the conditions under which gas (present as a discrete gas-phase) will be mobile in laboratory specimens of Callovo-Oxfordian argillite and quantify the gas entry pressure and the gas permeability of the specimens using a combination of controlled flow rate and constant pressure methodologies. Intrinsic permeability (to a synthetic pore solution) will also be measured. Two flow directions will be examined: (a) parallel to bedding, and (b) normal to bedding. Each experiment will take in excess of one year to complete depending on the complexity of the planned test. A minimum of two tests will be completed during the study.

The primary objectives of this experimental study are to measure:

(a) the hydraulic conductivity and intrinsic (absolute) permeability;

(b) the (threshold) capillary displacement pressure;

(c) the effective gas permeability and relative permeability to gas for a range of conditions;

(d) the post-test gas saturation.

2 Experimental system

The basic permeameter (Figure 2-1) consists of five main components: (1) a specimen assembly, (2) a 70 MPa rated pressure vessel and associated confining pressure system, (3) a fluid injection

system, (4) a backpressure system, and (5) a PC-based data acquisition system. The specimen is subject to an isotropic confining stress, with injection platen mounted on the base of the specimen. A novel feature of the apparatus is the use of porous annular guard-ring filters around the inflow and outflow filters. The pressures in these two guard-rings can be independently monitored. The advantages of the guard-ring approach are: (a) pore pressure evolution can be studied, (b) hydraulic anisotropy can be quantified in a single test, (c) a check can be made of flow symmetry in the specimen, (d) excess gas pressure at gas entry can be determined, and (e) uncertainties associated with possible sheath leakage can be eliminated from data interpretation. Permeants (gas and water) are injected at the base of the specimen to minimise the chance of slug flow during gas testing.

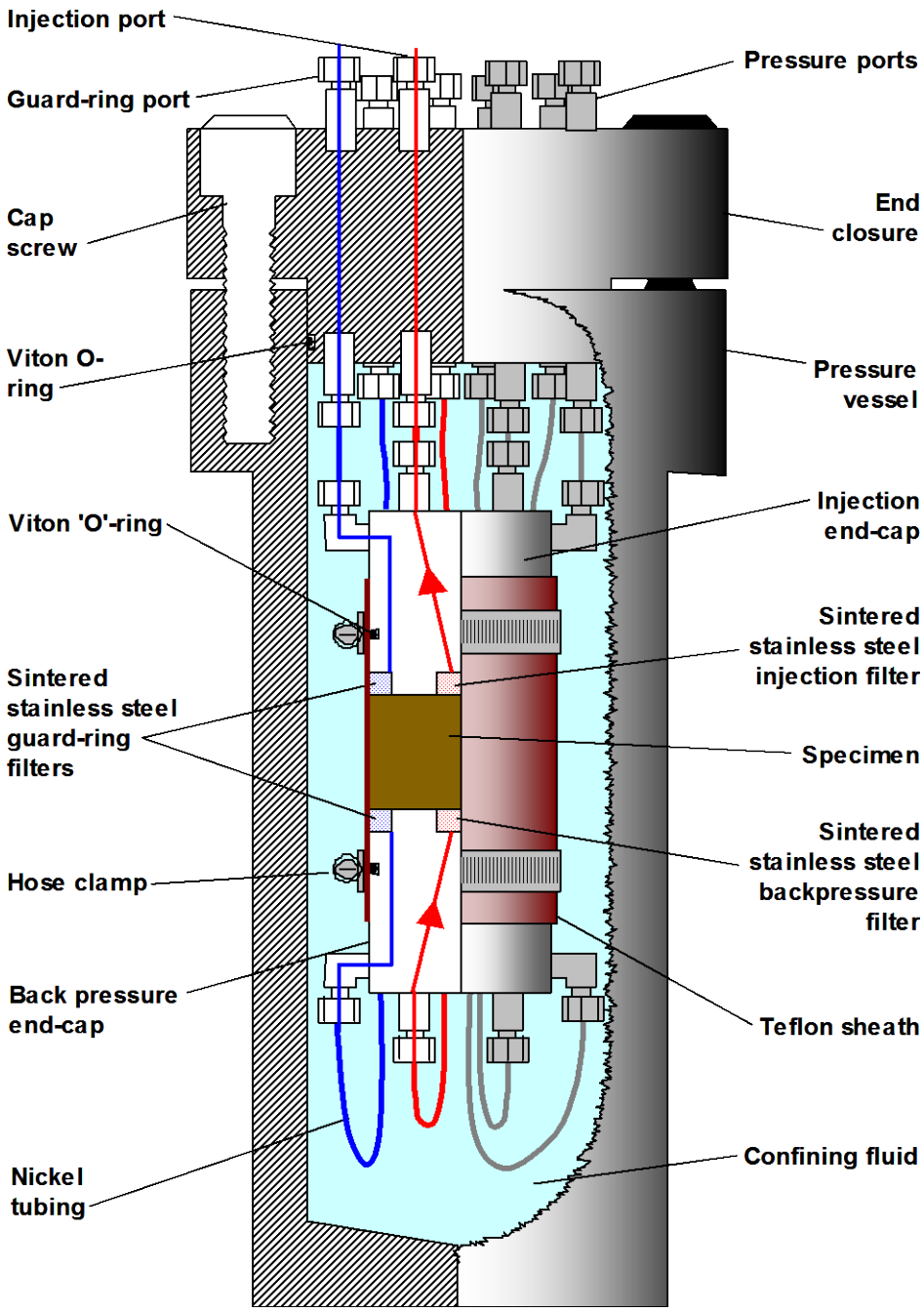

Figure 2-1 Schematic diagram of the pressure vessel and sample assembly for the BGS guard-ring permeameter. The pressure vessel is a custom-built stainless steel vessel rated to 70 MPa. The cylindrical clay specimen is sandwiched between two stainless steel end-caps, each with two filters recessed into the load-bearing surface, and jacketed in heat shrink Teflon to exclude the confining fluid.

The test specimen is sandwiched between two stainless steel end-caps and jacketed in heat-shrink Teflon to exclude confining fluid. Tapered locking rings compress the Teflon against two Viton "O"-rings in each end-cap to provide a leak-tight seal. The inlet and outlet zones for water or gas flow through the specimen are provided by porous filter discs 20 mm in diameter which are recessed into the bearing surface of the end-caps (Figure 2-1). These act as either source or sink for the injection of test permeants. Annular guard-ring filters with an internal diameter of 48.4 mm and an external diameter of 54.4 mm are recessed into the end-caps so that they completely encircle the inlet and outlet filters. A seal between the guard-ring and source/sink filters is achieved through the application of the confining stress, compressing the carefully machined surface of each platen against the clay. During hydraulic measurements, all the filters are saturated with an aqueous porewater solution.

Volumetric flow rates are controlled or monitored using a pair of ISCO-260, Series D, syringe pumps operated from a single digital control unit. The position of each pump piston is determined by an optically encoded disc graduated in segments equivalent to a change in volume of 16.6 nL. Movement of the pump piston is controlled by a micro-processor which continuously monitors and adjusts the rate of rotation of the encoded disc using a DC-motor connected to the piston assembly via a geared worm drive. This allows each pump to operate in either constant pressure or constant flow modes. A programme written in LabVIEW^{TM} elicits data from the pump at pre-set time intervals. Testing is performed in an air-conditioned laboratory at a nominal temperature of 20 ºC. A typical test history comprises a sequence of test stages, each designed to examine a particular system response, as described in Section 2.4.

2.1 TEST CONDITIONS

In order to limit osmotic swelling of the specimen, a synthetic porewater solution was prepared for use as the backpressuring fluid and permeant during hydraulic test stages. Details of the hydrochemistry of the interstitial fluid were provided by Andra. A stock solution comprised of the following components was used as the aqueous test fluid in all hydraulic and consolidation test stages: Ca^{2+} (227 mg l^{-1}); Mg^{2+} (125 mg l^{-1}); Na^{+} (1012 mg l^{-1}); K^{+} (35.7 mg l^{-1}); SO_4^{2-} (1266 mg l^{-1}); S_i (4.59 mg l^{-1}); S_iO^2 (9.83 mg l^{-1}); S_r (13.5 mg l^{-1}); total S (423 mg l^{-1}); total Fe (0.941 mg l^{-1}). ICP-AES analysis of the stock solution was undertaken to verify the fluid composition. This fluid was saturated with fluorescein prior to testing. Post-test analysis of the core will be undertaken to try and identify the location and extent of the fluorescein within the sample. Helium gas (selected as a safe substitute for hydrogen) was used to measure the gas transport properties of the argillite. *In situ* (isotropic) confining stress data was provided by Andra with the initial confining stress nominally set to 12.5 MPa with a backpressure of 4.0 MPa.

2.2 TEST MATERIAL

The composition of the Callovo-Oxfordian argillite (150-160 Ma) can be divided in to three main constituents; clay, silt and carbonate. Wenk et al. (2008) reports these constituents (at the Bure site) as follows; clay 25-55 wt%, 23-44% carbonates and 20-31% silt (essentially quartz + feldspar). Clay minerals are reported to include illite and illite-smectite with subordinate kaolinite and chlorite. In the upper half of the formation the illite-smectite is disordered and contains 50-70% smectite interlayers, whilst in the lower half the illite-smectite is ordered (R=1 type) with lower contents (20-40%) of smectite interlayers (Wenk et al., 2008). Beds can contain common organic matter.

Other authors report compositions similar to these. Wileveau and Bernier (2008) quote values for quartz (18%), calcite (25%), clay minerals (55%; illite-smectite ~65%, illite 30%) and kaolinite and chlorite (2%) with subordinate feldspars, pyrite and iron oxides (2%). Esteban et al. (2006) report 35-60% clay minerals with the remaining shared by calcite and silt. Gaucher et

al. (2004) includes highly detailed mineralogical and chemical compositions of the sequence which are again in broad agreement with the above compositions.

The argillite was deposited under marine basin conditions during a period in which the Paris Basin was variously linked to the Atlantic and Tethyan Oceans, as well as to the London Basin and North Sea (Rousset and Clauer, 2003). Clay sedimentation is therefore considered to have two primary inputs; continental and oceanic. The argillite is over- and underlain by Oxfordian and Bathonian shelf limestones. It is primarily clayey at its base, then becomes increasingly silty and then increasingly calcareous at its top (Gaucher et al., 2004). A maximum clay content zone within the clayey base has been identified; this is interpreted to mark the inflection point (and interval of maximum flooding) from a lower transgressive sequence to an upper regressive sequence (Gaucher et al., 2004).

Upon receipt of the preserved T1-cell core barrels at BGS, the material was catalogued and stored under refrigerated conditions of 4°C (to minimise biological and chemical degradation) ready for future testing. Following several unsuccessful attempts to manufacture a suitable core plug because of discing of the core (Figure 2-2), a test specimen was finally prepared following sub-sampling of the core barrel (Figure 2-3) by a combination of dry core-drilling (with gas flushing and vacuum removal of fines) and diamond slicing. The ends of the sample were then surface ground flat and parallel to minimise “end-effects” during testing. The specimen was accurately measured using a digital micrometer and weighed. The curved surfaces of the specimen were covered with a thin coat of high-purity silicone sealant, providing a good seal between the Teflon sheath and the rock surface. Off-cuts from the coring process were weighed and oven dried to obtain an estimate of moisture content. The dimensions and provisional geotechnical properties of the specimen are given in Table 2-1.

Figure 2-2 Discing of the core during early attempts to prepare a suitable test plug. As core preparation techniques evolved this problem was virtually eliminated.

The initial test specimen, designated COx-1, was cut with the flow direction perpendicular to the bedding, and was taken from drilling core EST27367, dated 10/12/07 from location PAC1011, drilling interval 10.23m to 10.55m. The torque applied to the axial confining system of the T1-cell was around 18 Nm. Table 2-1 shows the preliminary pre-test physical properties of the specimens based on the moisture content of the off-cuts and a grain density of 2.70 Mg m^{-3}

(Zhang et al. 2007). The provisional data presented in Table 2-1 is in fairly good agreement with the generic values quoted by Zhang et al.. However, on the basis of the preliminary numbers for specimen COx-1, the current test sample would appear have a slightly lower porosity than average which is also reflected in the values for dry and bulk density.

A second test specimen was prepared in a similar manner to that described above. The sample was cut perpendicular to bedding from the next 100mm core segment from drilling core EST27367 (location PAC1011). This sample was designated COx-2. A third sample, cut parallel to bedding from core EST30341, was prepared on a machine lathe. The basic geotechnical properties for the material are presented in Table 2-1. The preliminary values obtained for CoX-2 is in line with those reported by Zhang et al. 2007. The minor differences in geotechnical properties between specimens COx-1 and -2 are illustrative of the localised heterogeneity within the Callovo-Oxfordian formation. However, while these small-scale variations in geotechnical properties are of only minor interest, their importance may increase when it comes to the interpretation of hydraulic and gas data.

Figure 2-3 Sub-sampling of the core barrel (by dry cutting using a diamond encrusted blade) prior to preparation of the specimen by diamond coring and surface grinding.

Specimen		Length (mm)	Diameter (mm)	Moisture content (%)	Bulk density (Mg m^{-3})	Dry density (Mg m^{-3})	Porosity (%)	Saturation (%)
COx-1	Pre-test	53.9	54.4	6.1	2.45	2.31	14.6	97
	Post-test	54.1	54.5	6.7	2.44	2.29	15.2	100
COx-2	Pre-test	55.0	54.4	6.6	2.41	2.26	16.5	91
	Post-test	-	-	-	-	-	-	-
COx-3	Pre-test	63.7	54.5	-	-	-	-	-
	Post-test	-	-	-	-	-	-	-
Zhang et al. 2008		-	-	7.7	2.41	2.25	16.8	-

Table 2-1 Provisional basic physical properties of the test specimens from pre-test measurements of water content from off-cut material adjacent to the core. An assumed specific gravity for the mineral phases of 2.70 Mg.m^{-3} (Zhang et al. 2007) was used in these calculations.

2.2.1 Petrographic Analysis of Linear Feature on Fractured Core Surface

Initial attempts to manufacture a suitable test sample were unsuccessful. On a number of failure planes, linear features were noted running through the core (Figure 2-4). An example feature was sent for analysis and the preliminary results of the ongoing study are presented below.

The linear feature is approximately and uniformly 2mm across (Figure 2-5) with a central dark grey portion that comprises finely granular iron sulphide (pyrite). The edges of this central portion are finely embayed and marked by a line of strontium sulphate (celestine) and framboidal pyrite that corresponds to a narrow strip of white-coloured sediment. Outside this the sediment is orange-brown in colour for a thickness of 200-300 microns; this sediment is enriched with iron oxide / hydroxide (Figure 2-6). This outer portion and the sediment beyond still contain iron sulphide in the form of scattered pyrite framboids; the dissolution and alteration of some of these has left scattered rounded pores lined by iron oxide / hydroxide (Figure 2-7).

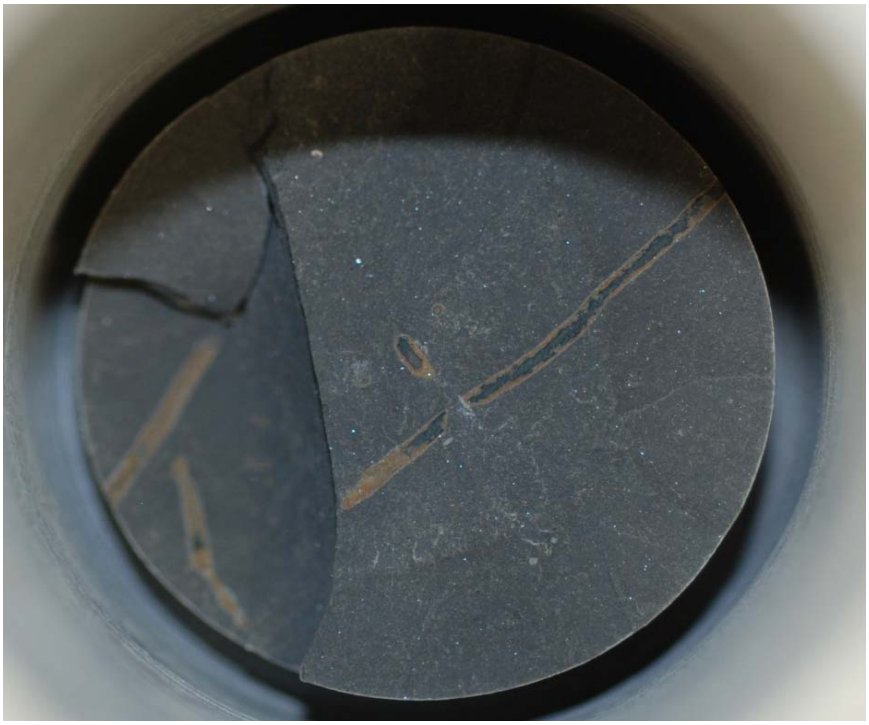

Figure 2-4 Photo looking longitudinally along the core showing a number of linear features crossing the core.

Other off-cuts from the same core contain oval features with cross-sections of 2-3mm with the same sequence of colours. These features were most likely deposited as organic matter, subsequently pyritised. The pyrite has then been partially oxidised along its margins, resulting in the formation of strontium sulphate and iron oxide / hydroxides. The features have a higher porosity than the surrounding sediment, particularly along the oxidation ‘front’ and may provide localised channels of enhanced permeability. Further work will focus on defining the vertical density of the features, on attempting to identify their typical lateral extents and to examine the origin of the oxidisation front.

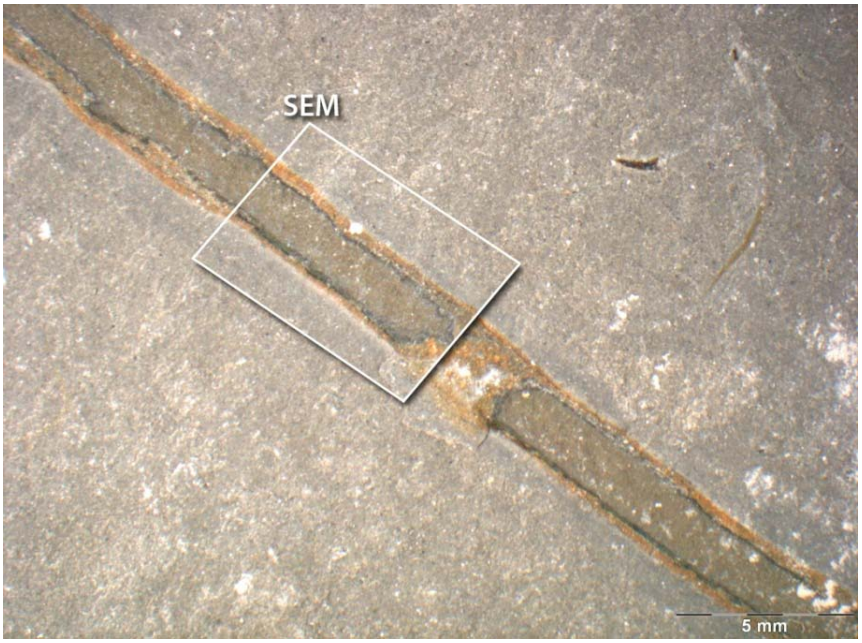

Figure 2-5 The linear feature is approximately 2mm across, dark grey in the central portion with orange-brown edges. Outside the orange-brown zone is a thin 'bleached' zone and outside this the sediment has a slightly darker grey colour for a further 1-2mm. Locally the edge between the dark grey interior and orange-brown zone is marked by a thin white zone. The edges of the dark grey interior are darker grey and iridescent. The box shows the area of the SEM image shown in Figure 2-6.

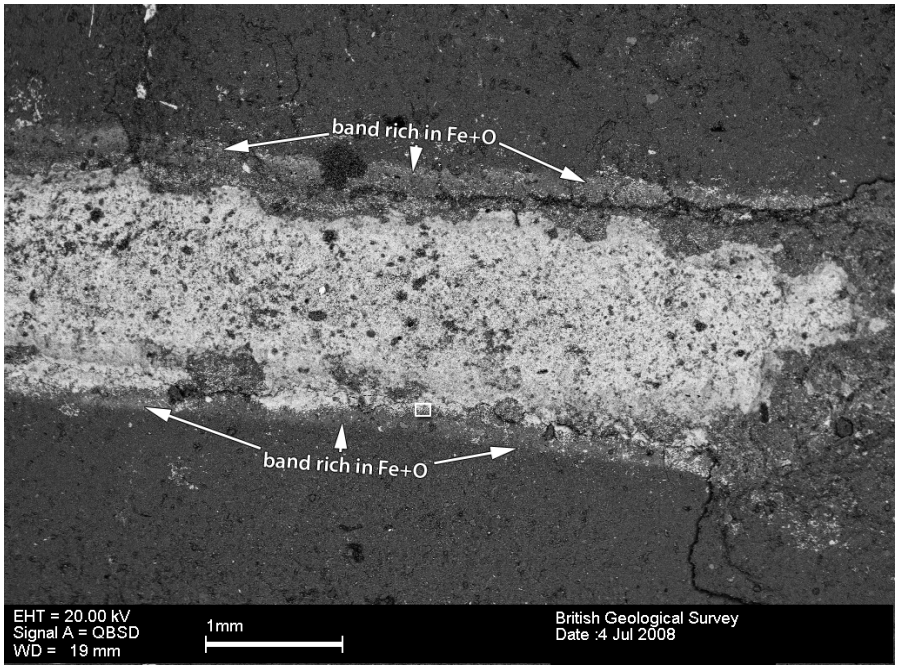

Figure 2-6 The central high brightness portion comprises finely granular iron sulphide (pyrite). The adjacent zones of intermediate brightness correspond to the orange-brown zones and record compositions rich in iron and oxygen (ED analysis), suggesting the presence of iron oxide / hydroxide. The embayment of the central portion suggests that it is the edges of the sulphide that have been altered and dissolved. The box, located on the boundary between these zones, shows the area of the SEM image shown in Figure 2-7.

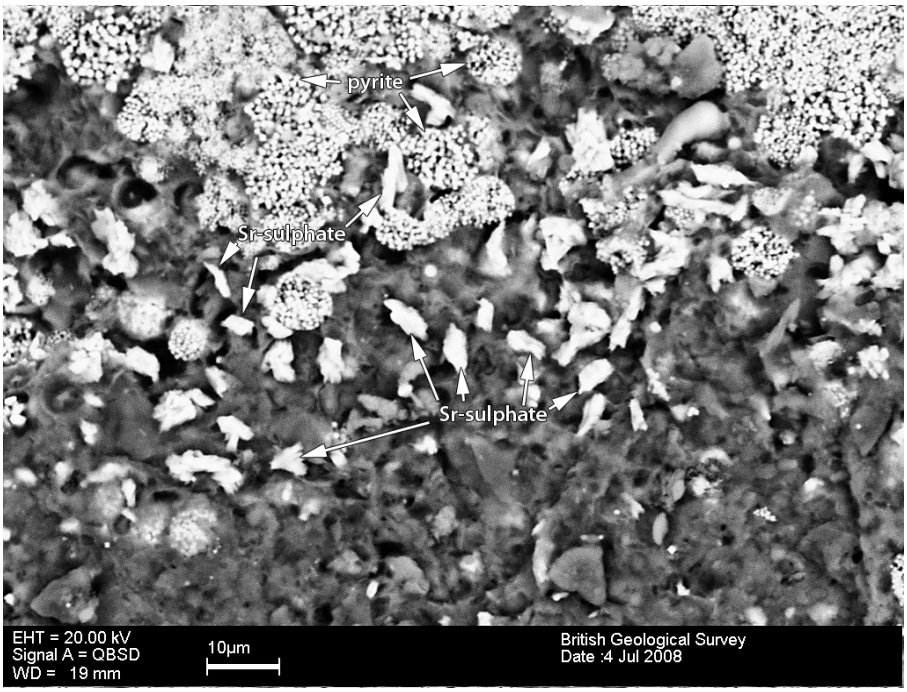

Figure 2-7 Detail of the edge of the iron sulphide (pyrite) inner zone, showing the presence of a thin band of strontium sulphate. This has formed as <10 micron euhedral and subhedral crystals. These are scattered amongst pyrite framboids, in contrast to the densely granulated inner structure of the linear feature.

2.3 CALIBRATION

All pressure sensors were calibrated against laboratory standards by applying incremental steps in pressure, from atmospheric to a pre-determined maximum value. This was followed by a descending sequence to quantify any hysteresis. Least-squares fits were calculated and the regression parameters used to correct raw data.

2.4 EXPERIMENTAL PROCEDURE

An individual test history comprises a sequence of test stages (Table 4-1). A consolidation (CO) stage involves incrementally raising confining pressure and measuring the volume of fluid displaced while backpressure (and injection pressure) are held constant. Constant pressure hydraulic (CPH) and gas (CPG) stages are used to evaluate the intrinsic permeability, specific storage, gas entry and breakthrough pressure, apparent threshold capillary pressure and gas permeability. At the end of hydraulic testing a pressure recovery stage (PRH) allows excess porewater pressures to dissipate (i.e. the injection pump is reset to the backpressure value and the flux and guard-ring pressure response monitored with time). Transient analysis of this data provides an alternative determination of the hydraulic properties. Synthetic groundwater solution is used as the backpressuring fluid in all test stages.

3Data reduction and modelling approaches

Moving average smoothing was applied to all flow data to remove background experimental noise associated with pump switching and minor diurnal variations in temperature.

3.1 HYDRAULIC FLOW

The equation of porewater flow is obtained by combining Darcy's Law with the equation of fluid mass conservation to give (de Marsily, 1986):

$$\frac{S_s}{\rho_w g}\frac{\partial p_w}{\partial t} = \nabla.\left(\frac{k_i}{\mu_w}\left(\nabla p_w + \nabla z\right)\right) + Q \tag{1}$$

where S_s is the specific storage (m^{-1}), k_i is the intrinsic permeability (m^2), ρ_w is the density of water ($kg.m^{-3}$), g is the acceleration due to gravity ($m.s^{-2}$), μ_w is the viscosity of water (Pa.s), p_w is the pore-water pressure (Pa), z is the vertical coordinate (m) and Q is the rate of fluid volume injection per unit volume of porous medium (s^{-1}). This equation is solved here by the finite element method for an axisymmetric two dimensional domain subject to specified head and specified flow boundary conditions. Hydraulic head, h (m), is related to the pore-water pressure by $p_w = \rho_w g(h-z)$.

In order to model the consolidation tests it is necessary to couple the porewater flow equation to equations for the stress-strain relationships. The porewater equation for this takes the form Huyakorn and Pinder (1983):

$$\nabla.\left(\frac{k_i}{\mu_w}\left(\nabla p_w + \rho_w g \nabla z\right)\right) = \phi\beta\frac{\partial p_w}{\partial t} + \frac{\partial}{\partial t}\left(\nabla.\mathbf{u}\right) \tag{2}$$

where ϕ is the porosity, β is the fluid compressibility (Pa^{-1}), and **u** is the vector of solid phase displacements (m). For the case of elastic plane strain, the equations for the displacements are

$$\frac{E}{2(1+\nu)}\nabla^2\mathbf{u} + \frac{E}{2(1+\nu)(1-2\nu)}\nabla\left(\nabla\cdot\mathbf{u}\right) - \nabla p_w = 0 \tag{3}$$

Here E is Young's modulus (Pa) and ν is Poisson's ratio. Equations (2) and (3) are solved using the finite element code STAFAN (Intera, 1983).

3.2 GAS FLOW

The equation for steady state flow of gas as a single phase in a porous medium may be written by combining the mass continuity equation with a generalisation of Darcy's law:

$$\nabla.\left(\frac{\rho_g k_g}{\mu_g}\nabla\left(p_g\right)\right) = 0 \tag{4}$$

where p_g is the gas pressure (Pa), ρ_g is the gas density ($kg.m^{-3}$), $k_g = k_{rg}\, k_i$ is the effective gas permeability (m^2), and μ_g is the gas viscosity (Pa.s). Assuming ideal gas behaviour and a constant value for k_g, equation (4) can be integrated along a 1D flow path to obtain an expression for the flow rate at STP, Q_{st}, in terms of the pressures at either end of the path:

$$Q_{st} = \frac{v_{mst} k_g A}{2RT\mu_g L}\left(p_{gi}^2 - p_{go}^2\right) \tag{5}$$

where v_{mst} is the molar volume of the gas at STP, A is the specimen's cross-sectional area, L is the specimen length, R is the gas constant, T is the absolute temperature, p_{gi} is the gas pressure at injection, and p_{go} the pressure at outlet. Although gas pressure p_{go} cannot be measured directly in these experiments, it can be related to the backpressure of the water at the downstream end of the specimen, p_{wo}, by the relationship $p_{go} = p_{wo} + p_{co}$, where p_{co} is the apparent capillary threshold pressure.

4 Provisional results and numerical modelling

The results and interpretation presented in the following sections are provisional and are subject to alteration once testing is complete.

4.1 CALLOVO-OXFORDIAN CLAY SAMPLE 1 (COX-1)

4.1.1 Consolidation behaviour

Following assembly of the apparatus an initial equilibration period of 15 days was applied to the specimen, with confining and backpressure both held constant at 9.5 MPa and 4.5 MPa respectively. During this time, flux into and out of the specimen were monitored to provide data on the resaturation of the clay (Figure 4-1). Simultaneously, changes in hydraulic volume of the confining system were also monitored to provide an estimate for the volume change of the specimen during hydration.

Examination of the data in Figure 4-1 clearly shows that at the onset of testing, a rapid uptake of water by the specimen is observed as the sample resaturates. This flux progressively declines with time, such that by around 12 days, the net flow of water into the specimen is practically zero. A similar, but less prominent response is also observed by the confining pressure pump, which indicates an increase in specimen volume as a result of time dependent swelling of the argillite. Comparison of the cumulative flow curves from the backpressure and confining systems indicate changes in volume of 1.72 ml and -0.56 ml respectively (the minus sign denoting swelling of the argillite). This suggests the net volume change due to resaturation of the clay is around 1.16 ml during stage [1]. This is in close agreement with pre-test measurements of saturation (Table 2-1), suggesting the bulk of the gas phase was resident in non-dilatant pores and that the specimen was in a good state of preservation at the time of emplacement.

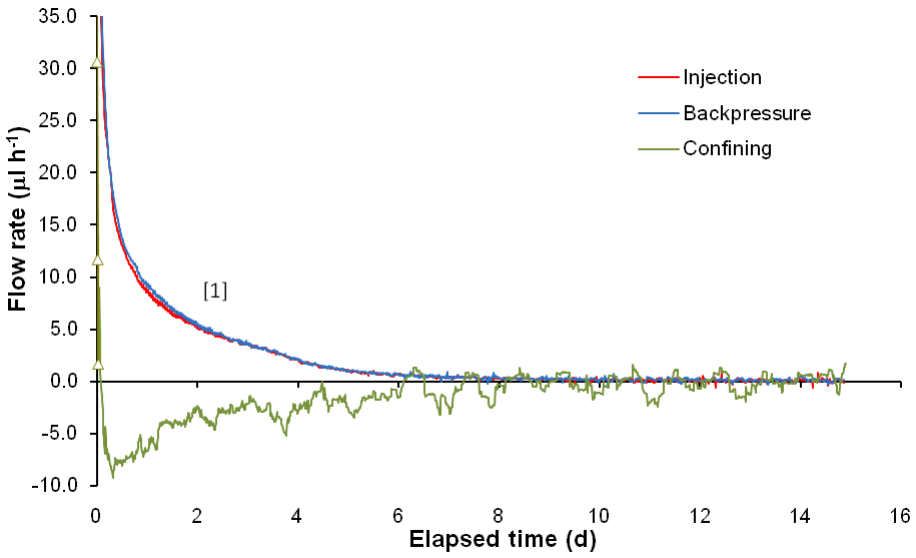

Figure 4-1 Flux response for backpressure and confining circuits during the initial the equilibration stage [1]. Positive flows for red and blue lines represent flux into the specimen. The negative flow for the green line denotes flux out of the pump system suggestive of time dependent swelling.

Stage no.	Specimen COx-1				Specimen COx-2				Specimen COx-3			
	Type	Confining pressure	Injection pressure	Back pressure	Type	Confining pressure	Injection pressure	Back pressure	Type	Confining pressure	Injection pressure	Back pressure
1	CO	9.5	4.5	4.5	CO	9.5	4.5	4.5	CO	9.5	4.5	4.5
2	CO	11.0	4.5	4.5	CO	11.0	4.5	4.5	CO	11.6	4.5	4.5
3	CO	12.5	4.5	4.5	CO	12.5	4.5	4.5	CO	12.5	4.5	4.5
4	CPH	12.5	7.5	4.5	CPH	12.5	7.5	4.5	CPH	12.5	7.5	4.5
5	PRH	12.5	4.5	4.5	PRH	12.5	4.5	4.5	PRH	12.5	4.5	4.5
6	CPG	12.5	6.5	4.5	CPG	12.5	7.5	4.5	CPG	12.5	4.5	4.5
7	CPG	12.5	7.0	4.5	CFG	12.5	7.5 to 8.0	4.5	CFG	12.5	4.5 to 5.5	4.5
8	CFG	12.5	7.0 to 7.5	4.5	CPG	12.5	8.0	4.5	CPG	12.5	5.5	4.5
9	CPG	12.5	7.5	4.5	CFG	12.5	8.0 to 8.5	4.5	CFG	12.5	5.5 to 7.5	4.5
10	CFG	12.5	7.5 to 8.0	4.5	CPG	12.5	8.5	4.5	CPG	12.5	7.5	4.5
11	CPG	12.5	8.0	4.5	CFG	12.5	8.5 to 9.0	4.5	CPG	12.5	7.5	6.5
12	CFG	12.5	8.0 to 8.5	4.5	CPG	12.5	9.0	4.5	CPG	12.5	9.5	6.5
13	CPG	12.5	8.5	4.5	CFG	12.5	9.0 to 9.5	4.5	CPG	12.5	9.5	8.5
14	CFG	12.5	8.5 to 9.0	4.5	CPG	12.5	9.5	4.5				
15	CPG	12.5	9.0	4.5	CFG	12.5	9.5 to 10.0	4.5				
16	CFG	12.5	9.0 to 10.5	4.5	CPG	12.5	10.0	4.5				
17	CPG	12.5	10.5	4.5	CFG	12.5	10.0 to 10.5	4.5				
18	CFG	12.5	10.5 to 12.0	4.5	CPG	12.5	10.5	4.5				
19	CPG	12.5	12.0	4.5	FG	12.5	10.5 to 11.3	4.5				
20	CPG	12.5	9.0	4.5	CPG	12.5	11.3	4.5				
21	CPG	12.5	7.0	4.5	CPG	12.5	12.3	4.5				
22	PDG	12.5	-	4.5	CPG	15.0	12.3	4.5				
23	CPH	12.5	7.5	4.5	CPH	15.0	4.5	4.5				
24	PRH	12.5	4.5	4.5								
25	CGP	12.5	7.5	4.5								
26	CFG	12.5	7.5 to 12.0	4.5								
27	CPG	12.5	12.0	4.5								
	Test complete											

Table 4-1 Experimental history for specimens COx-1 and COx-2 showing the initial test stages. CO = consolidation stage; CPH = constant pressure hydraulic stage; PRH = pressure recovery hydraulic stage; CPG = constant pressure gas stage; CFG = constant flow rate gas stage, PDG = pressure decay gas stage.

Once the equilibration stage was complete a two-step consolidation test was then performed. In the first step, stage [2], the confining pressure was raised to 11 MPa for 5 days and in the second step, stage [3], it was raised to 12.5 MPa for 8 days. Instantaneous flow rate and net cumulative flow volume data were collected (Figure 4-2), with the latter equating to volumetric strain. Inspection of the data show well defined transient responses for the backpressure system for each increment in confining stress. A similar response is noted for net flow out of the confining system though the transients here are less well defined, due to the mixed composition (gas and water) and large fluid volume of the confining system.

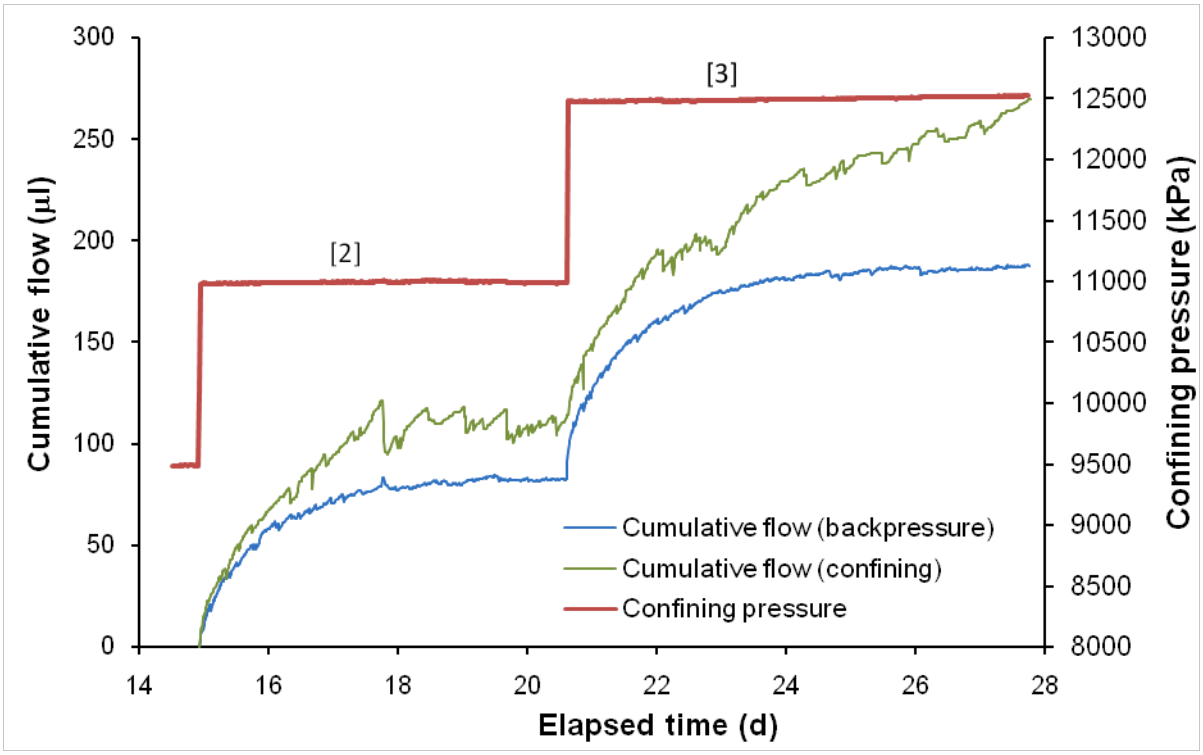

Figure 4-2 Cumulative flow from backpressure and confining systems from test stages [2] and [3]. The backpressure response shows well defined transients associated with drainage of the argillite as confining stress is increased.

Stage no.	Ave. effective stress (MPa)	Void ratio (at end of stage)	Volumetric strain (%)	Drained compressibility $\beta/10^{10}$ (Pa^{-1})	Drained bulk modulus (MPa)	Young's modulus (MPa)
1	5.0	0.175	-	-	-	-
2	6.5	0.174	0.07	4.4	2262	2629 [1825]
3	8.0	0.173	0.16	6.4	1574	1870 [1700]

Table 4-2 Provisional consolidation data for test specimen during test stages [2] and [3]. The start value for void ratio [1] is based on the pre-test measurement. Values for Young's modulus are based on a Poisson's ratio of 0.3 (Wileveau and Bernier, 2008). Values in parentheses are derived from finite element modelling.

Analysis of the consolidation data based on the total volume of fluid expelled from the specimen at the end of each step is presented in Table 4-2. Following each increment in confining stress the specimen exhibits a very small reduction in volume. Values for drained bulk modulus are therefore reasonably high, ranging from 1574 MPa to 2262 MPa, reflecting the indurated nature of the material. These values suggest that the specimen has not suffered significant damage from de-stressing during sampling, transportation and specimen preparation. Young's modulus values were found to range from 1870 MPa to 2629 MPa.

A finite element coupled deformation and porewater flow model of the experimental configuration was created to simulate the test. The two steps were found to differ slightly in the parameters required to best fit the data and so have been interpreted separately. The hydraulic anisotropy obtained from the hydraulic tests of all three samples discussed below (2.65:1 radial to axial) has been maintained for these models and a Poisson's ratio of 0.3 (Wileveau and Bernier, 2008) has been used throughout. The value of the Young's modulus was adjusted to fit to the magnitude of the net flow volume in each step whilst the permeability was adjusted to fit the transients.

The first step was fitted using an axial permeability of 4.0×10^{-21} m^2, a radial permeability of 1.06×10^{-20} m^2, and a Young's modulus of 1825 MPa. This value is significantly lower than that derived from the volumetric strain data, though the reason for this is unclear at present. It may be noted that the Young's modulus, E, and Poisson's ratio, ν, can be related to the solid phase compressibility, α, and the specific storage, S_s, by (de Marsily, 1986):

$$\alpha = \frac{3(1-2\nu)}{E} \tag{6}$$

and:

$$S_s = \rho g(\alpha + \phi\beta_l) \tag{7}$$

where ρ is the porewater density, g the acceleration due to gravity, ϕ the porosity, and β_l the compressibility of the porewater. From these equations it is found that a Young's modulus of 1825 MPa corresponds to a specific storage of 7.2×10^{-6} m^{-1}, slightly more than the value found from the hydraulic test. Figure 4-3 compares output from this model with the data from the test.

The second step was fitted using an axial permeability of 3.4×10^{-21} m^2, a radial permeability of 9.0×10^{-21} m^2, and a Young's modulus of 1700 MPa. This corresponds to a specific storage of 7.7×10^{-6} m^{-1}. Figure 4-4 compares output from this model with the data from the test. It appears that the permeability reduces slightly with the increase in confining pressure, and that there is a further small reduction when the hydraulic test is conducted.

4.1.2 Hydraulic test

For the hydraulic test the confining pressure was maintained at a constant level of 12.5 MPa whilst the porewater pressure at the back pressure filter was kept at 4.5 MPa. The pressure at the injection filter was raised to 7.5 MPa for 7.6 days after which it was returned to 4.5 MPa. Flows at injection and backpressure filters were monitored together with the pressures at the two guard rings. The pressure at the backpressure guard ring did not rise from that of the backpressure filter. This behaviour could potentially be the result of some degree of leakage across the axial surfaces of the samples during the experiment and additional models exploring this option are discussed below. A finite element porewater flow model of the experimental configuration was created to simulate the test and it was found that a good fit to the data could be obtained by setting axial permeability to 1.8×10^{-21} m^2 and radial permeability to 4.5×10^{-20} m^2. The latter value is difficult to reconcile with direct measurements of permeability parallel to bedding presented in Section 4.3.2. A specific storage of 5.4×10^{-6} m^{-1} was used to obtain a reasonable fit to the transients, although the injection guard ring pressure data just after each step change are

not well represented. Increasing the specific storage does improve these early time fits at the expense of poorer late time fits and poorer fits to the flow rate data. Figure 4-5 and Figure 4-6 show comparisons of the model output with these parameters to the data for guard ring pressures and filter flow rates respectively.

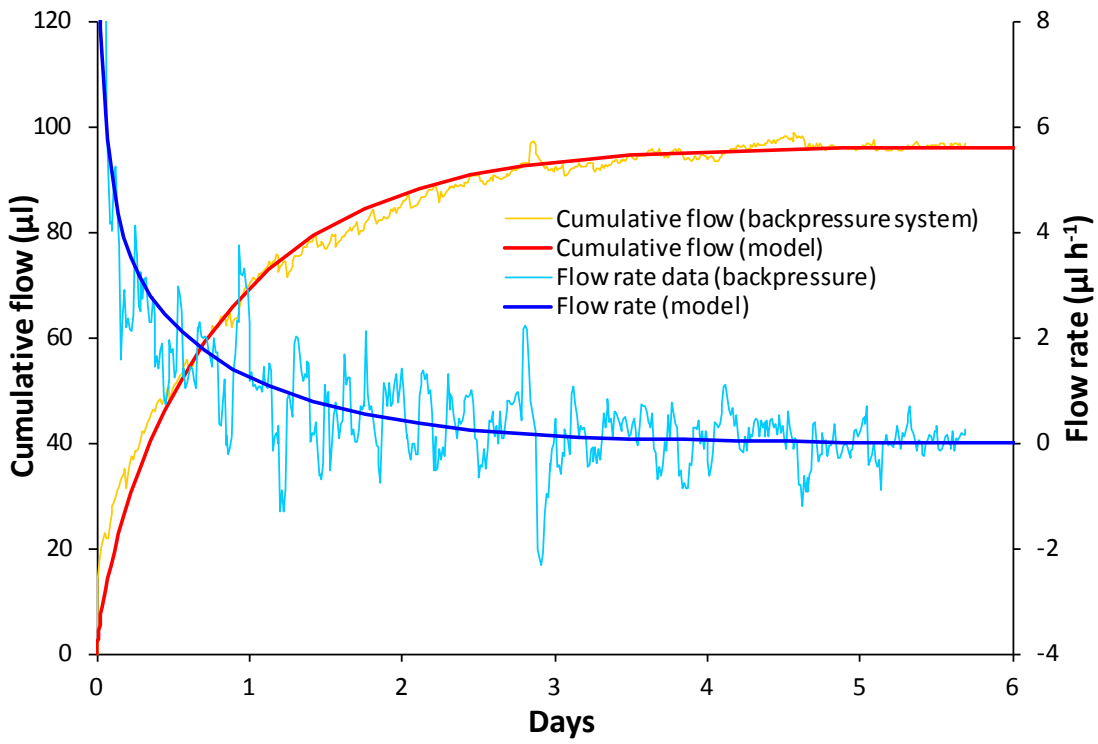

Figure 4-3 Comparison on model output to test data for the first step of the consolidation test, stage [2].

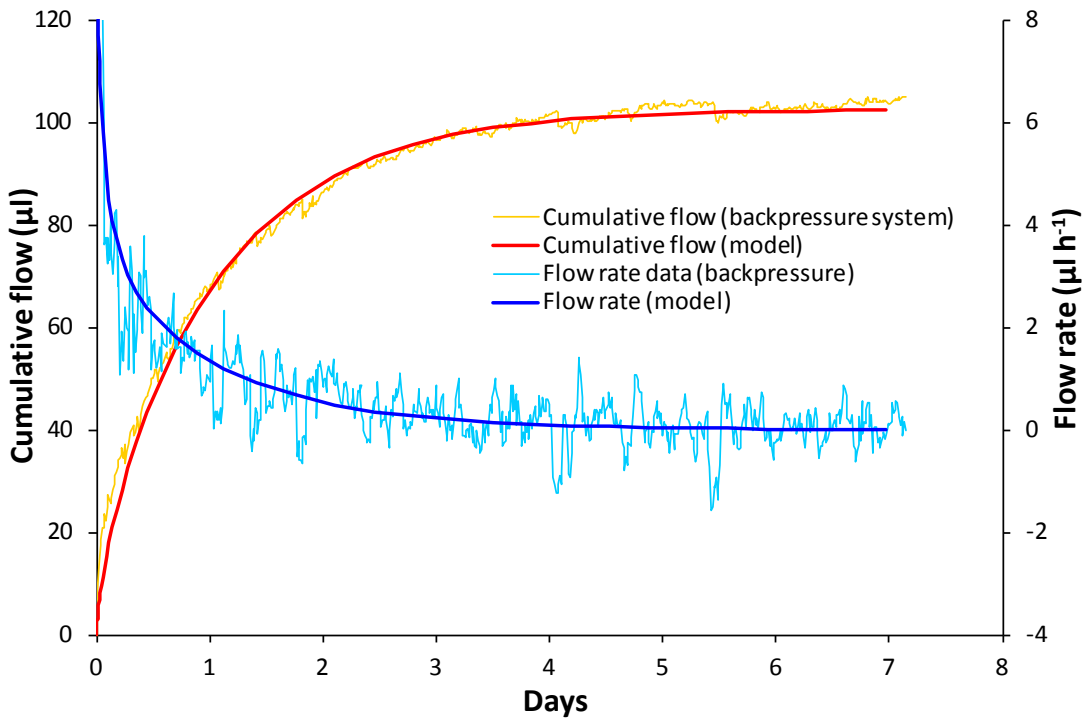

Figure 4-4 Comparison on model output to test data for the second step of the consolidation test, stage [3].

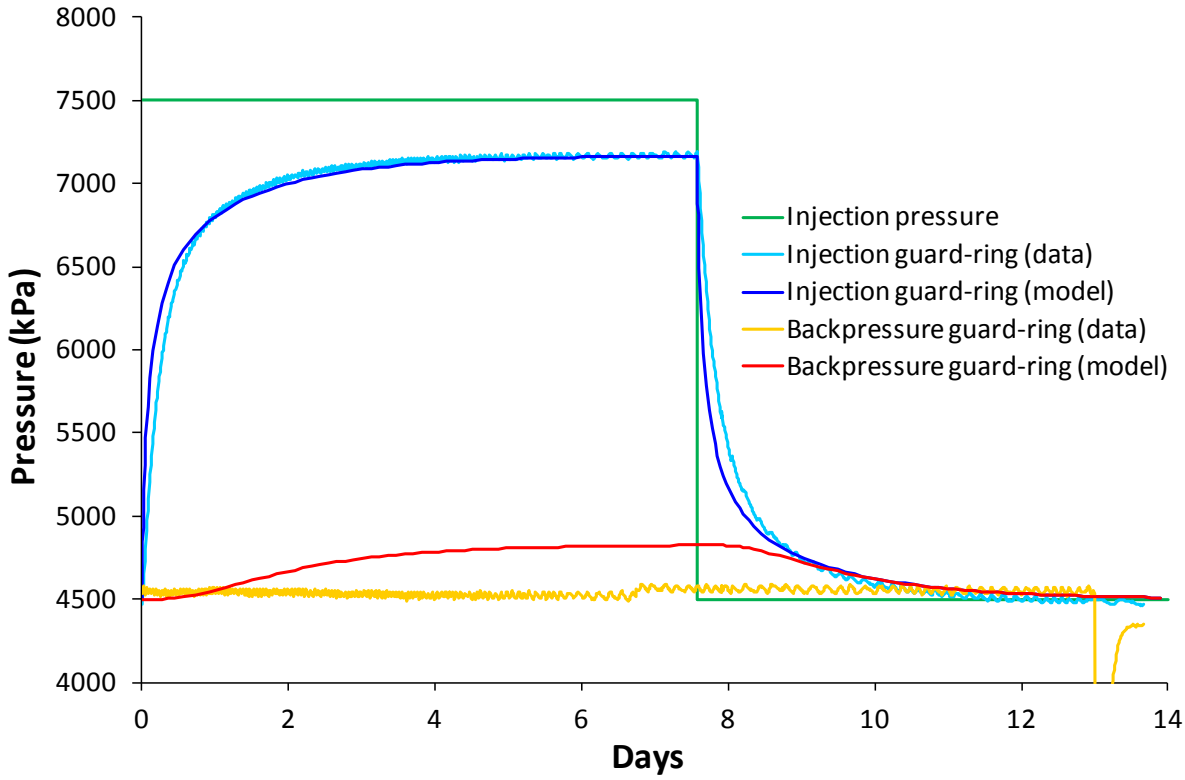

Figure 4-5 Comparison of observed guard ring pressures with the model simulation of the hydraulic test.

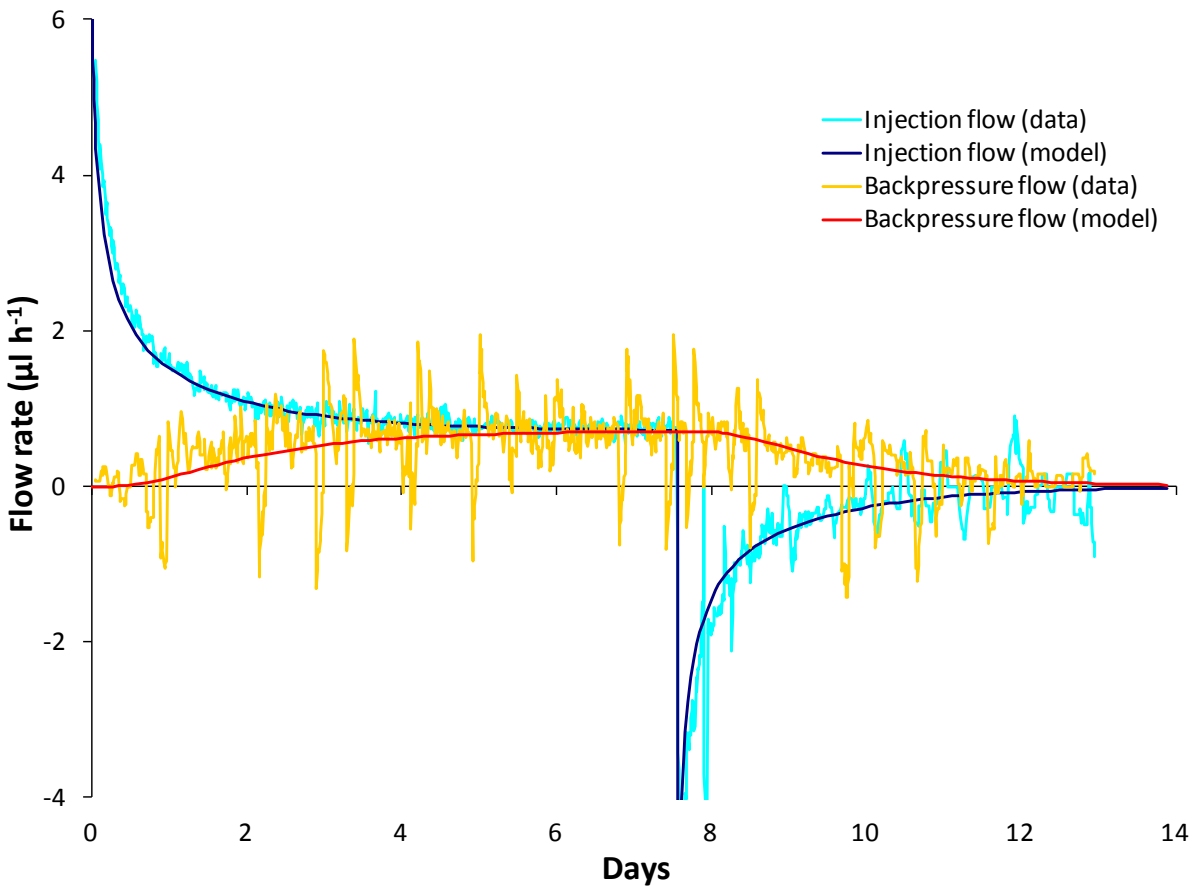

Figure 4-6 Comparison of observed flow rates from the injection and back pressure filters with the model simulation of the hydraulic test.

As noted above, the lack of any change in pressure at the backpressure guard-ring potentially indicates the occurrence of leakage over the surface of the sample. Similarly, the high degree of anisotropy required to explain the injection guard-ring pressures may also indicate some leakage over this surface too. To examine this possibility a second model was run in which elements between injection / backpressure filters and their respective guard-rings are given enhanced permeabilities, whilst the clay was set to an isotropic permeability of 1.8×10^{-21} m^2.

Figure 4-7and Figure 4-8 show that a good fit to the data, including the backpressure guard-ring pressures, can be obtained from this model. In this model the transmissivity (product of hydraulic conductivity and thickness) of the injection end surface is 5.0×10^{-16} m^2s^{-1} and of the backpressure end surface is 5.0×10^{-15} m^2s^{-1}. Further runs of this model with anisotropic permeabilities for the clay up to an anisotropy of 10 show that essentially identical results can be obtained with small adjustments to the transmissivity of the injection surface. Thus, for this model the anisotropy of the clay is undetermined in the absence of any independent information about the transmissivity of the axial surfaces. The estimate of axial permeability does appear to be robust however.

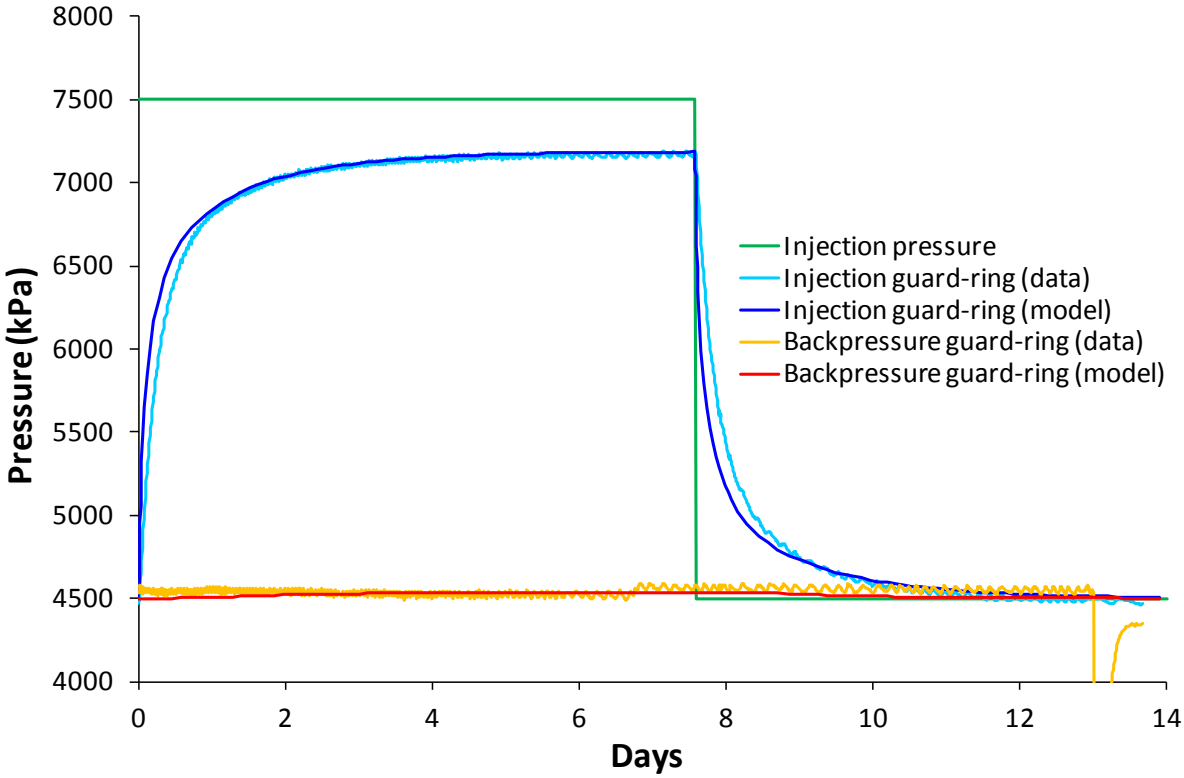

Figure 4-7 Comparison of observed guard ring pressures with the model simulation of the hydraulic test, using a model with isotropic clay and leakage over the axial surfaces.

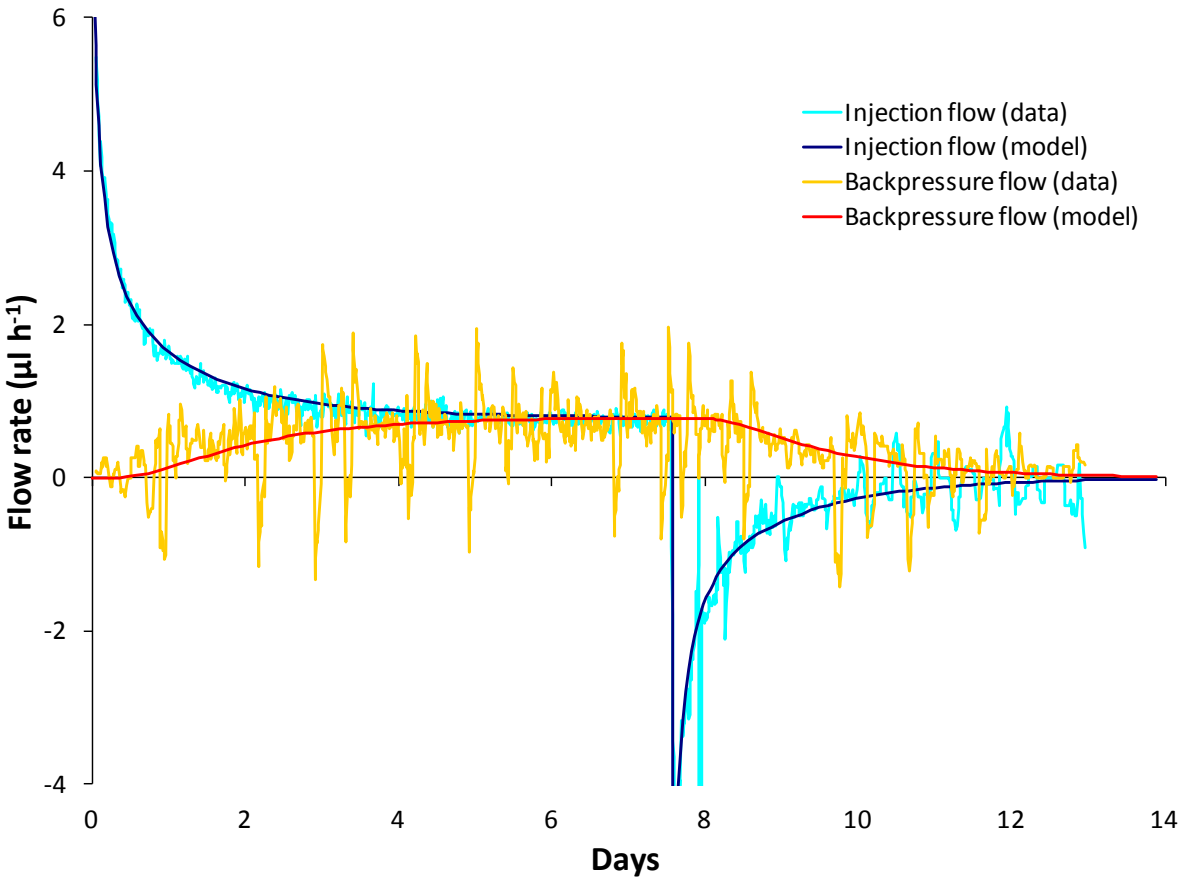

Figure 4-8 Comparison of observed flow rates from the injection and back pressure filters with the model simulation of the hydraulic test.

4.1.3 Gas injection

The gas pressure gradient across the sample has been slowly increased in a step-wise manner in order to investigate the mechanisms governing gas migration through the Callovo-Oxfordian clay. For each test stage the confining pressure and backpressure were maintained constant at values of 12.5 MPa and 4.5 MPa respectively. A list of test stages is presented inError! Reference source not found.. The pressure at the injection filter was raised from 6.5 MPa to 12 MPa in a series of 7 steps over 620 days. The first 5 steps were of 0.5 MPa and the last 2 were 1.5 MPa. The data obtained for pressures and flow rates are shown in Figure 4-9 and Figure 4-10. The data from the backpressure guard-ring is notable for the fact that it differs significantly from that of the backpressure filter only for a short period around 200 days into the test. The data from the injection guard-ring after about 180 days track the pressures at the injection filter very closely with an offset of only about 100 kPa. Before that time a number of anomalous features are seen in the injection guard-ring (Section 4.1.3.1). At the start of the test the injection guard-ring pressure declines from about 6.1 MPa to 5.0 MPa before abruptly rising again to about 5.8 MPa. That pressure is maintained until the injection pressure is stepped up to 7 MPa when the guard-ring pressure rises to about 6.5 MPa and remains at that level, with a slight decline, for the duration of the step. When the injection pressure rises to 7.5 MPa the guard-ring pressure initially follows but falls back by about 150 kPa for a period before rising again at about 180 days to a pressure that is about 100 kPa below the injection pressure. This offset remains consistent for the duration of the test, ranging from 100 to 135 kPa.

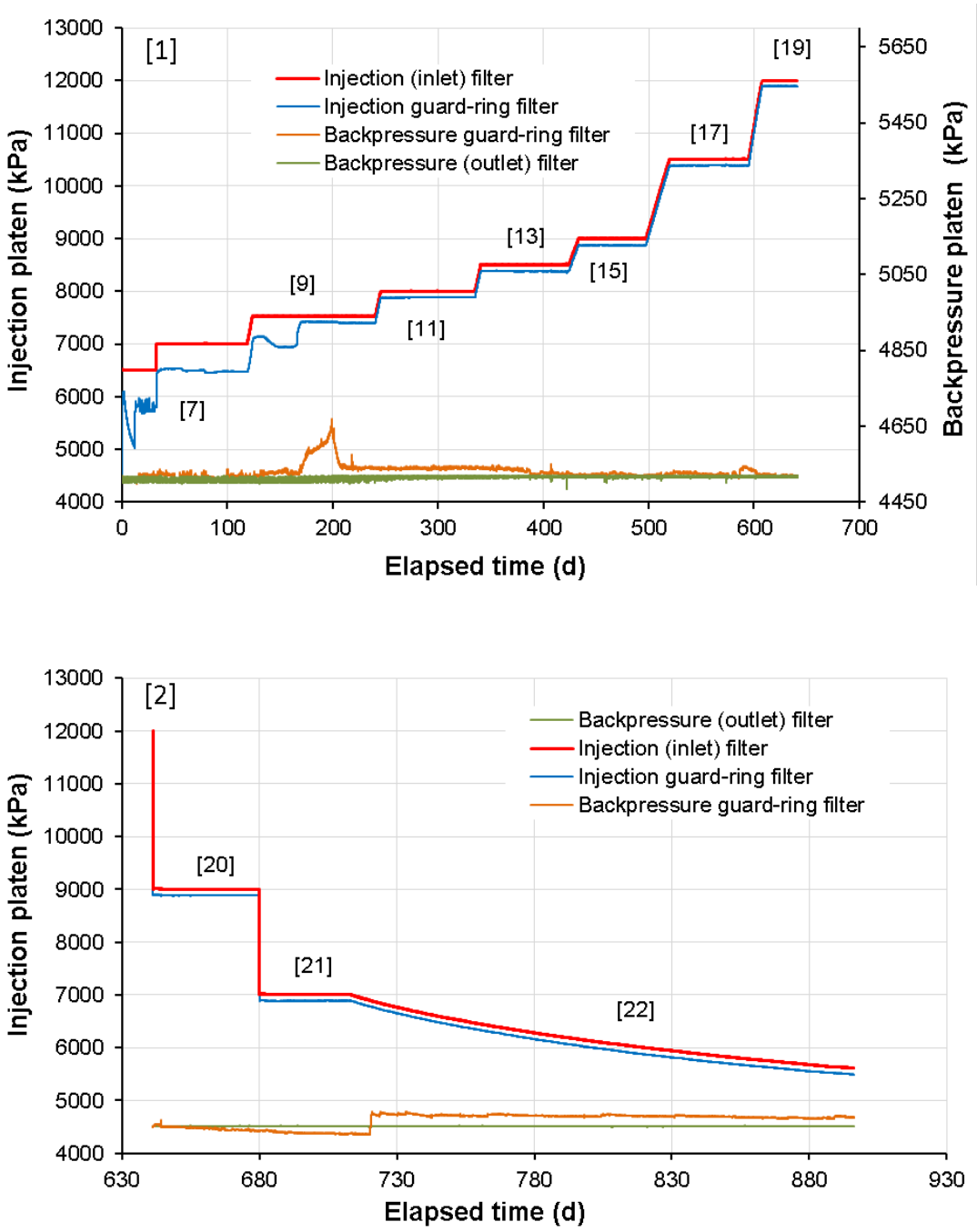

Figure 4-9 Pressure data from the injection, backpressure, and guard-ring filters during the gas injection test.

The gas outflow data show a small emergent flux until about 170 days (Section 4.1.3.1) when there is a gradually rising flow rate until an abrupt step at 200 days. Flow rate reduces again slightly at about 220 days and then follows a generally rising trend until about 430 days when the injection pressure is raised to 9 MPa. After an initial sharp rise in flow rate during this step there is a rapid decline at about 460 days and then recovery during the rest of the step. Flow rates then roughly double at the first of the 1.5 MPa steps in the injection pressure and a similarly substantial increase appears to be occurring in steps [17] and [19]. As the imposed flow rate is reduced, stages [20] and [21], the data exhibits significant hysteresis, with outflow larger during this 'imbibition' phase of the test history.

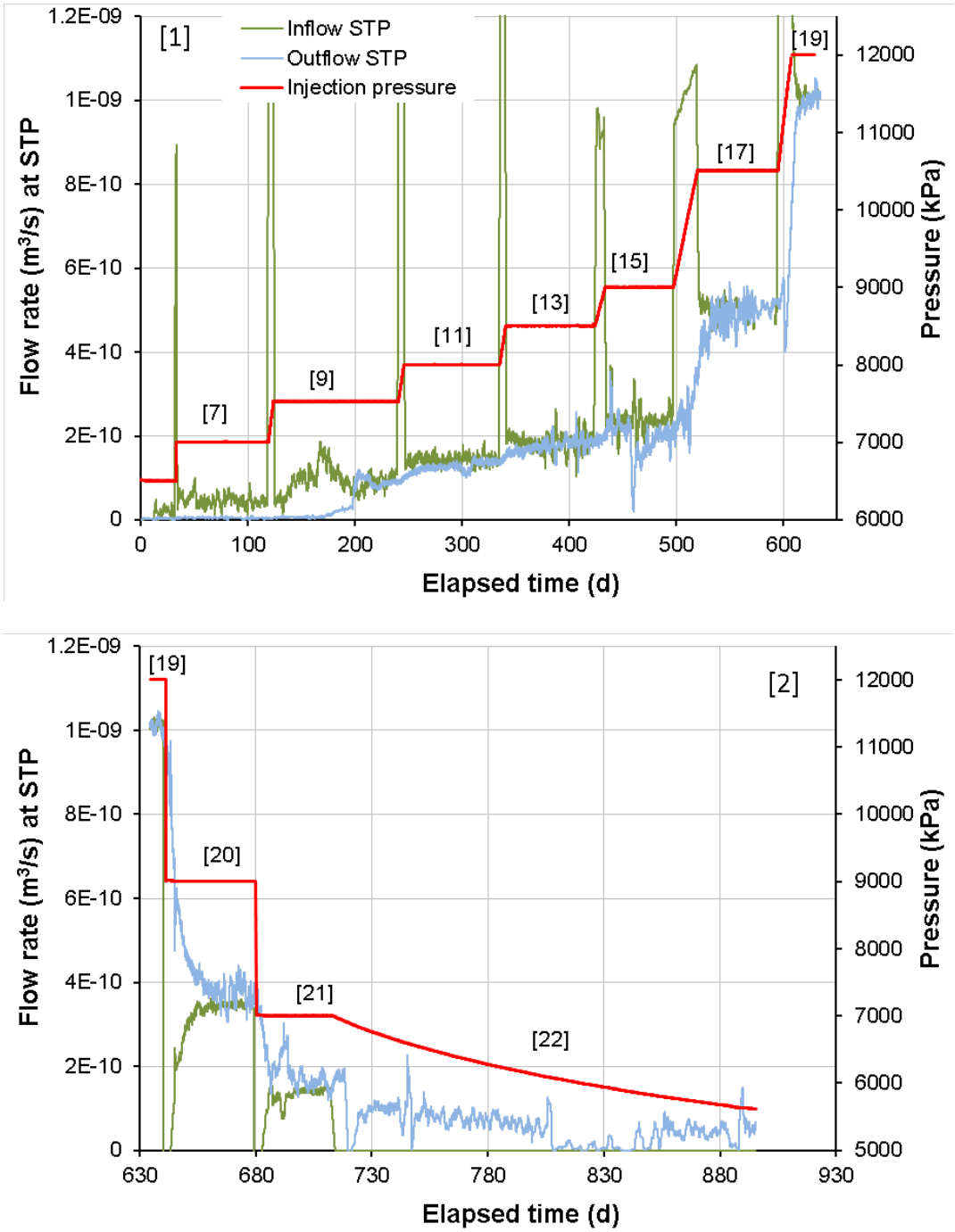

Figure 4-10 Gas flow rates at the injection and backpressure filters during the gas injection test. The large spikes in injection flux relate to the compression of the gas phase during constant flow rate test stages.

4.1.3.1 PRECURSOR FLOW

In test stages [6] through [9] gas pressure was increased in a series of steps while flux into[1] and out of the sample were monitored with time (Figure 4-11). The data clearly shows a small emergent flux discharged from the backpressure end of the specimen which begins shortly after the first increment in gas pressure is applied, test stage [6]. Flux out of the argillite remains constant at around 0.3 µl h^{-1} for the duration of the stage. Linear regression of the data (Figure

[1] Minor leakage problems with the injection pump degraded the resolution of the injection system resulting in the loss of accurate volumetric data for the first 200 days of testing.

4-12A) indicates quasi-steady state flow for the duration of the stage. After 32.8 days the increase in gas pressure, test stage [7], results in a small but measureable increase in discharge rate. This quickly plateaus at around 0.5 µl h^{-1} and remains constant for approximately 30 days (similar in length to the entire duration of stage [6]), before exhibiting a slow progressive decline to a value of around 0.4 µl h^{-1}. Linear regression of the discharge rate plotted against elapsed time yields a small negative slope symptomatic of the reduction in flux (Figure 4-12B). As before, flow out of the specimen quickly increases when gas pressure was again raised during test stage [9]. However, this time the discharge rate appears to remain in a quasi-steady state, yielding an average volumetric flow rate of approximately 0.6 µl h^{-1}. This continued for a further 47 days until the flux spontaneously increased, indicative of the start of major gas breakthrough. At this point in time the total fluid volume discharged from the specimen is around 1.87 ml. If we assume this relates purely to the displacement of water from the original porosity of the sample, then it would equate to a gas saturation of around 10%[2].

While this value outwardly appears reasonable a cross-plot of flux verses excess gas pressure (Figure 4-13) provides an initial estimate for the gas entry pressure of only 0.9 MPa. This estimate is low and is actually comparable to values reported for Boom Clay (Ortiz et al, 1997) which has a hydraulic permeability two orders of magnitude greater than the Callovo-Oxfordian argillite. Extrapolation of IGR pressure presented in Table 4-3 using a 3rd order polynomial fit to the data, Figure 4-14, provides a second estimate for the gas entry pressure. This yields a value around 1.3 MPa. We can therefore surmise that the initial gas entry pressure, close to the injection face of the clay, is in the range 0.9 to 1.3 MPa. However, it is important to recognise that these values are estimates only and relate specifically to the argillite in close proximity to the inlet filter and may relate to localised discrete features within the clay which are discontinuous within the majority of the sample.

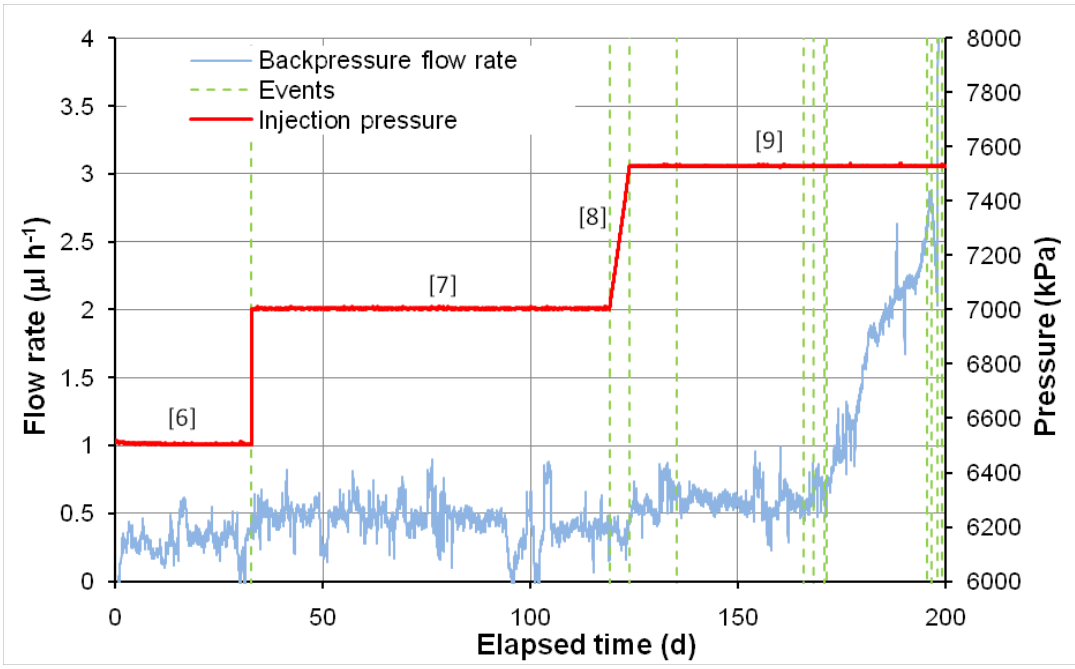

Figure 4-11 Backpressure flow rate and injection gas pressure plotted against elapsed time for test stages [6] through [9]. Note a small but measureable increase in discharge rate following the rise in gas pressure. The rapid increase in flow at around 171.5 days is indicative of major gas breakthrough.

[2] This estimate is likely to be high and may reflect a combination of processes including slug flow from residual water trapped in the injection filter at the time of gas sweeping.

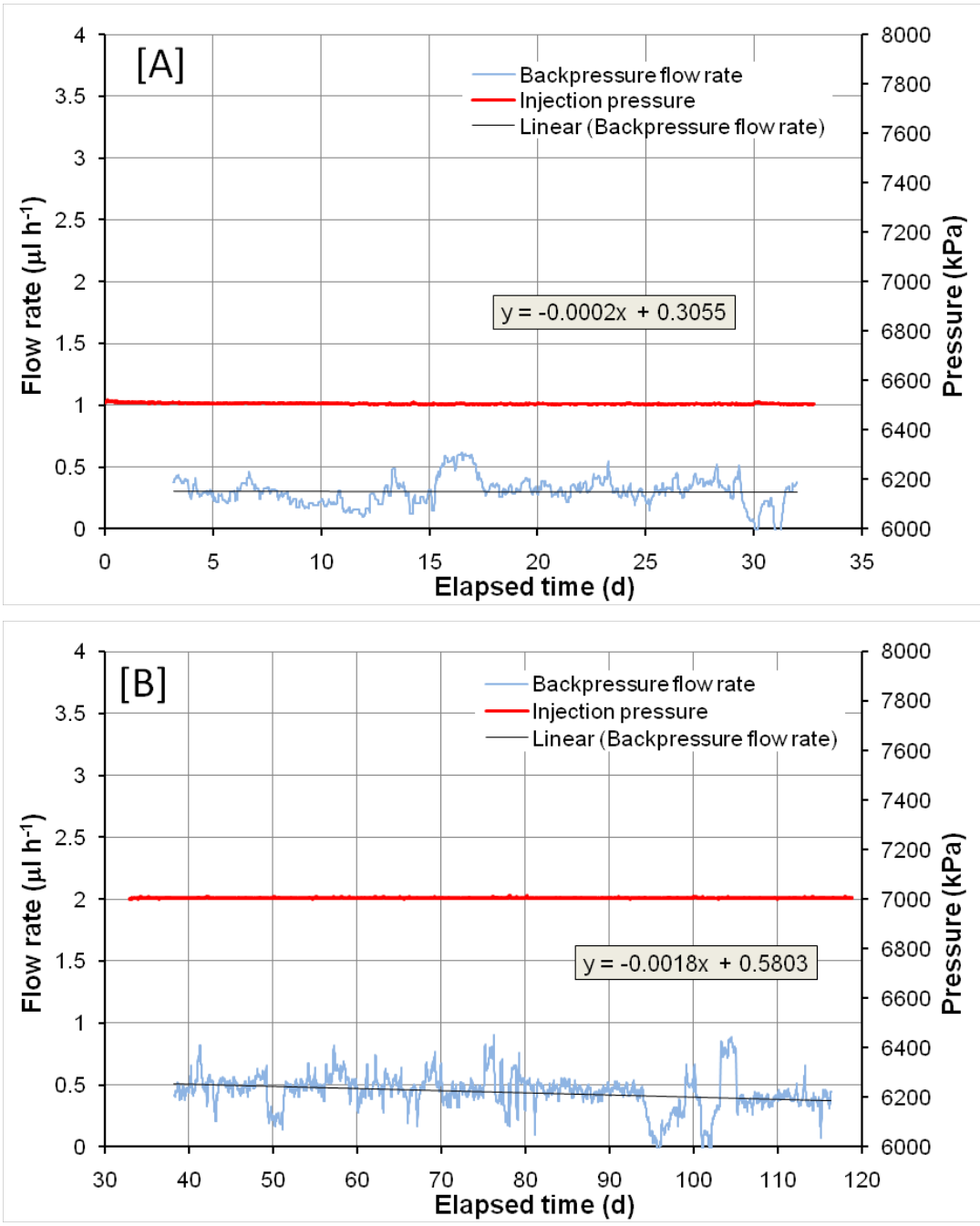

Figure 4-12 Backpressure flow rate and injection gas pressure plotted against elapsed time for test stages [6] through [7]. Linear regression of the data suggests flux is decreasing during stage [7].

While the origin of these precursor fluxes remains somewhat unclear, it is worth noting that the discharge rates are comparable to those observed during hydraulic testing, if the higher hydraulic gradient is appropriately scaled, suggesting the flux is aqueous in nature. Equivalent hydraulic conductivities calculated for these fluxes are of a similar order of magnitude to those observed during hydraulic testing (Figure 4-13). This hypothesis is supported by inspection of flux transients, which rapidly plateaus at the new steady-state value, following the change in injection pressure. This behaviour is suggestive of an incompressible response in which desaturation of the specimen plays little, if any, part. Analysis of data from the first gas stage of test COx-2 provides clear evidence for the existence of 'slug flow'. It is possible that the same applied to test COx-1 and that part or all of the observed precursor flow stems from incomplete sweeping of the injection filter and connecting pipe work. It is also possible that some of the fluid

originates from displacement of water following the early penetration of the injection guard-ring (IGR) by gas shortly after testing begins. This hypothesis is supported by the analysis of the hydraulic data in final section of 4.1.2.

However, further examination of the guard-ring data provides a useful insight into the system behaviour. As gas pressure is applied to the sample, stage [6], pressure in the injection guard-ring rapidly increases, reaching a peak value of 6095 kPa, before spontaneously declining to a minimum value of 5040 kPa. The asymmetry of this event (Figure 4-15) combined with the rapid increase in IGR pressure at day 12.6 are symptomatic of dynamic behaviour and suggests the movement of gas along unstable pathways. It is also noteworthy that following the jump in gas pressure at 12.6 days, the pressure plateaus at a significantly lower value than that observed the peak (day 1.5). This suggests that the network of conductive pathways has evolved during these events. Given the dynamic nature of this behaviour, it is highly unlikely that this relates to flow between the sample-platen interface, but rather gas movement along preferential features within the top section of the clay.

When gas pressure in the inlet filter was increased at the beginning of stage [7], the IGR pressure rapidly increased over a period of several hours, reaching a well-defined plateau. The difference in pressure between the injection inlet and guard-ring filter is around 0.7 MPa and 0.5 MPa for stages [6] and [7] respectively. The rate of IGR pressure increase and in particular, the shape of the resulting pressure transient (Figure 4-16), are atypical of the hydraulic behaviour observed in Figure 4-5 and are suggestive of gas pathway flow. Small spontaneous drops in IGR pressure at days 57 and 78 (Figure 4-17), further support this hypothesis and are highly indicative of unstable pathway flow.

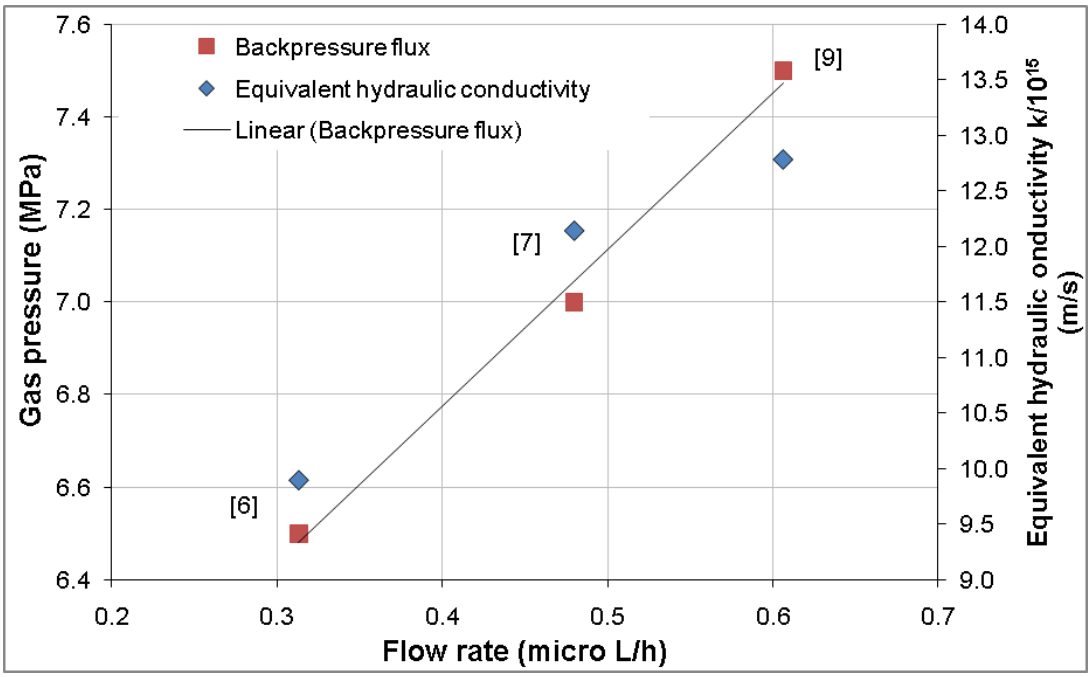

Figure 4-13 Cross-plot of gas pressure and equivalent hydraulic conductivity versus discharge rate during test stages [6], [7] and the initial section of [9]. Projection of the flux data to the zero flow condition suggests a gas entry pressure of around 0.9 MPa (see Figure 4-14). Equivalent hydraulic conductivities are of a similar magnitude to those observed during hydraulic testing.

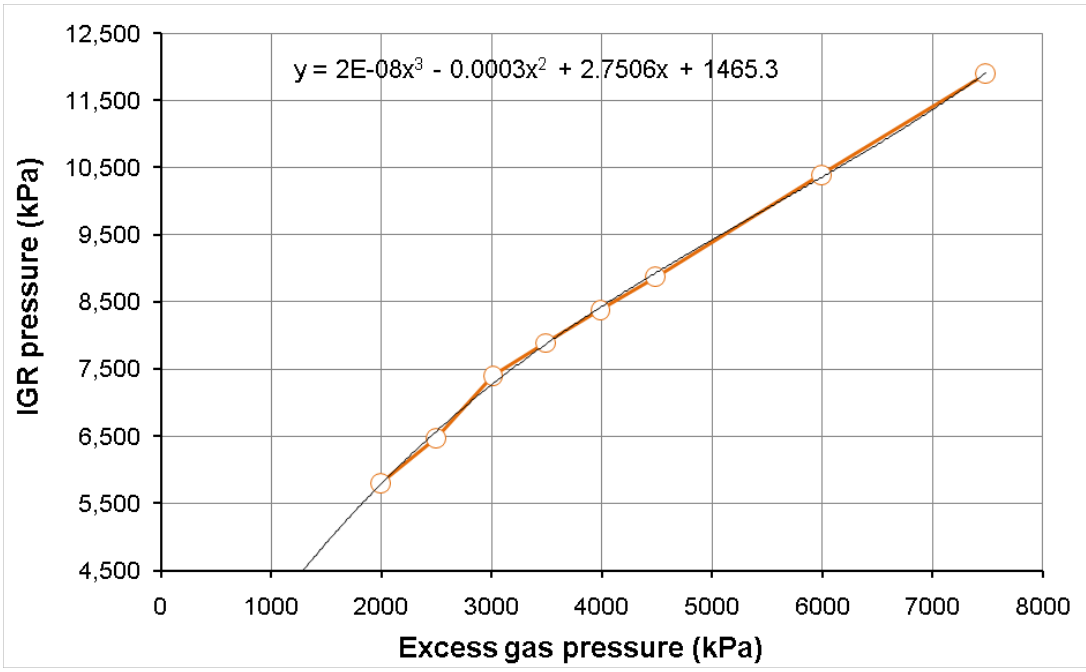

Figure 4-14 Cross-plot of IGR versus excess injection gas pressure. Extrapolation of the line suggests a gas entry pressure of approximately 1.3 MPa.

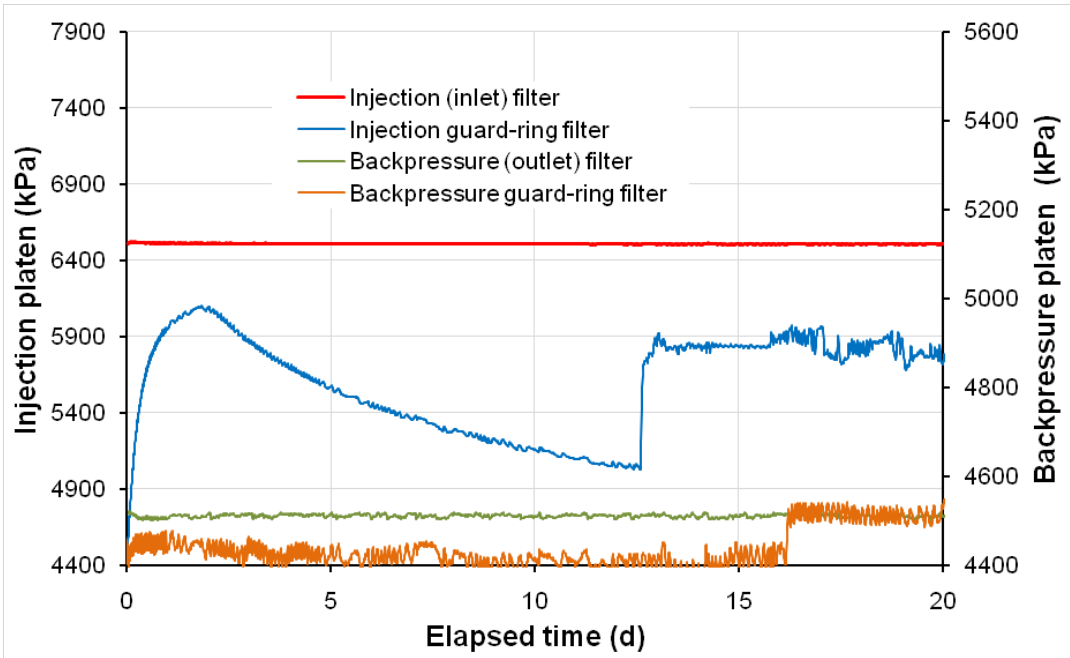

Figure 4-15 Pressure data from the injection, backpressure, and guard-ring filters during the stage [6]. The asymmetry of the injection guard-ring response observed during the first 12.6 days of the test is atypical of hydraulic behaviour, as is the spontaneous increase in IGR pressure at 12.6 days.

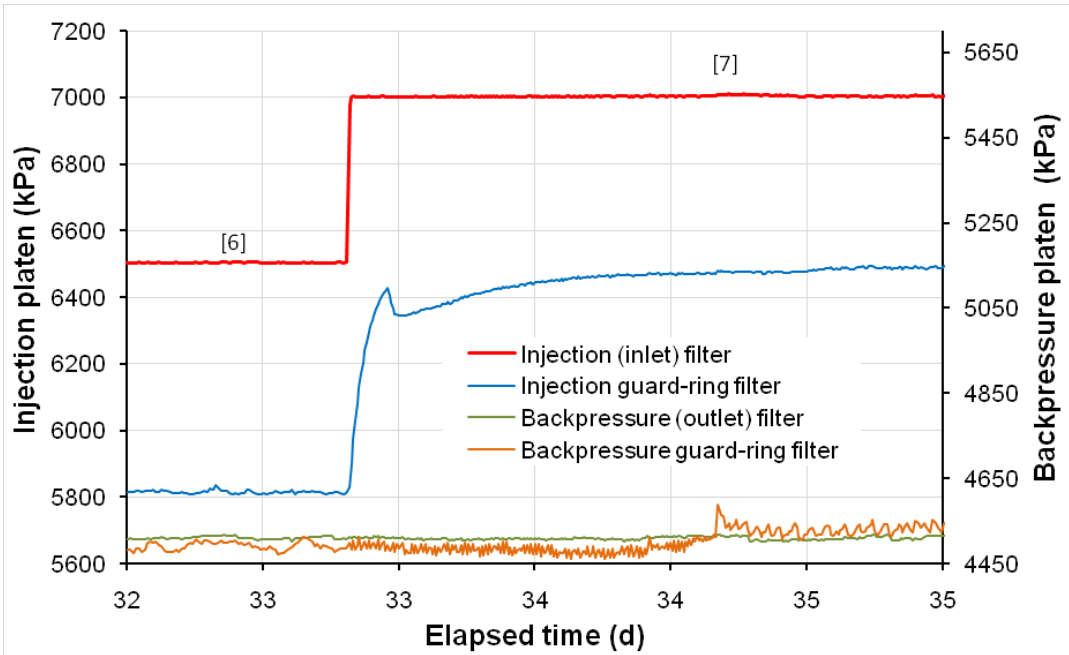

Figure 4-16 Pressure from the injection, backpressure, and guard-ring filters during the step-wise increase in pressure from stages [6] to [7]. The rate and shape of the IGR transient is atypical of hydraulic behaviour.

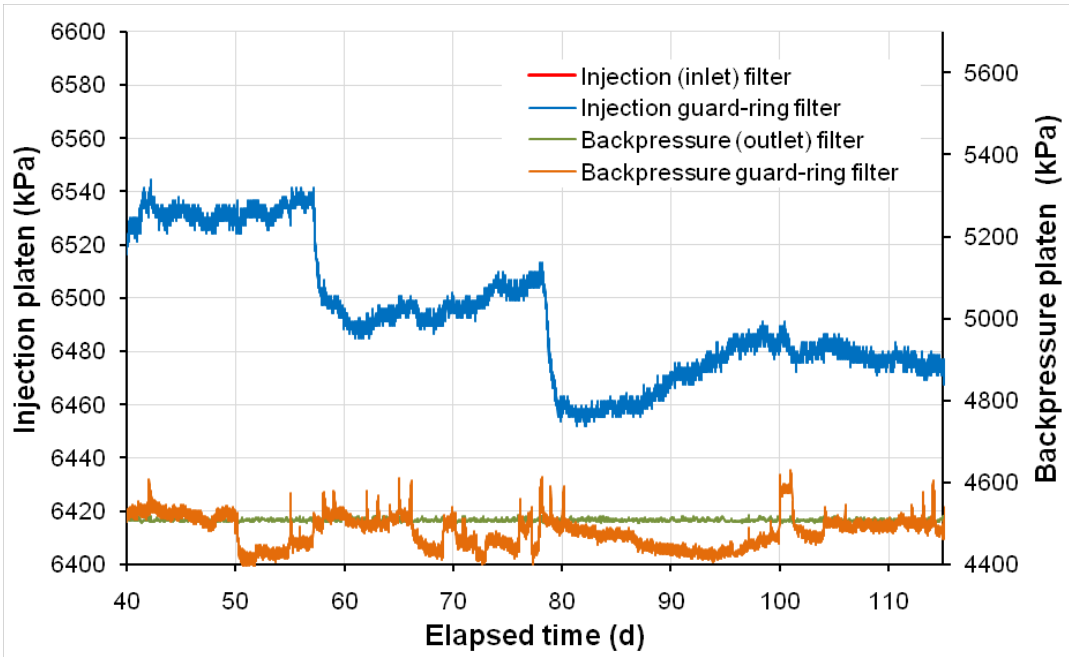

Figure 4-17 Evolution of IGR pressure during stage [7]. The spontaneous drops in pressure at days 57 and 78 are symptomatic of unstable pathways flow.

In summary, it seems clear from analysis of the data that gas penetrates the upper section of the argillite near the injection face relatively early in the test history. However, the lack of correlation between the IGR data and that of the downstream guard-ring pressures or the emergent flux, suggest that gas is unable to fully propagate across the specimen during stages [6] and [7]. While the origin of the precursor flux remains somewhat unclear, the data suggest they are predominantly aqueous in nature and do not relate to desaturation of the sample (Table 2-1). It is possible that part of this flow stems from desaturation of the argillite close to the injection The low value for the initial estimate of the gas entry pressure probably relates to localised

features within the clay close to the injection face, which may account for the initial high anisotropy observed in the hydraulic modelling (Section 4.1.2). Post-test mineralogy and petrology investigations of the sample in this zone may provide additional data with which to help to explain these observations.

4.1.3.2 BREAKTHROUGH

On day 123.9 the injection pump was switched to constant pressure mode signifying the start of test stage [9]. The inlet filter pressure was then held constant for the next 116.6 days. Analysis of the pressure data from the IGR filter exhibits a small time lag in reaching an asymptote at around 128 days (Figure 4-18). Pressure in the IGR filter then remains constant until day 135.3 when it spontaneously begins to decay even though the gas pressure gradient across the specimen remains constant. This behaviour is again symptomatic of unstable gas flow through a network of pathways between IGR and inlet filters. Gas pressure in the upstream IGR filter then begins to decay into the neighbouring clay which continues until day 146.8, at which point the pressure levels, oscillating around 6.95 MPa. Subtracting the backpressure from this value gives yields a highly tentative estimate for the capillary pressure locally within the sample of around 2.45 MPa, though this may be a somewhat arbitrary number if time dependent dilatancy plays a significant role in this behaviour. This value is significantly higher than the initial estimate for the gas entry pressure (Section 4.1.3.1) which suggests that either the gas has penetrated further into the clay, or, the network of clays pathways has evolved during the first 150 days of the test. It is also noteworthy that flux out of the specimen remains constant during this time.

However, what is clear from this data is that such dynamic responses in pressure cannot be explained by simple hydraulic flow and that gas penetration of the specimen provides the only viable mechanism to explain these observations.

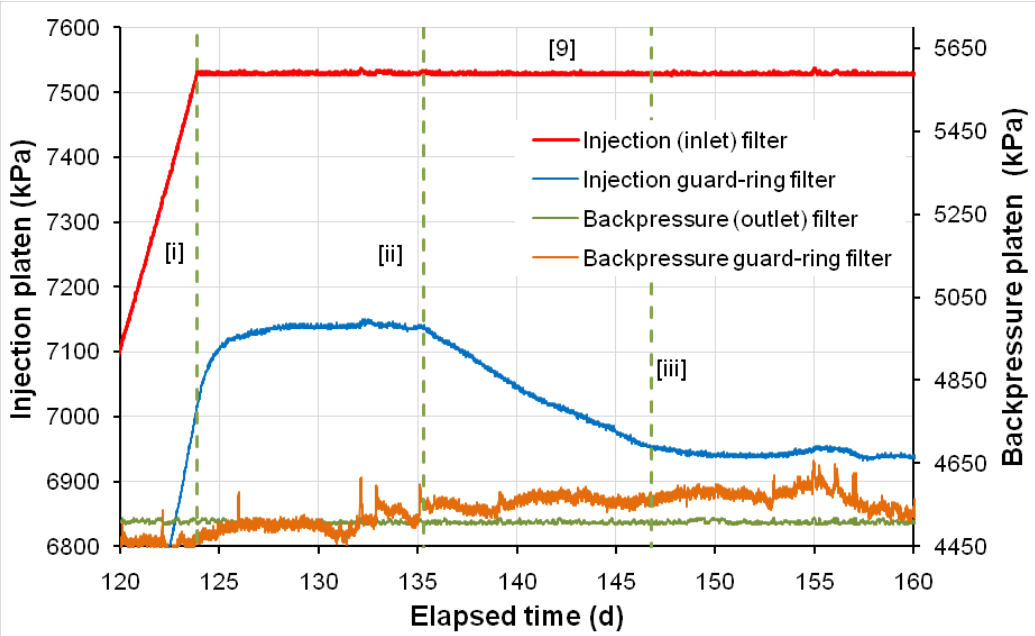

Figure 4-18 Evolution of guard-ring pressure during test stage [9]. Correlation lines [i], [ii] and [iii], indicate the start of stage [9], the initiation of the spontaneous negative pressure transient for the IGR filter and the inflection in the IGR pressure curve.

On day 165.7, pressure in the injection guard-ring spontaneously increases (Figure 4-19). On day 170.8, the backpressure guard-ring exhibits a small jump in pressure which then continues to steadily increase. This is followed on day 171.5 by a marked increase in discharge rate from the outlet filter, signifying the start of major gas breakthrough. By comparing 'breakthrough' times for the injection and backpressure guard-rings, it is possible to estimate the transit time of the gas across the specimen. Analysis of the data yields a value of around 5 days. It then takes a further 0.8 days for the gas to propagate to the outlet filter.

By cross-plotting the inflow and outflow data from stages [6] through [9] (Section 4.1.3.3, Figure 4-20) and linear regressing the data it is possible to estimate the excess gas breakthrough pressure. This value was found to be in the range 1.9 to 2.2 MPa.

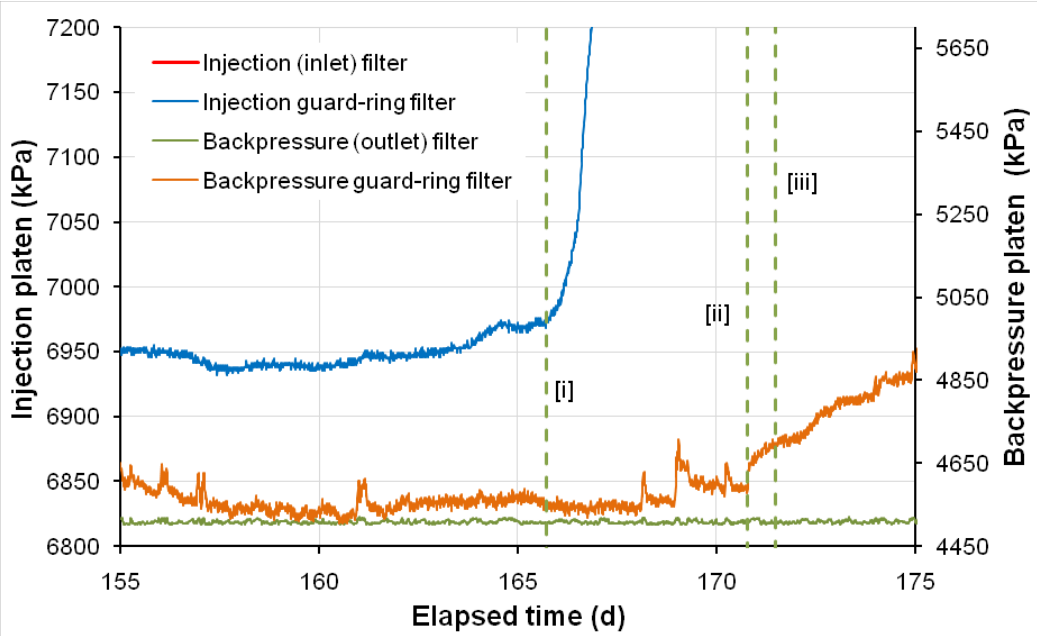

Figure 4-19 Evolution of guard-ring pressure during gas breakthrough. Correlation lines [i], [ii] and [iii] relate to increases in filter pressure at the injection and backpressure guard-rings and an increase in discharge rate respectively.

However, this raises an obvious question. Assuming these events are integrally linked, why did it apparently only takes five days for the gas phase to propagate across the specimen, given that the gas pressure gradient had remained constant for the previous 42 days? At present there is no definitive answer to this question, in part due the paucity of data from other detailed tests performed on the Callovo-Oxfordian clay. However, there is clear evidence from analysis of the guard-ring data for the existence of highly unstable gas pathways whose conductivity varies geospatially and temporally within the sample and test respectively.

Data from a triaxial test (Figure 4-21) clearly illustrates the time-dependent nature of deformation (i.e. radial displacement) within the COx during gas breakthrough (Cuss and Harrington, 2012). The change in sample volume stems from slow time-dependent deformation of the fabric. This evolution in behaviour provides an explanation for the evolution in gas flow observed across the specimen, as the gas meets and then slowly deforms its way through lower permeability or less compressible zones within the clay (see Section 6). Such a mechanism would introduce a time-dependency into the mechanisms governing gas flow in the Callovo-Oxfordian clay and would help to explain the observations seen in this experiment.

4.1.3.3 Steady-state gas flow

Following major gas breakthrough, flux out of the specimen again exhibits dynamic behaviour, first overshooting (Figure 4-22) then undershooting the ultimate value for steady-state[3]. This type of behaviour, observed in previous gas tests reported by Harrington and Horseman (1999; 2003), was considered to be indicative of the instability of conductive gas pathways.

[3] Even after extended periods of gas flow there is some evidence to suggest that there remains small residual slopes to a number of steady states.

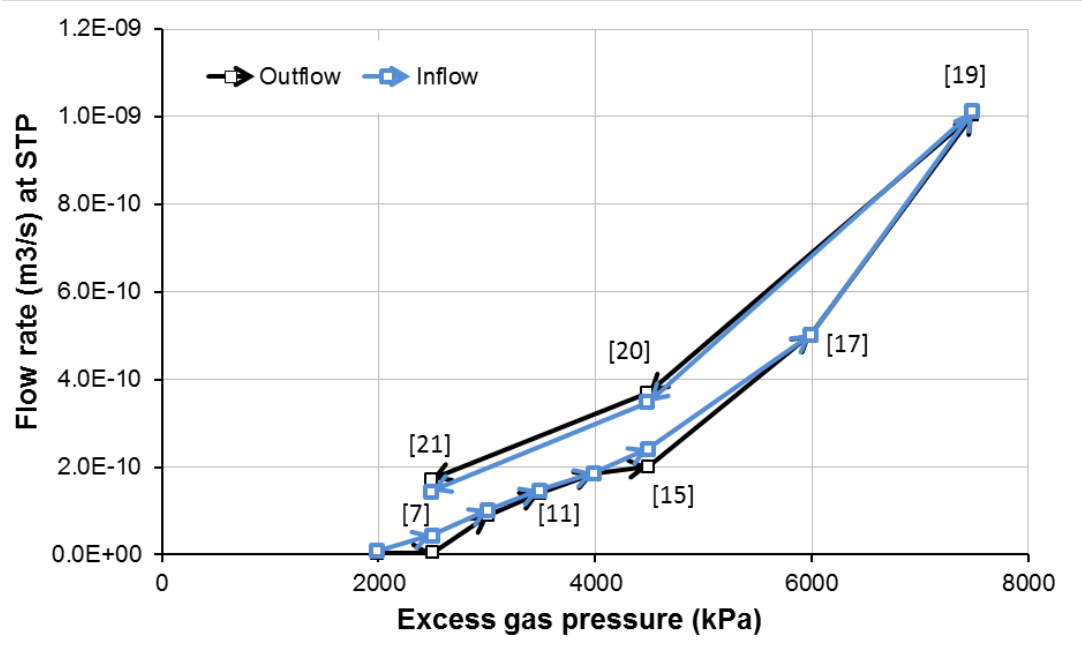

Figure 4-20 Cross-plot of flow in and out the sample plotted against excess gas pressure. The intersection of the lines provides an estimate for the gas breakthrough pressure. The hysteresis between ascending and descending flow cycles is evident in the data.

Prior to major gas breakthrough, pressure in the downstream guard-ring filter begins to increase (Figure 4-23). This continues for several days before levelling off at around 176 days. Pressure in the guard-ring then remains constant for a further 4 days, before spontaneously increasing to a peak value of 5.5 MPa. The observed inflections in slope are highly indicative of the spontaneous development of new conductive gas pathways. Following the peak, pressure in the guard-ring rapidly declines, exhibiting a sharp inflection in slope around day 210. Thereafter, gas pressure remains fairly constant for the duration of the stage. The highly dynamic nature of the guard-ring response provides conclusive proof for the existence of a network of highly unstable gas pathways. In the opinion of the authors such extreme changes in pressure are highly unlikely to occur as a result of instabilities associated with flow as embodied within classic concepts of two-phase flow, but are more likely to be symptomatic of the movement of gas along unstable, dilational gas pathways. This assertion is supported by post-test measurements of water saturation which show no discernible desaturation.

At the end of stage [9], gas pressure was gradually increased over a 5 day period to the next target value of 8.0 MPa, stage [11]. Here, gas pressure was again held constant for a further 89.4 days while flux into and out of the sample were monitored (Figure 4-24). While examination of the data in Figure 4-24 clearly shows the injection flux quickly levels, flow out of the sample lags significantly behind, taking a further 20 plus days to reach near steady-state. This time-dependent evolution in discharge rate is indicative of the slow development of conductive gas pathways, stemming from the dilation and deformation of the clay fabric. A summary of the gas data for each test stage is presented in Table 4-3.

Further examination of the data from stage [11] shows a small reduction in discharge rate around day 300. This is followed by an increase in flux from day 303 leading to a quasi steady-state where fluxes in and out closely agree. While these changes in flux are small they may reflect localised instabilities associated with the opening and closure of gas pathways.

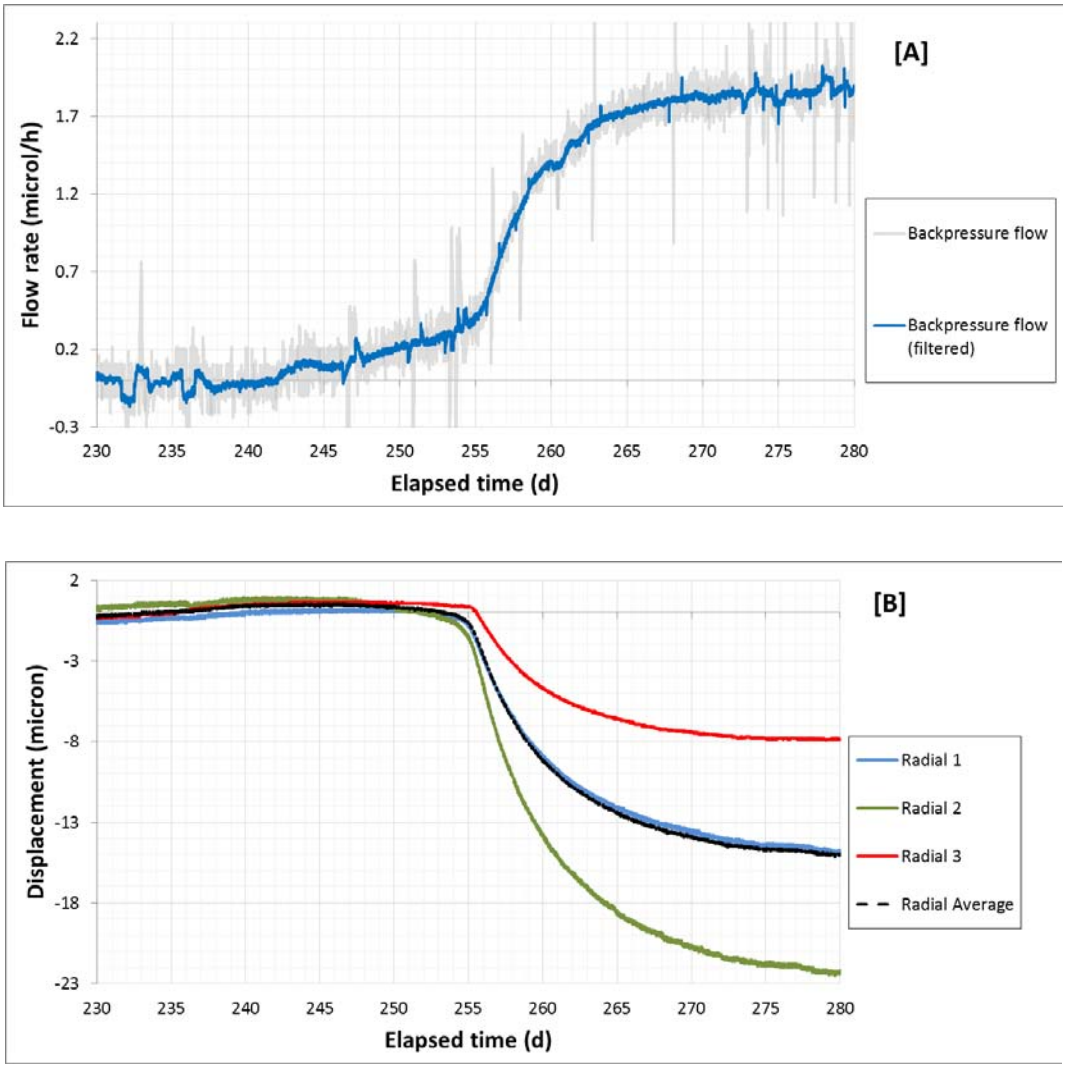

Figure 4-21 Flow and strain data from a triaxial test performed on COx (Cuss and Harrington 2012). Plot A shows the slow time dependent evolution in flux out of the core, while plot B, shows the sample dilating in response to changes in gas outflow.

The gas pressure gradient across the sample was then increased by 0.5 MPa in each of the next two increments, test stages [13] and [15]. As before, flux into and out of the specimen increased with the change in gas pressure gradient leading to quasi steady-states. Again, flux out of the sample lagged considerably behind the change in gas pressure, indicative of the time-dependent processes outlined above. Further evidence for the instability of gas pathways is seen within the data, in particular test stage [15], where outflow rapidly declines around day 459. It then takes a further 35-40 days for the flux to recover to close to the previous steady-state value.

In the final two ascending stages of the gas test, gas pressure in the inlet filter was increased to 10.5 MPa and then 12.0 MPa respectively, Figure 4-24. For each stage gas pressure was held constant for an extended period of time, yielding quasi steady-states. Comparison of data with that from Figure 4-25 shows that flux across the specimen significantly increases as the gas pressure gradient rises, approximately doubling between stages [15] and [17] and again between [17] and [19], even though the pressure gradient across the specimen has only increased by 25%. It is notable that the instability in flow apparent in the earlier data appears to reduce as the flux of gas across the specimen significantly increases. It is also notable that the time taken to reach steady-state is significantly less during these test stages. Given that the hydraulic conductivity of the intact clay remains the same as in previous stages, proportionally less, if any, desaturation of

the sample appears to occur at these higher flow rates. This suggests that dilation of the fabric plays a dominant role in the movement of gas through the argillite.

Setting aside the large obvious spike in downstream guard-ring pressure following the initial breakthrough event, it is possible through close scrutiny of the data to elicit significant detail relating to the mechanics controlling gas flow. Figure 4-26 contains a series of 30 day plots showing the downstream guard-ring response at various times during the gas injection test. From around day 245, there is a significant change in the underlying response of the pressure transducer, which begins to exhibit a 'saw tooth' type response, characterised by a rapid increase in pressure which then decays with time. Inspection of the data suggests some form of periodicity to the response though this has not been analysed as part of this report. This saw-tooth behaviour is symptomatic of unstable gas flow within the argillite, as gas pathways connect, discharge and then close. The pressurised gas trapped in the guard-ring filter then slowly decays with time as the gas moves back into the clay. However, at around day 380, the pressure in the guard-ring begins to reduce to a value roughly equal to that of the backpressure filter. Thereafter, the saw-tooth pattern is far less distinctive; suggesting gas flow to the guard ring has significantly reduced or stopped.

Hysteresis

During test stages [20] and [21], Figure 4-10 (2), the gas pressure gradient was decreased in a stepwise manner, mimicking stages [7] and [15] previous undertaken during the ascending gas history. Flux into and out of the specimen decreased with time, slowly evolving to a well-defined steady-state. In test stage [20] the asymptotic volumetric flow rate was nearly twice that of stage [15], Figure 4-20, indicating significant hysteresis in the flow response between ascending and descending flow histories. As pressure was reduced still further, stage [21], gas flow into and out of the specimen continued. This is in contrast to the equivalent stage [7], where little if any flow was observed. Analysis of the post-test saturation for specimen COx-1 suggests the sample remained fully saturated throughout the test. As such, the underlying cause for this apparent hysteresis is unclear but may relate to time-dependent processes associated with the creation and subsequent closure of dilatant gas pathways.

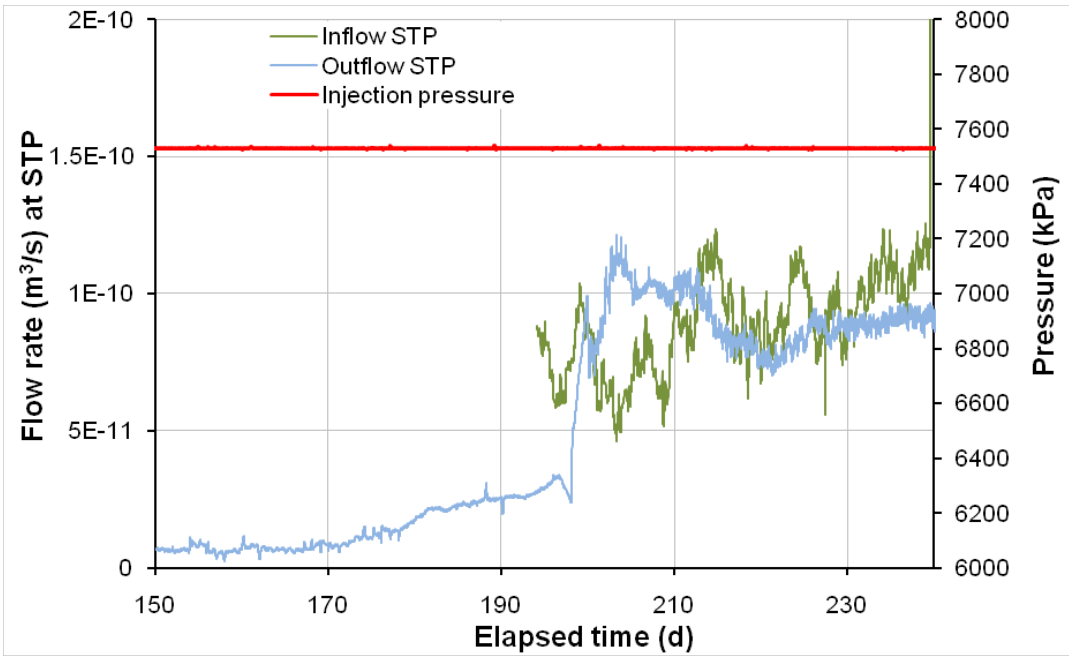

Figure 4-22 STP flow rate into and out of the specimen during test stage [9]. The inflow data has been cropped during the early part of the test due to problems with leakage from the injection system.

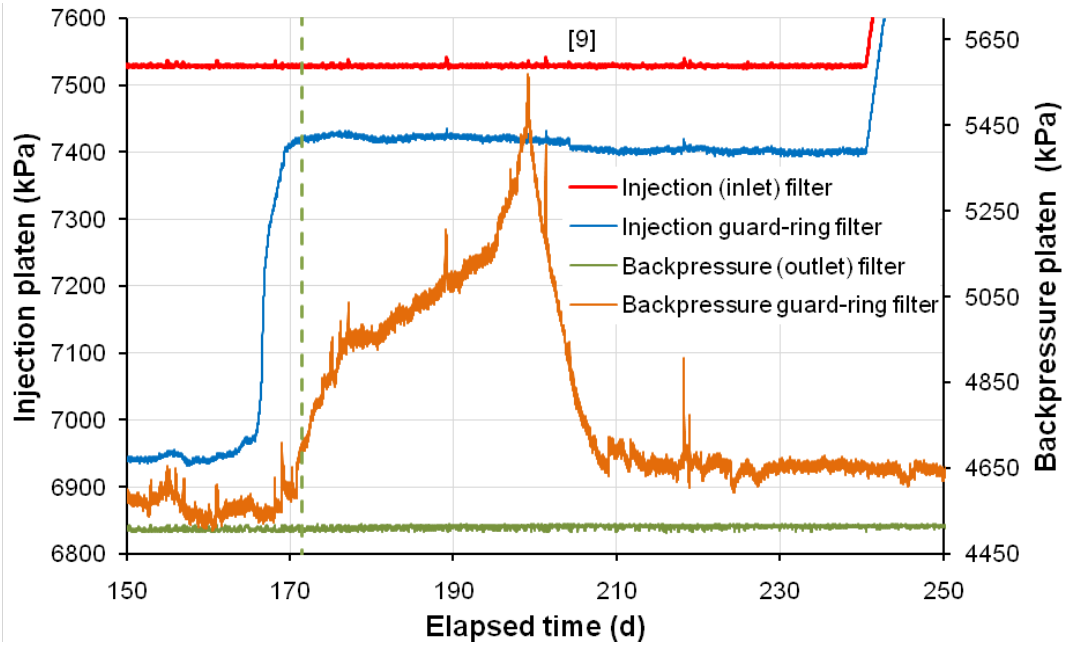

Figure 4-23 Evolution of guard-ring pressure during test stage [9]. The dash line indicates the point at which flux out of the specimen increases. The dynamic behaviour exhibited by the backpressure guard-ring can only be explained by the existence of highly unstable gas pathways.

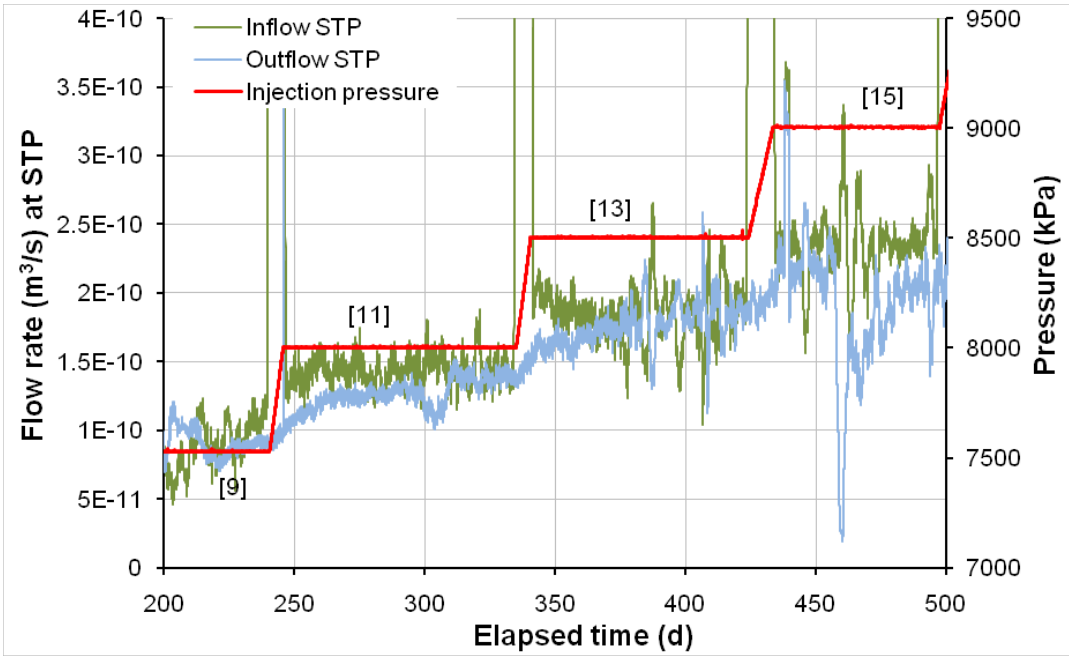

Figure 4-24 STP flow rate into and out of the specimen and gas injection pressure plotted against elapsed time during test stage [9] through [15].

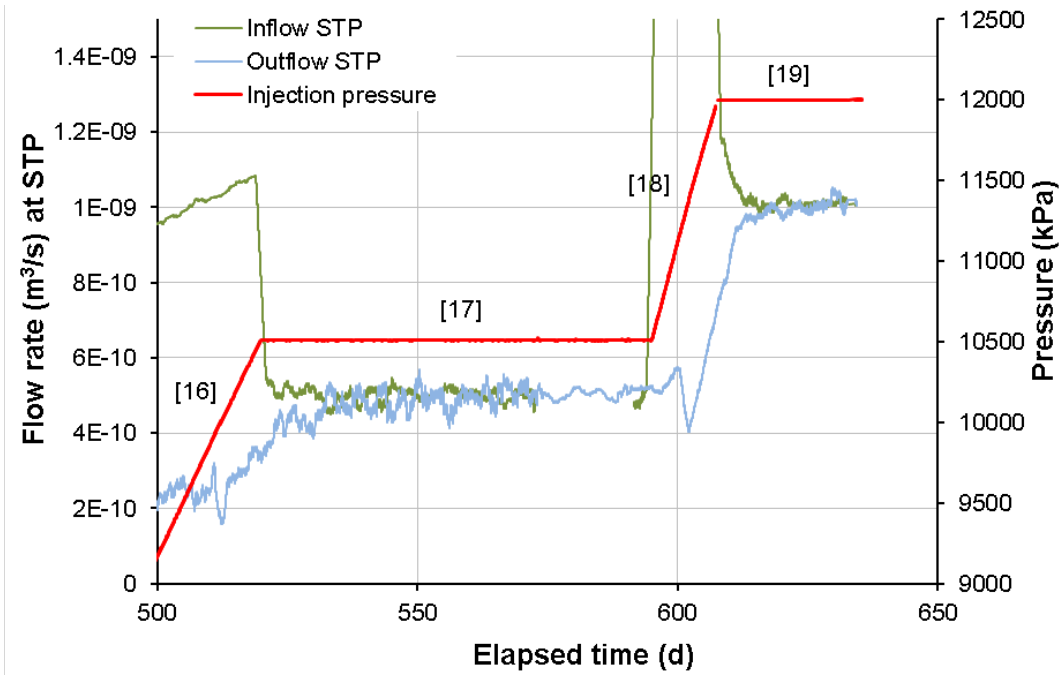

Figure 4-25 STP flow rate into and out of the specimen and gas injection pressure plotted against elapsed time during test stage [16] through [19].

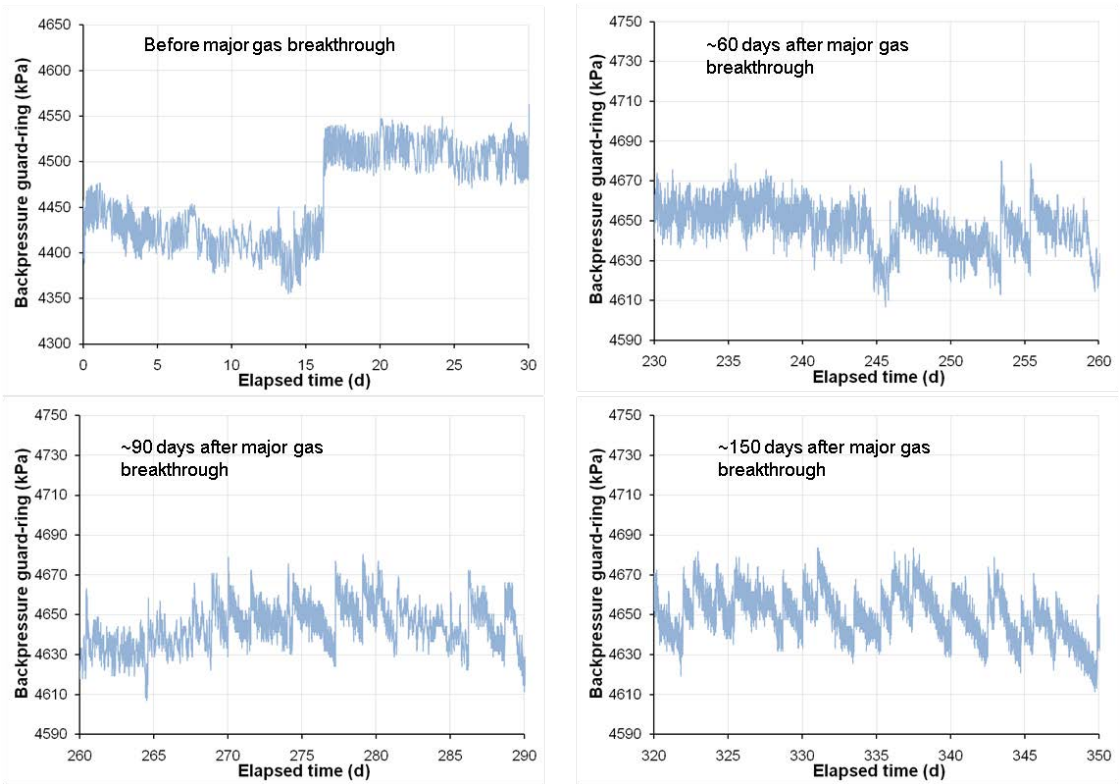

Figure 4-26 Downstream guard-ring response during gas testing. The saw-tooth pressure response observed in later data is symptomatic of unstable gas pathways.

Evidence for desaturation during gas testing

Inspection of the data from Figure 4-24 and Figure 4-25 show quasi steady-states for each test stage. By comparing mass flux into and out of the specimen, it is possible to estimate the

evolution of gas saturation associated with each increment in gas pressure (assuming standard concepts of two-phase flow apply). Figure 4-27 shows the area of flux (shaded in light red) which has been used to calculate the change in saturation for each step. As can been seen, a conservative approach to the calculation has been adopted, which should result in the prediction of minimal desaturation of the argillite for each test stage. However, a cross-plot of the data with excess gas pressure, Figure 4-28, indicates unrealistically high gas saturations for relatively minor excess gas pressures. This result, directly contradicts post-test measurements of sample desaturation (Table 2-1) which indicate no measureable desaturation of the sample, and would appear to confirm early observations suggesting dilatancy plays an important role in the movement of gas through the COx.

Analysis of volumetric data from the confining pressure pump appears to support this hypothesis showing a general trend of increasing sample volume as gas pressure increases (Figure 4-29), when gas pressure is reduced the sample volume decreases. While the correlation is rather crude more detailed measurements from a triaxial test (Figure 4-21) provide clear evidence of gas induced dilatancy (Cuss and Harrington, 2012).

Evidence for sample-sheath integrity

To address the potential for fluid flow between the sheath and sample when testing low permeability materials, the BGS developed the 'guard-ring' arrangement of filters. These provide an independent measure of pressure around the circumference of each platen which can be used to monitor the pressure evolution (and therefore interaction with the gas phase) during gas testing. While the guard-ring data clearly indicates the periodic presence of gas, it is hard from a mechanistic perspective, to see why this flow would periodically stem from flux around the sheath/sample during discrete stages of the gas test. There is no obvious correlation between upstream and downstream guard-ring pressures.

Close inspection of the data between 170 and 380 days shows that the downstream guard-ring pressure is above that of the downstream filter, indicating a small pressure drop exists between the two filters. The fact that this pressure drop remains fairly constant and doesn't vary even though discharge rate substantially increases indicates gas flow is not from the guard-ring to the outlet filter and therefore cannot be along the wall of the sheath. The fact the downstream guard-ring exhibited a maximum pressure of ~5.5 MPa indicates it was capable of supporting a significant pressure gradient to the downstream filter.

It may be that there are a number of conductive pathways near the downstream end of the sample which combine to give the results observed during hydraulic testing (which is likely to be far more uniformly distributed within the clay) but if gas flow is localised, may not interact with the downstream guard-ring during testing. This would explain the sudden peak in gas pressure near breakthrough and provide an explanation for the subsequent decay in pressure as pathway geometries evolve within the sample and the downstream guard-ring ceases to act as a significant sink. It should also be noted that if gas flow was along conductive features between sample and the wall of the sheath, the time taken to reach steady state (following an increment in pressure), should be relatively short.

However, inspection of the data clearly indicates time-dependent evolution of gas pathways even after many weeks of testing. This observation cannot be reconciled with concepts of by-pass flow.

Stage no.	Injection pressure (MPa)	Asymptotic value of guard-ring pressure (MPa)		STP conditions $Q_{st}/10^{11}$ ($m^3.s^{-1}$)	
		Upstream	Downstream	Flow in	Flow out
9	7.53	7.40	4.65	9.9	8.9
11	8.00	7.89	4.65	14.5	13.8
13	8.50	8.38	4.55	18.5	18.5
15	9.00	8.87	4.51	24.0	20.0
17	10.51	10.39	4.55	50.1	50.2
19	12.00	11.90	4.50	101.2	100.4
20	9.00	8.89	4.43	34.6	36.8
21	7.00	6.89	4.37	14.1	17.0
25	7.53	7.48	4.59	14.0	13.8
27	12.00	11.93	4.64	100.0	96.7

Table 4-3 Summary of the steady-state gas results for test stages [9] through [27]. Analysis of the flux data indicates breakthrough pressure for initially water saturated conditions in the range 1.9 to 2.2 MPa.

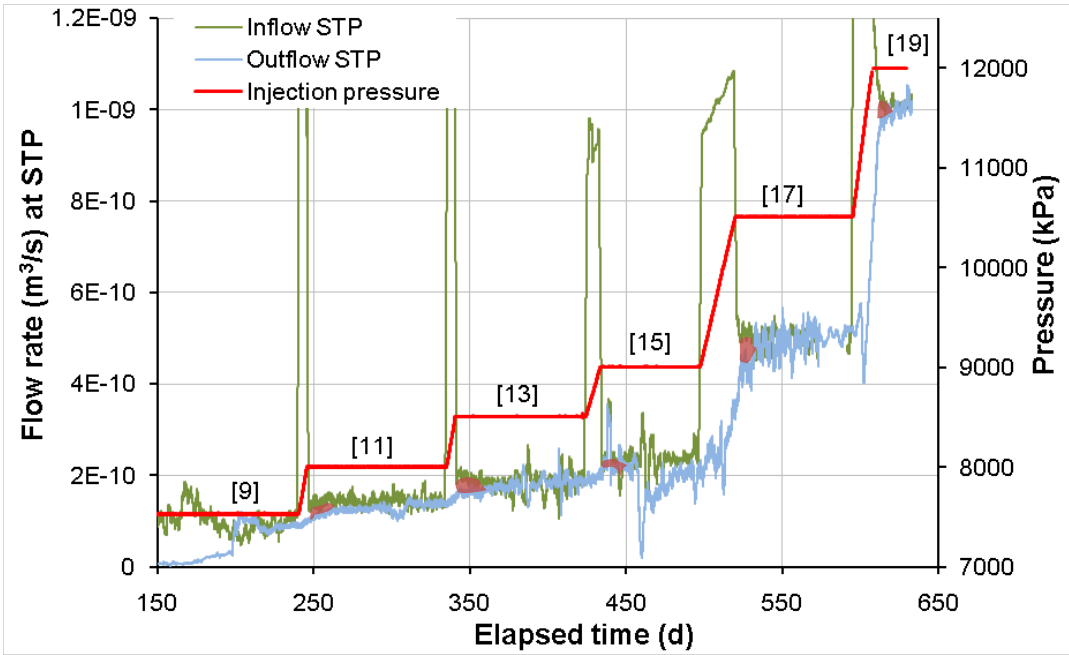

Figure 4-27 STP flow rates into and out of the sample. The red shaded areas at the beginning of each stage delineate the sections of the transient response used to estimate saturation.

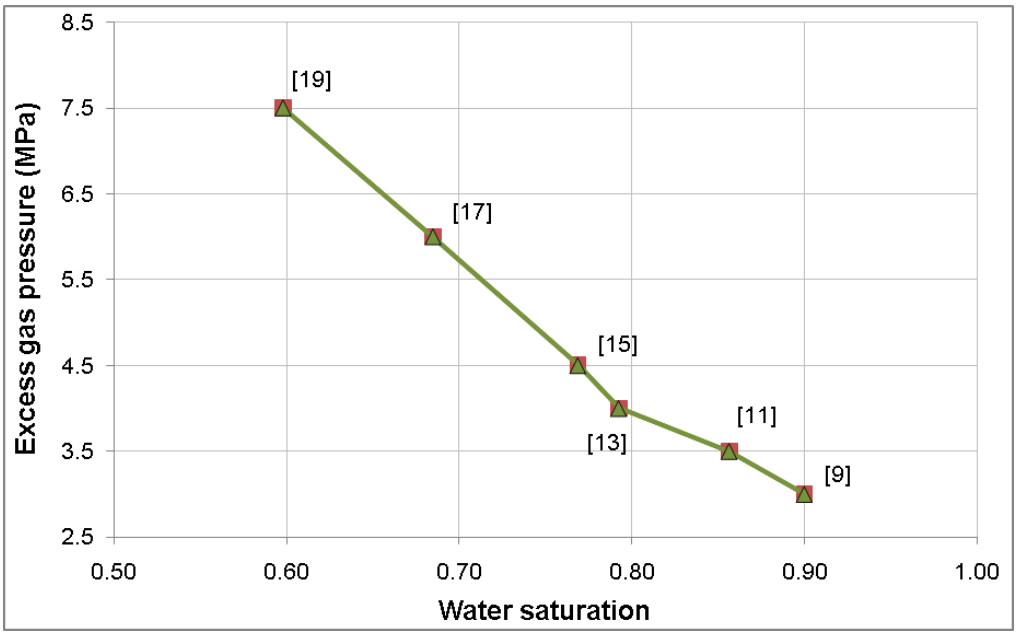

Figure 4-28 Cross-plot of excess gas pressure against estimated water saturation based on mass balance. Estimates for the water saturation are derived from mass balance of the STP data presented in Figure 4-27. STP volumes have been corrected back to experimental conditions assuming a capillary threshold pressure of 2.0 MPa. However, the data predicts unrealistically high desaturations which cannot be reconciled with post-test measurements of sample saturation.

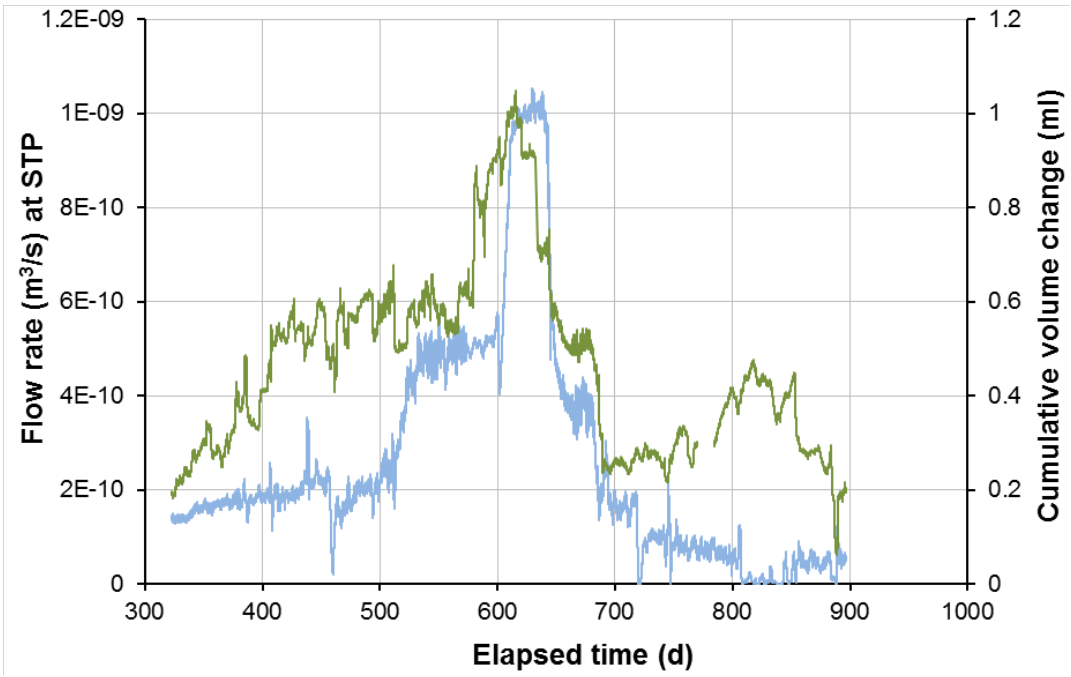

Figure 4-29 Outflow from backpressure filter and cumulative flow from confining pump (from day 322 onwards) plotted against elapsed time. While the correlation is rather crude the data suggests an underlying trend of volume increase as outflow (and pressure) increase and volume decrease when outflow (and pressure) fall.

4.1.3.4 Pressure decay (shut-in)

To estimate the apparent capillary threshold value (i.e. the point at which gas ceases to be mobile within the clay), the injection pump was switched off and excess gas pressure allowed to decay.

Figure Z1 shows the slow time-dependent decrease in pressure as permeability within the sample deceases. The length of the transient is a direct consequence of the non-linearity in the gas flow law. However, an estimate of the transient length can be obtained using governing differential equation for axial flow (Harrington and Horseman, 1999)

$$V_{gi}\frac{dp_{gi}}{dt} + p_{gi}\frac{dV_{gi}}{dt} = B\left(p_{go}^2 - p_{gi}^2\right)$$

where p_{gi} and V_{gi} are the pressure and volume of gas in the injection system, p_{go} is the sum of the external water pressure (p_{wo}) and the apparent value of matric suction (p_{co}) and B is a transport variable given by

$$B = \frac{k_g A_s}{2\eta_g L_s}$$

where k_g is the effective gas permeability, A_s the cross-sectional area, η_g the viscosity of gas and L_s the length of the specimen. The solution to the governing differential equation during the shut-in stage (i.e. when the injection pump is set to zero flow rate) gives

$$p_{gi} = p_{go}\left[\frac{(p_{gi0} + p_{go})exp(Ht) + (p_{gi0} - p_{go})}{(p_{gi0} + p_{go})exp(Ht) - (p_{gi0} - p_{go})}\right]$$

where p_{gi0} is the initial pressure of gas in the injection system, *t* is the elapsed time from stopping the pump and

$$H = \frac{2Bp_{go}}{V_{gi0}}$$

where V_{gi0} is the volume of gas at the start of the shut-in. Using this solution a good fit to the data (Figure 4-30) can be achieved with the following parameters: A_s=3.142E-4 m^2 (equates to the cross-sectional area of the central injection and backpressure filters); k_g=2.55E-21 m^2; p_{co}=1x10^6 Pa. While these may not be exactly correct, we can use this technique to produce an estimate for the length of the test. Assuming conditions and material properties remain constant (which is a significant assumption) Figure 4-30 suggests stage [22] may take around 680 days to reach an asymptote.

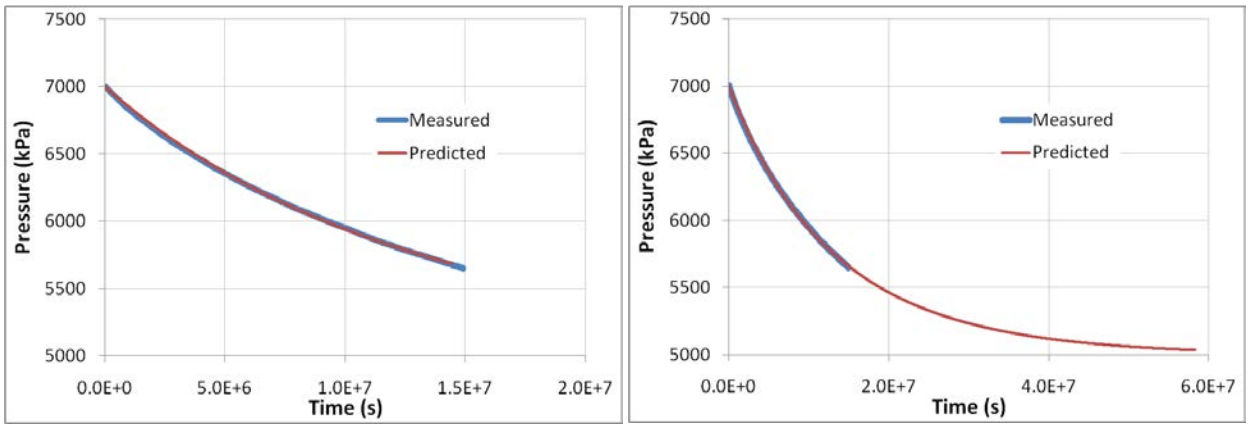

Figure 4-30 Shut-in response for test COx-1. The protracted nature of the shut-in response is a function of the initial gas volume and the non-linearity in the gas flow law. However, a good numerical fit to the data is obtained allowing a prediction of the capillary threshold pressure to be made.

4.1.4 Hydraulic test – post gas injection

Following completion of the gas injection test a second hydraulic test has been carried out and the data from which is presented in Figure 4-31 and Figure 4-32. Attempts to model this data

assuming a saturated initial state give rather poor fits, possibly due to the effects of residual gas in the system.

Figure 4-32 compares the pressure data with a model in which the axial permeability is 1.65×10^{-21} m^2, the radial permeability is 3.30×10^{-20} m^2, and the specific storage is 4.5×10^{-5} m^{-1}. It may be noted that a very similar fit can be obtained using an isotropic permeability for the clay of 1.65×10^{-21} m^2 but including surface leakage fluxes through surface zones with transmissivities of 3×10^{-16} $m^2 s^{-1}$. It can be seen that the model output does not match the data for the injection guard ring until about 25 days into the test. Similarly, during the recovery step of the test it takes about 25 days before the model again matches the injection guard ring data. The model output for the back-pressure guard ring is not at all similar to the data except for a short period around the end of the injection step and the beginning of the recovery step.

Figure 4-32 also shows the comparison of the flow rate data from the test with output from the same model. It can be seen that the model provides a good match to the inflow data after the first 20 days of the test. However, the outflow data bears almost no resemblance to the model predictions.

For comparison, the hydraulic test conducted before gas injection was found to match a model in which axial permeability is 2.0×10^{-21} m^2, radial permeability is 5×10^{-20} m^2, and specific storage is 5.4×10^{-6} m^{-1}, or, with surface leakage flow, an isotropic permeability of 1.8×10^{-21} m^2. There appear to have been small changes to the permeability, but the specific storage appears to have increased by about an order of magnitude. As indicated above, this is probably due to the effects of residual gas within the sample pore space, clearly demonstrating gas has fully penetrated the fabric of the clay.

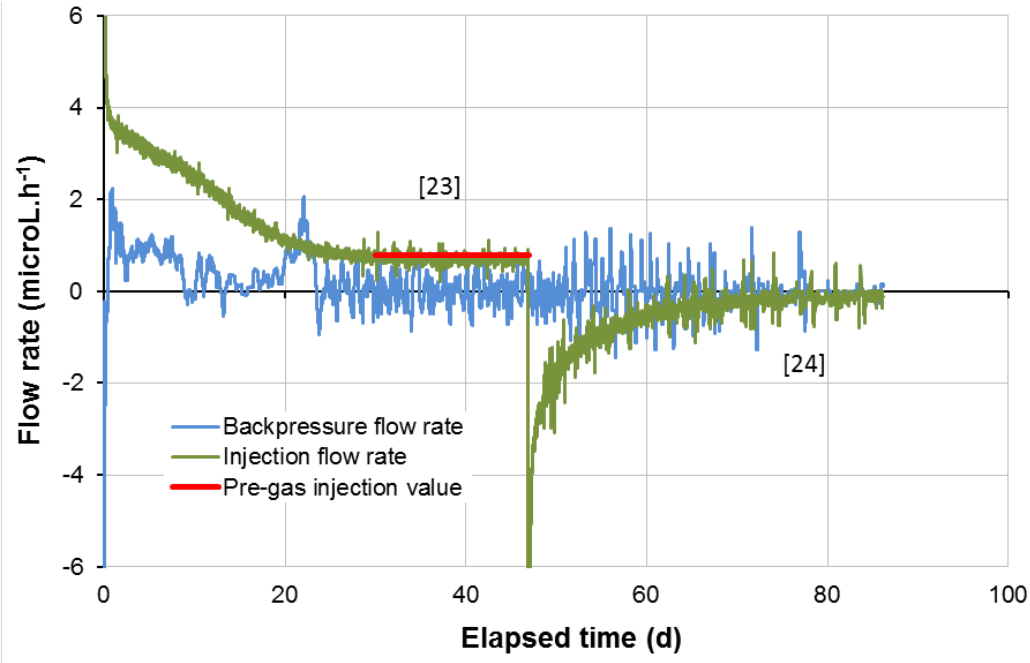

Figure 4-31 Hydraulic response following the initial gas injection cycle. Flow in asymptotes at a value very close to that of the pre-gas injection stage (red line). The offset in the outflow data probably relates to minor leakage.

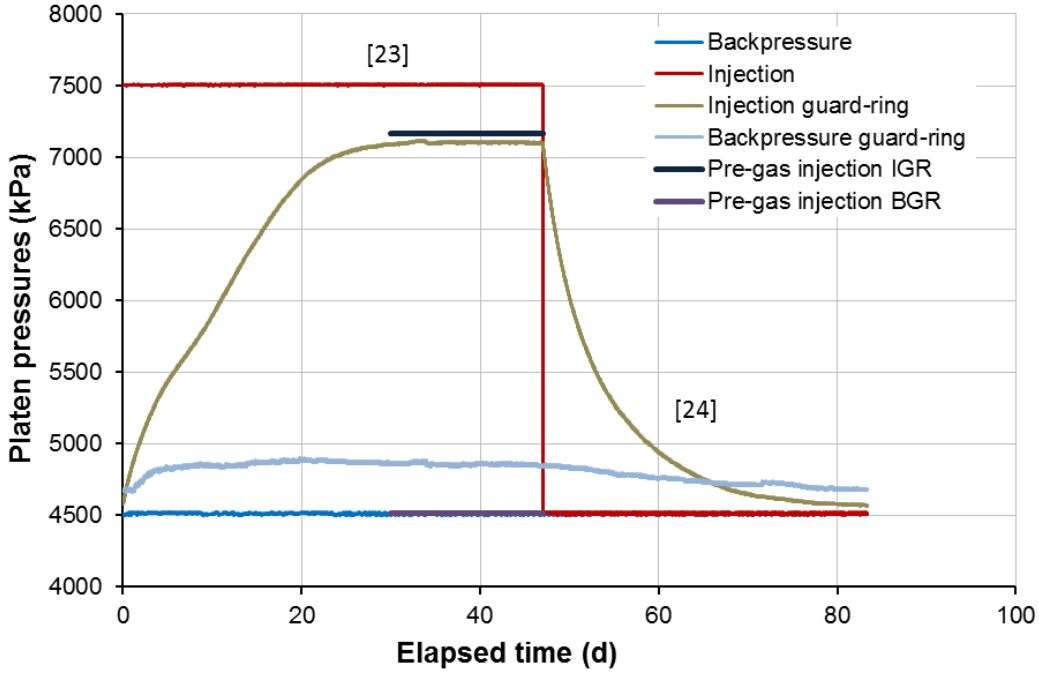

Figure 4-32 Guard ring response during second hydraulic test. While the slow pressurisation of the injection guard ring (IGR) is caused by the presence of residual gas within the filter, the asymptote is very close to the previous value. This suggests little if any change in hydraulic anisotropy. The downstream guard ring pressure (BGR) appears insensitive to the hydraulic gradient with its response probably dominated by the presence of residual gas.

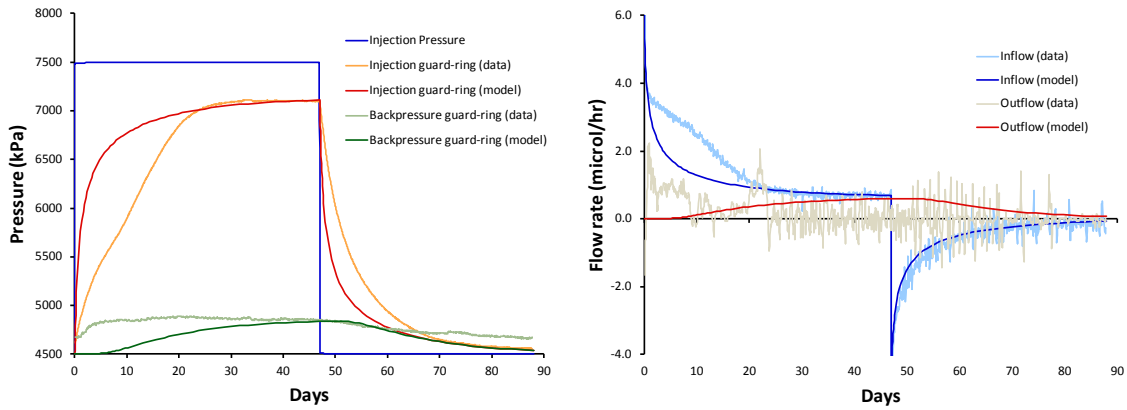

Figure 4-33 Comparison of observed guard ring pressures and flow rates with the model simulation of the post-gas injection hydraulic test on sample COx-1.

4.1.5 Second gas injection test

To examine the self-sealing capacity of the COx, it was decided to perform a second gas injection test following a simplified pressure history compared to that observed during the first gas injection cycle. Following flushing of the sintered filters with helium to try and remove the hydraulic permeant, the injection pressure was set to 7.5 MPa and flow into and out of the sample monitored with time (Figure 4-34 and Figure 4 33). Inspection of the guard-ring data shows a rapid rise in the injection guard-ring pressure (IGR) shortly after the introduction of the gas within the central injection filter. This is accompanied by a small increase in backpressure guard-ring (BGR), possibly caused by gas displacement of water from the IGR filter, and a small emergent flux of fluid out of the sample.

In total 1.38 ml of fluid was expelled from the sample during this period. As pressure was maintained constant, out flow spontaneously increased at around 82.5 days. This was accompanied by a drop in backpressure guard-ring and a subsequent increase in the injection guard ring pressure (Figure 4-35) at a slightly later time of around 83.3 days. Prior to these events, small scale changes in guard ring pressure suggests a dynamic network of gas filled pathways begin to form early in the test stage. These unstable features then continue to evolve in time and space within the sample, opening and closing depending on the localised flow of gas.

Flow into and out of the sample then evolves to 'two' apparent steady-states. The first at day 82.5 is interpreted as major gas breakthrough. This quasi-steady state lasts for around 14 days, before flux spontaneously increases. The evolution of flow during this second transient phase is markedly different to that observed during the initial event at 82.5 days. While the injection flow rate rapidly increases to a well-defined asymptote, outflow evolves much more slowly. This transient behaviour can be viewed as the time dependent development of permeability within the sample. During this time there are also a number of notable changes in guard-ring pressure. These responses are again, symptomatic of an evolving network of highly unstable gas pathways, the number and distribution of which appear to vary with time. Interestingly many of these events do not correlate with specific changes in flow, suggesting they may be relatively unimportant to the bulk movement of gas through the sample. By around day 140, the system enters a stable quasi-steady state regime with flow in and out generally equal.

While there are a number of subtle differences between the stages [25] and [9], examination of the data suggests a number of clear commonalities between the two breakthrough events. These include the time dependent development of conductive pathways, and pathways which are unstable and evolve both in time and space. While unclear at present, the origin of the initial outflow may relate to slug flow and displacement of water from the injection guard-ring filter/system. However, this phenomenon requires further investigation, what is clear, is that gas flow in the COx is a highly dynamic and coupled process.

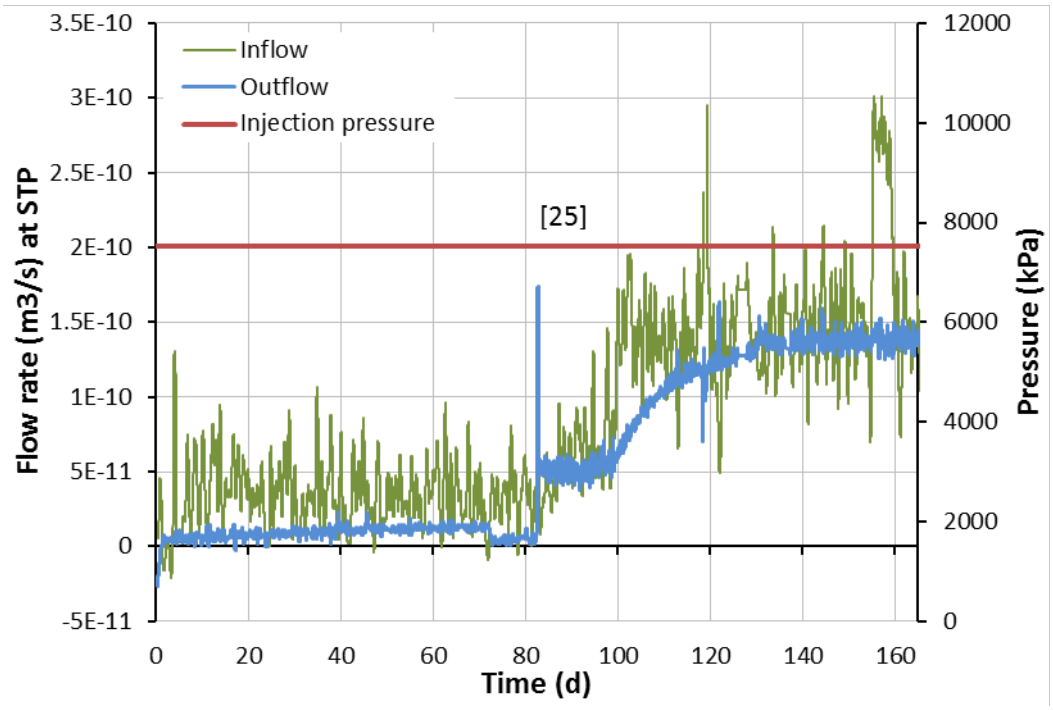

Figure 4-34 Evolution in flow into and out of sample COx-1 to examine self-sealing characteristics of the Callovo Oxfordian Clay during stage [25].

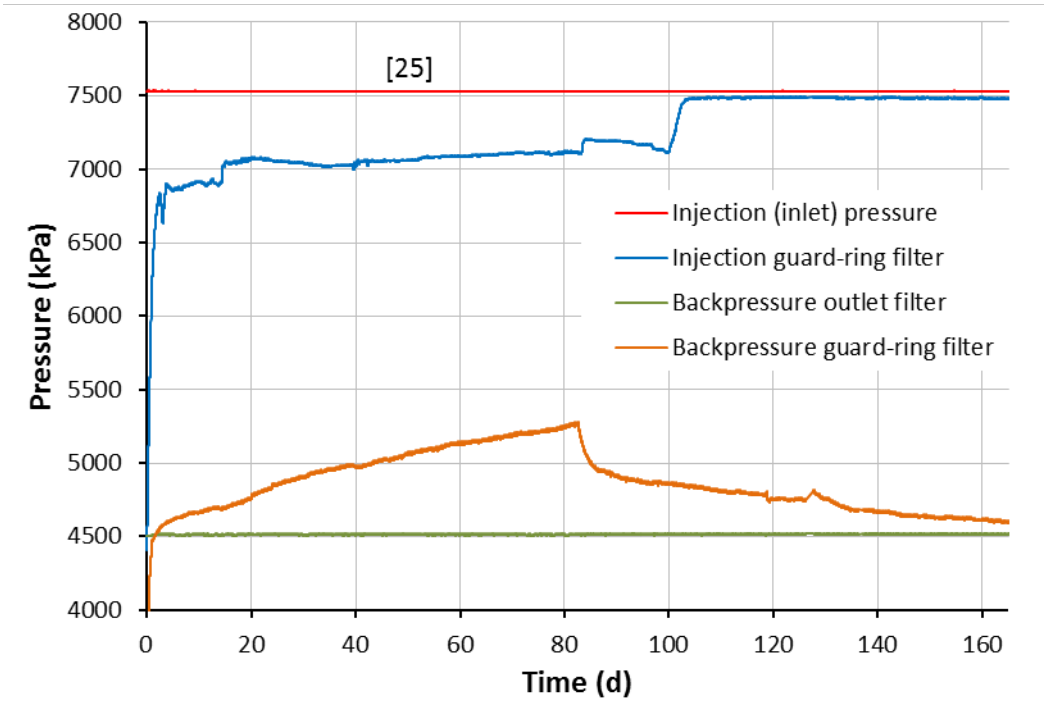

Figure 4-35 Evolution in pressure within sample COx-1 following the reinjection of gas, stage [25]. The inflections in the guar ring response are symptomatic of the opening and closing of unstable gas pathways.

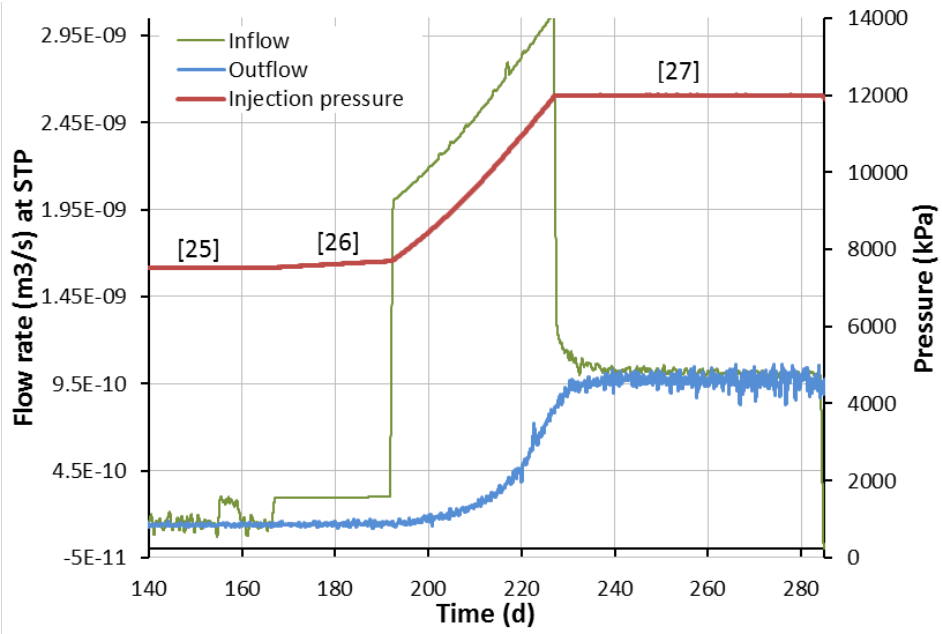

Figure 4-36 Evolution in flow into and out of the sample as gas pressure gradient is increased across the sample.

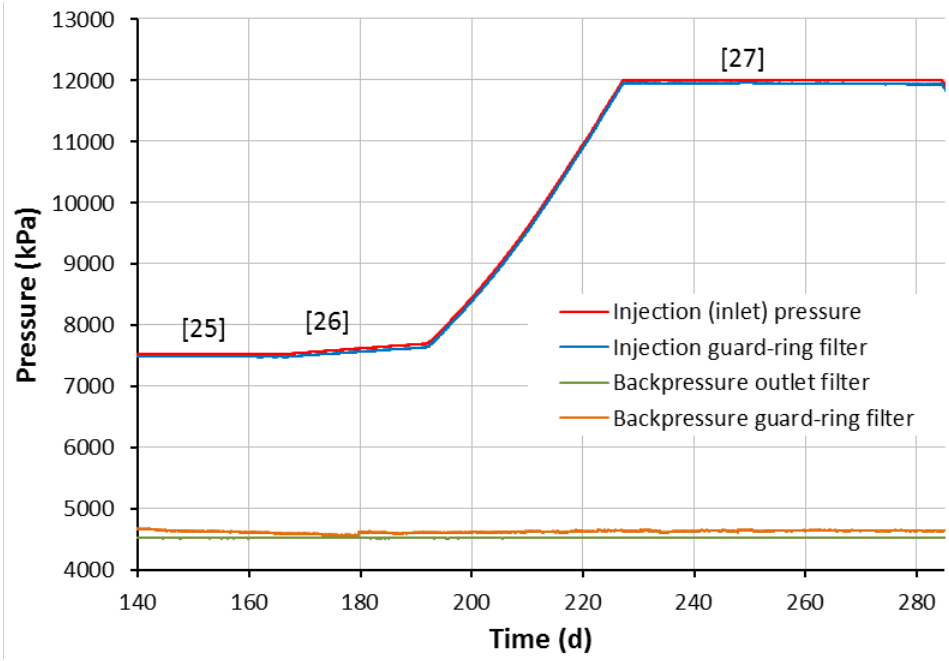

Figure 4-37 Evolution in pressure for sample COx-1 from 140 days onwards. Injection pressure guard ring tracks gas pressure while backpressure guard-ring appears insensitive to the change in gas pressure gradient.

At day 167 the injection pressure is slowly increased, over the following 60 days, to the next target value of 12.0 MPa (Figure 4-36 and Figure 4-37). During this time flux out of the specimen gradually increases approaching a well-defined asymptote at around 240 days. During this phase of gas testing the injection guard-ring closely tracks the pressure in the inlet filter, suggesting very little if any pressure drop exists between them. In contrast, the backpressure guard ring shows no sensitivity to the change in gas pressure gradient and continues the negative trend begun in Figure 4-47, reaching an asymptote value close to that of the back pressure filter. Given this filter was able to sustain a significant pressure differential and that its behaviour from day 83 exhibits no correlation to the gas pressure gradient, it provides strong evidence to confirm the sheath integrity (4.1.3.3).

The steady state data from stages [25] and [26] are presented in Table 4-3 and has been plotted against data from the first gas cycle (Figure 4-38). Inspection of the graph indicates little change in volumetric gas flow rate between test cycles, suggesting that the hysteresis observed between stages [19] and [21] has been nullified by the reinjection of water. Under these conditions, this observation suggests the gas has little permanent impact on the structure and fabric of the clay.

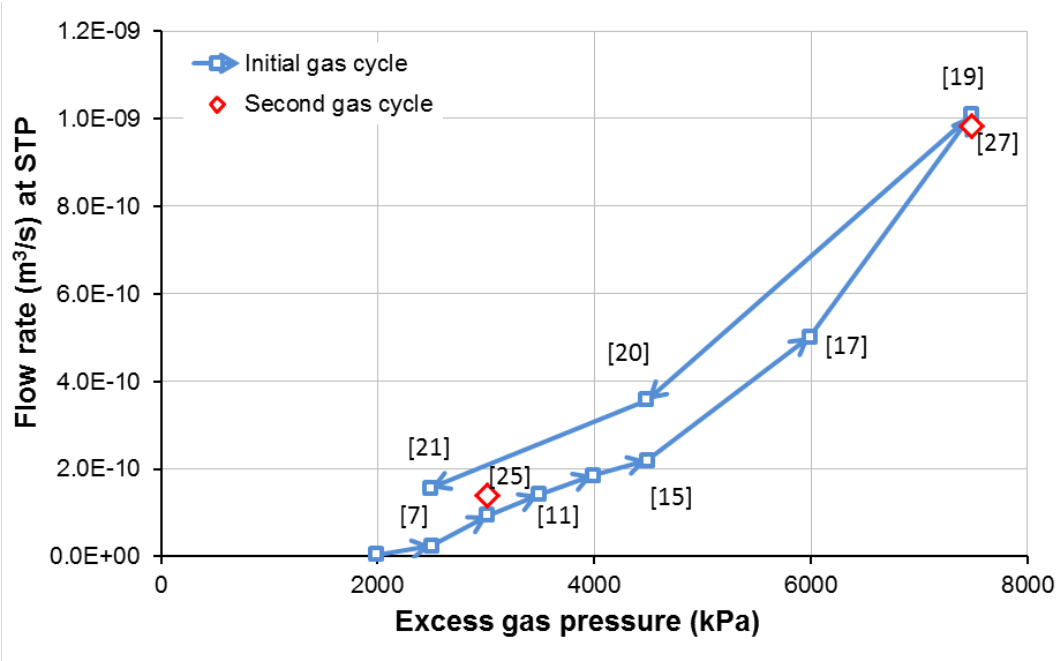

Figure 4-38 Steady state flow rates plotted against excess gas pressure for both gas injection cycles, stage [6] to [21] and [25] to [27] respectively.

4.1.5.1 Further evidence for dilatancy

Figure 4-39 shows a plot of out flow and volumetric strain plotted against time for test stages [25] to [27] inclusive. Strain is calculated based on the pre-test volume of the sample and the cumulative change in the confining system volume. While this approach is less refined than measurements from more complex triaxial systems, it can be used to identify systematic trends. The negative slope of the strain response is symptomatic of an increase in sample volume i.e. dilation. There is a clear correlation between the increase in outflow and sample volume from day 195 onwards, as gas flow out of the sample begins to increase. As outflow asymptotically approaches steady state, volumetric strain plateaus, and the system enters a quasi-steady state. These results are in general agreement with those presented in Figure 4-29 for COx-1 and the triaxial data from Figure 4-21.

By cross plotting volumetric strain against STP flow rate the correlation between flow and sample volume becomes apparent (Figure 4-40). However, the initial response at low volumetric strains suggests that for low gas entry pressure samples like COx-1, very small gas flows may be possible without significant dilation of the clay. However, the composition and limited resolution of the strain data in these tests undermines rigorous interpretation of the data during this phase of testing. As the sample approaches steady state, volumetric strains begin the plateau at an average value of around 0.5%. Interestingly, as flux across the sample remains fairly constant, the core appears to undergo some form of stress relaxation. The cause for this response remains unclear but may stem from time dependent processes related to local reorientation of the clay fabric adjacent to conductive gas pathways. Alternatively, leakage from the confining system may also play a factor though this seems unlikely as the pump piston would be traversing the same section of barrel as that experienced during the initial dilation response.

Either way, when viewed in its totality, this data provides further compelling evidence for the movement of gas by pathway dilation.

4.1.5.2 Localisation of gas flow

Upon removal from the apparatus, sample COx-1 was submerged in glycerol and gently heated to promote the release of gas. Figure 4-41 shows two images of gas evolved from the injection

and backpressure faces of the sample. Visual inspection clearly indicates a lower density of gas pathways on the inject face compared to that of the backpressure end. Intuitively, this is to be expected and is symptomatic of an expanding network of pathways which fan out as they propagate through the core. While this method of observation is not fully quantitative, it strongly suggests gas flow is localised within the clay. This observation supports the early results describing the evolution of guard ring pressures, the time dependent and non-uniform distribution of flow and the anisotropy in the strain measurements reported by Cuss and Harrington (2012). It should also be noted that no discharge of gas was observed in a control test performed on a 'fresh' section of intact core.

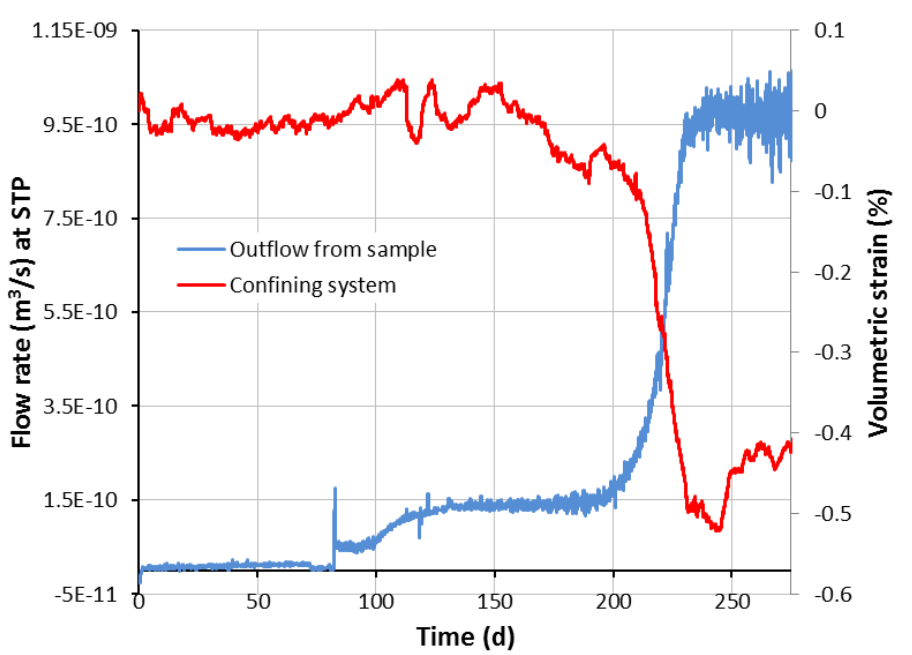

Figure 4-39 Out flow and volumetric strain plotted against time. Volumetric strain is estimated from the pre-test volume of the sample (Table 2-1) and the change in confining system volume. Negative strain represents dilation of the sample.

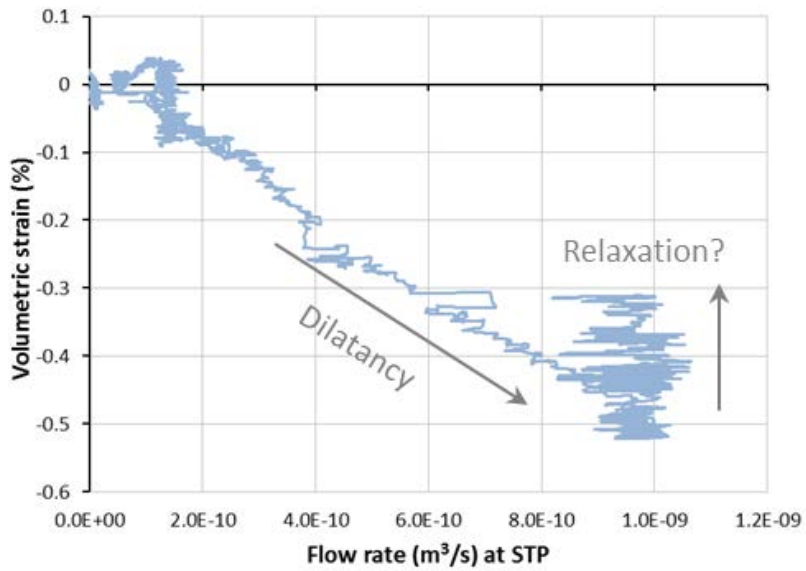

Figure 4-40 Volumetric strain plotted against STP flow rate for COx-1 showing a clear correlation between major gas flow and expansion (dilation) of the sample.

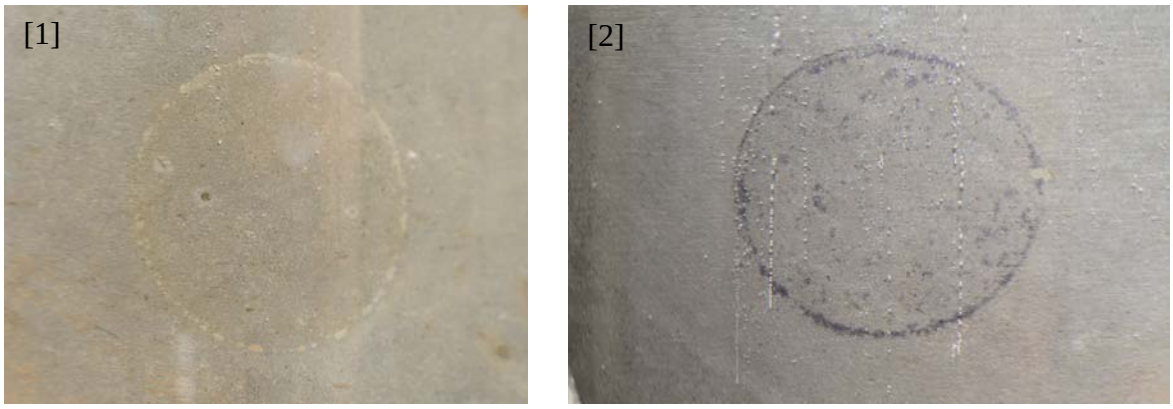

Figure 4-41 Gas discharged from sample COx-1 following submersion and gentle heating in a glycerol bath. [1] = injection face; [2] = backpressure face.

4.2 CALLOVO-OXFORDIAN CLAY SAMPLE 2 (COX-2)

4.2.1 Consolidation behaviour

A two-step consolidation test was carried out after an initial equilibration period of 31 days with the confining pressure held at 9.5 MPa. In the first step the confining pressure was raised to 11 MPa for 8 days and in the second step it was raised to 12.5 MPa for 15 days. Instantaneous flow rate and net cumulative flow volume data were collected, Figure 4-42.

Examination of the data clearly shows that at the onset of testing there is a rapid uptake of water by the specimen as it resaturates. This flux progressively declines with time, such that by around day 18, the net flow of water into the specimen is practically zero. Unlike in test COx-1, no data was available from the confining system due to a small background leak from the control pump. However, analysis of data from stage [1] indicates a net volume change of around 2.54 ml during resaturation. This is somewhat larger than the initial estimate of gas volume derived from the geotechnical data (Table 2-1), but this may in part relate to errors in the initial estimate (which is based on the moisture content of off-cut material and an assumed value for the grain density), or, more probably, reflects the fact that the sample underwent a higher degree of swelling during restauration.

Analysis of the consolidation data based on the total volume of fluid expelled from the specimen at the end of each step is presented in Table 4-4, along with the data from test COx-1 for comparison. Following each increment in confining stress specimen COx-2 exhibits a very small reduction in volume. Values for drained bulk modulus are therefore reasonably high, ranging from 1490 MPa to 1759 MPa, reflecting the indurated nature of the material. As with specimen COx-1, these values suggest that the specimen has not been subject to significant damage from de-stressing during sampling, transportation or specimen preparation. Young's modulus values were found to range from 1764 MPa to 2092 MPa.

Comparison of the data in Table 4-4 indicates specimen COx-2 is somewhat more compressible than specimen COx-1, exhibiting larger volumetric strains for a given change in confining stress. This supports the theory that COx-2 underwent a higher degree of swelling during stage [1] which would then explain the discrepancy between the measured inflow and the initial estimate for the gas saturation. While there is some degree of variance in the calculated parameters for each test specimen, the numbers are relatively similar which is to be expected since both samples came from neighbouring sections of the same core barrel.

Stage no.	Ave. effective stress (MPa)	Void ratio (at end of stage)	Volumetric strain (%)	Drained compressibility $\beta/10^{10}$ (Pa^{-1})	Drained bulk modulus (MPa)	Young's modulus (MPa)
Data for COx-1						
1	5.0	0.175	-	-	-	-
2	6.5	0.174	0.07	4.4	2262	2629 [1825]
3	8.0	0.173	0.16	6.4	1574	1870 [1700]
Data for COx-2						
1	5.0	0.193	-	-	-	-
2	6.5	0.192	0.09	5.6	1759	2092 [1600]
3	8.0	0.191	0.19	6.7	1490	1764 [1450]
Data for COx-3						
1	5.0	-	-	-	-	-
2	7.0	-		5.3	1902	2334 [-]
3	8.1	-		4.7	2133	2381 [-]

Table 4-4 Provisional consolidation data for test specimens COx-1, -2 and -3 during test stages [2] and [3]. The start value for void ratio [1] is based on the pre-test measurement. Values for Young's modulus are based on a Poisson's ratio of 0.3 (Wileveau and Bernier, 2008). Values in parentheses are derived from finite element modelling. Data for test COx-2 and -3 are provisional as testing is on-going at the time of writing.

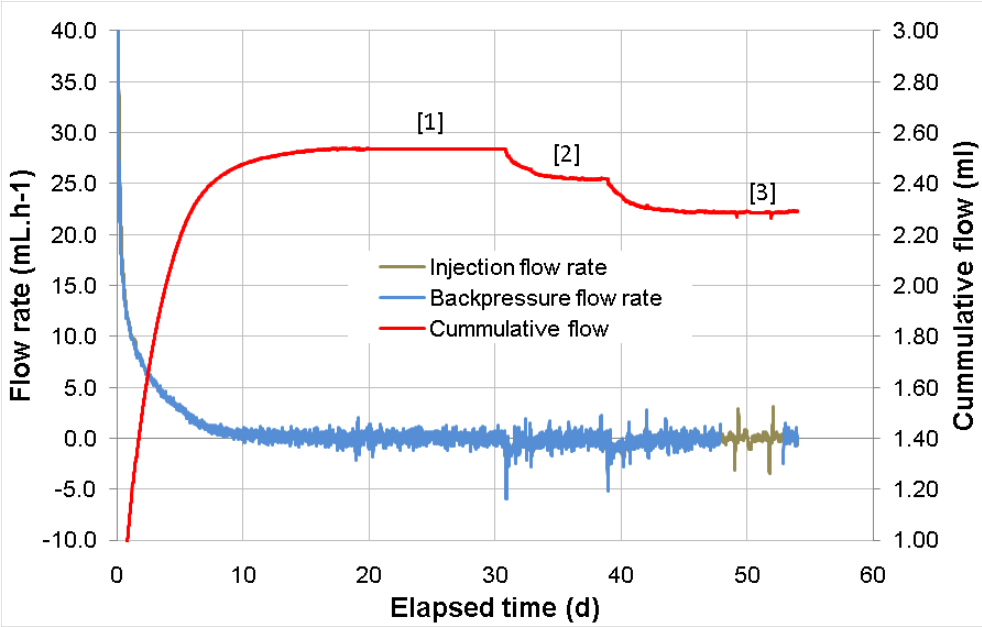

Figure 4-42 Cumulative flow from backpressure system from test stages [1] through [3] for sample COx-2. The backpressure response shows well defined transients associated with drainage of the argillite as confining stress is increased. The cumulative flow data has been edited between day 20 and 31 to correct for a pump problem.

As before, a finite element coupled deformation and porewater flow model of the experimental configuration was created to simulate test COx-2. The two steps were found to differ slightly in the parameters required to best fit the data and so have been interpreted separately. The hydraulic anisotropy derived from the values from the hydraulic tests on all three samples (2.65:1 radial to

axial) has been maintained for these models and a Poisson's ratio of 0.3 has been used throughout. The value of the Young's modulus was adjusted to fit to the magnitude of the net flow volume in each step whilst the permeability was adjusted to fit the transients.

The first step was fitted using an axial permeability of 2.5×10^{-21} m^2, a radial permeability of 6.62×10^{-21} m^2, and a Young's modulus of 1600 MPa. From equations (6) and (7) it is found that a Young's modulus of 1600 MPa corresponds to a specific storage of 8.1×10^{-6} m^{-1}. Figure 4-43 compares output from this model with the data from the test.

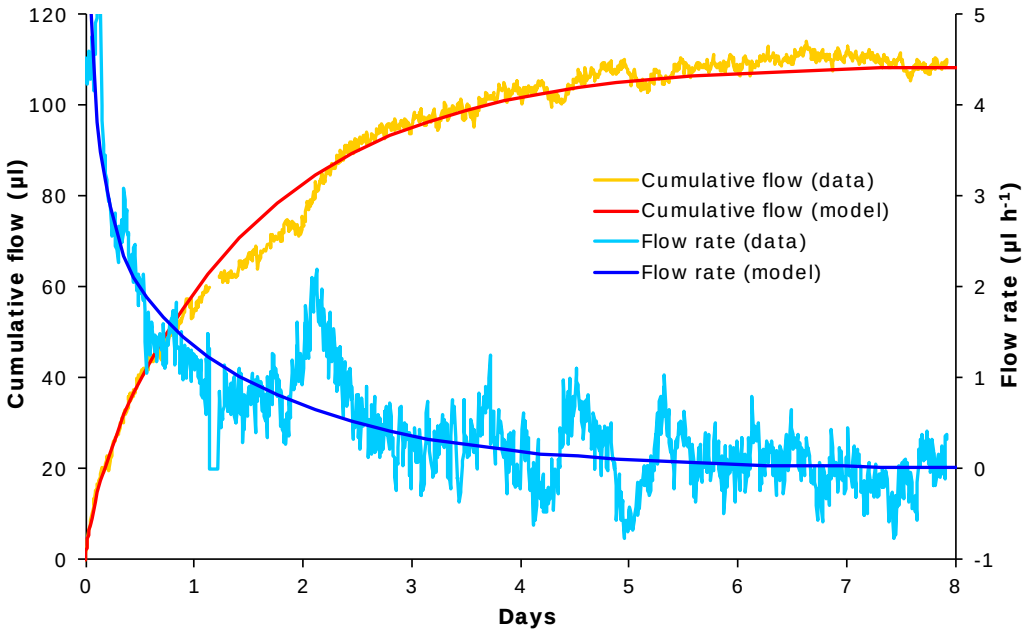

Figure 4-43 Comparison on model output to test data for the first step of the consolidation test on sample 2.

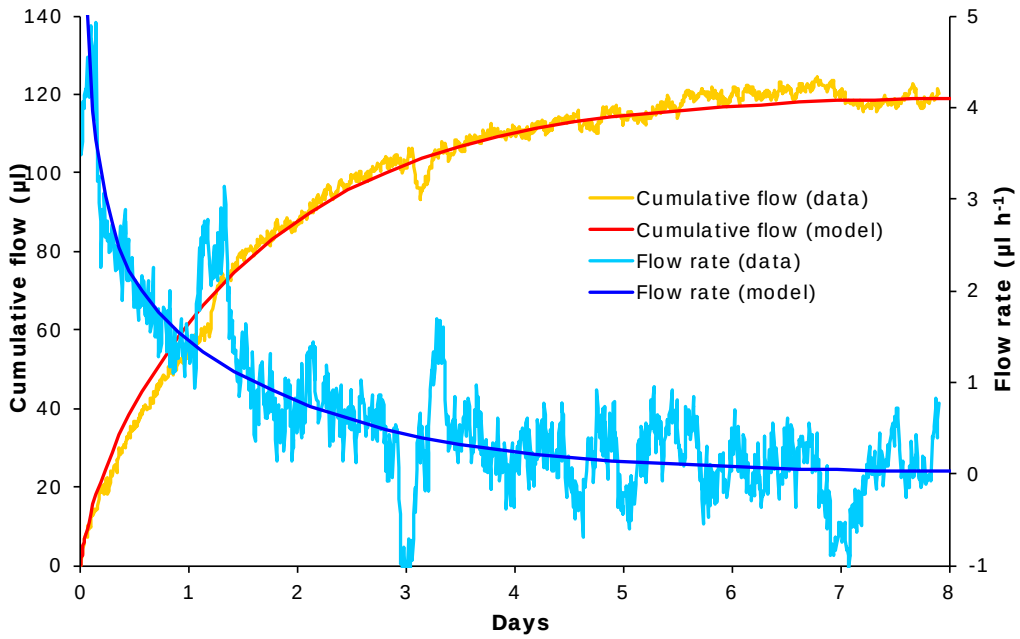

Figure 4-44Figure 4-44 Comparison on model output to test data for the second step of the consolidation test on sample 2.

The second step was fitted using an axial permeability of 2.5×10^{-21} m^2, a radial permeability of 6.62×10^{-21} m^2, and a Young's modulus of 1450 MPa, corresponding to a specific storage of 8.9×10^{-6} m^{-1}. Figure 4-44 compares output from this model with the data from the test. It appears that the permeability increases very slightly with the increase in confining pressure, but there is a small reduction when the hydraulic test is conducted. The estimates of specific storage derived

from the fitted values for Young's Modulus are slightly higher than the value found from the hydraulic test.

4.2.2 Hydraulic test

For the hydraulic test the confining pressure was maintained at a constant level of 12.5 MPa whilst the porewater pressure at the back pressure filter was kept at 4.5 MPa. The pressure at the injection filter was raised to 7.5 MPa for 21 days after which it was returned to 4.5 MPa. Flows at injection and backpressure filters were monitored together with the pressures at the two guard rings. A finite element porewater flow model of the experimental configuration was created to simulate the test and it was found that a good fit to the flow rate data could be obtained by setting axial permeability to 1.6×10^{-21} m^2 and radial permeability to 14.0×10^{-21} m^2, with a specific storage of 6.0×10^{-6} m^{-1}. Figure 4-45 and Figure 4-46 show comparisons of the model output with these parameters to the data for guard ring pressures and filter flow rates respectively. It can be seen that the model pressures are too high for both the injection and backpressure guard rings and the model parameters have been chosen as a compromise. The injection guard ring data imply a lower anisotropy in the permeability whilst the backpressure guard ring data imply a greater anisotropy.

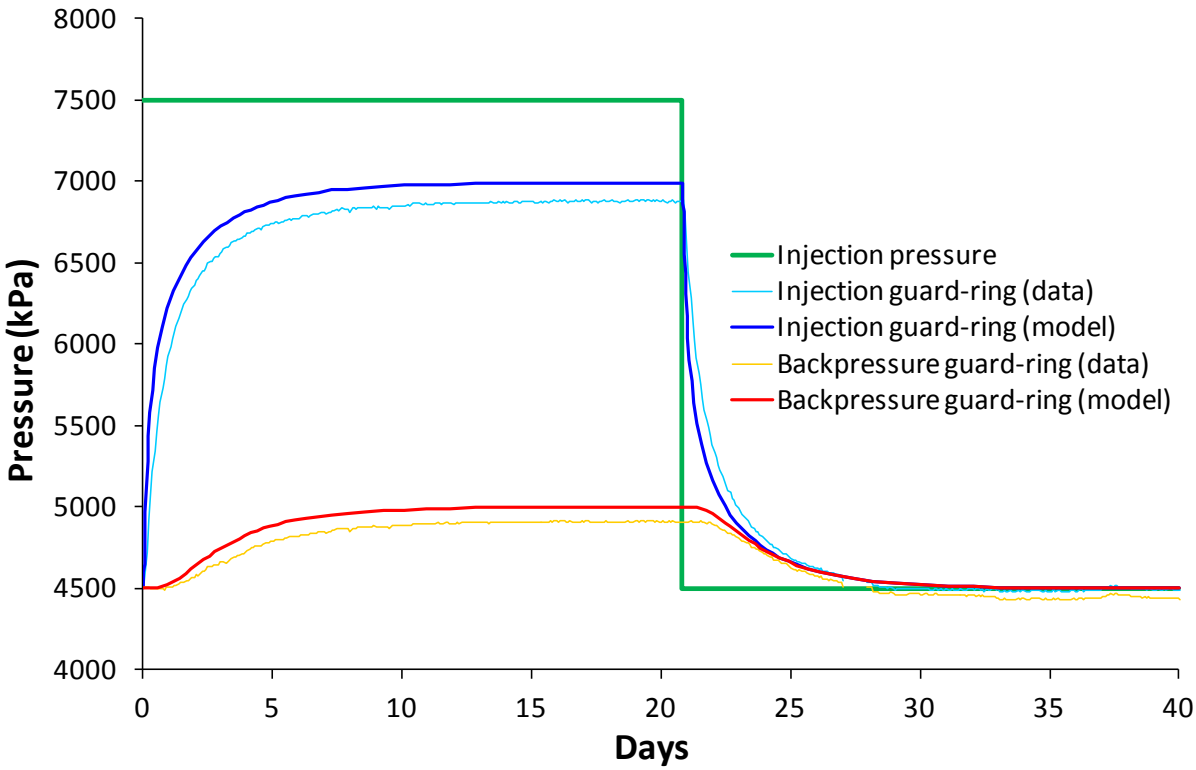

Figure 4-45 Comparison of observed guard ring pressures with the model simulation of the hydraulic test on sample 2.

The apparent differences in anisotropy of the permeability indicated by the guard ring data can be accommodated only by introducing more than a single rock type into the model. Two alternative models were constructed. In the first the sample was divided arbitrarily into separate rock layers half way along its axis. The rock properties of the two layers were set to the same values except that the radial permeability of the layer at the injection end was set to 8.8×10^{-21} m^2 and at the back pressure end to 22.4×10^{-21} m^2. This corresponds to an anisotropy in the permeability of 5.5 at the injection end and 14 at the back pressure end. The output of this model is compared to the guard ring pressure data and the flow rate data in Figure 4-47 and Figure

4-48. It can be seen that this model has a much improved fit to the guard ring data with very little change to the fit to the flow rate data.

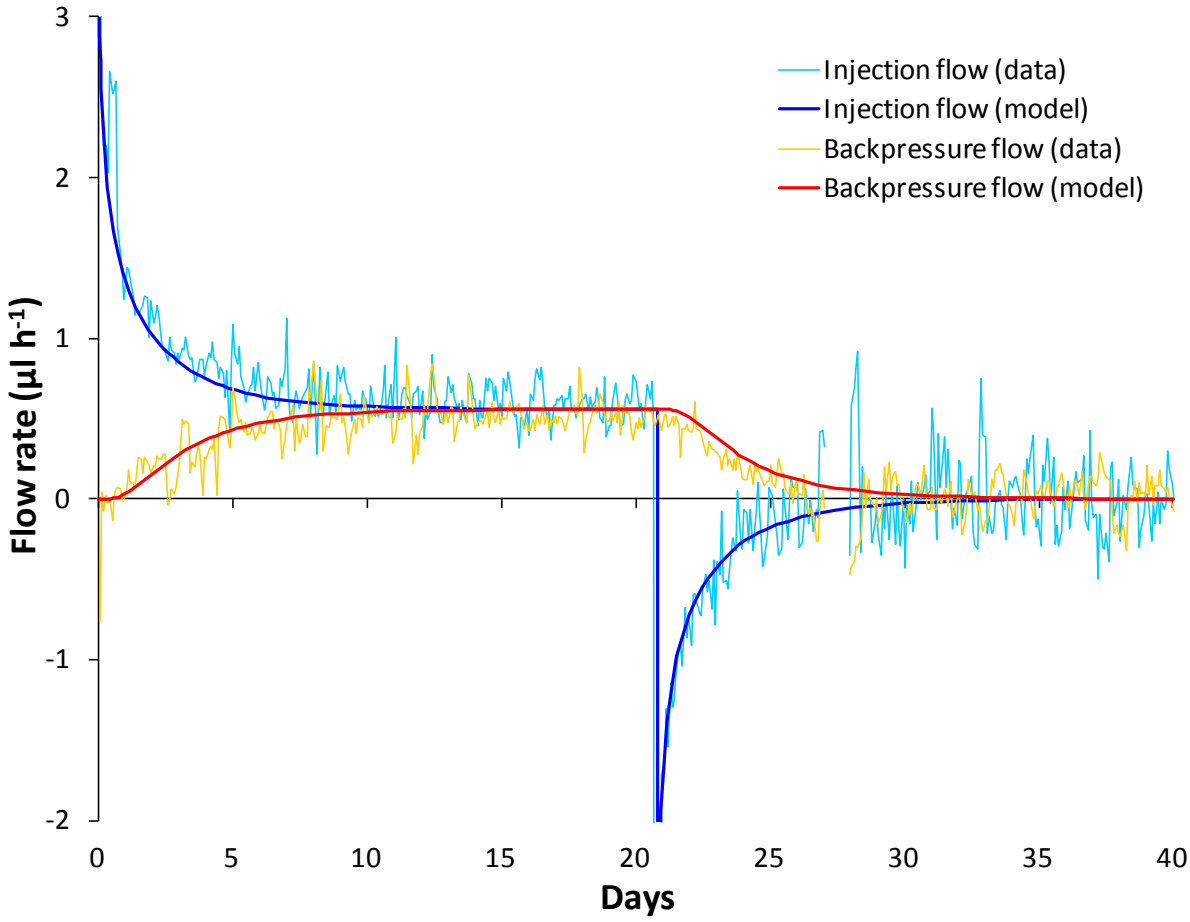

Figure 4-46 Comparison of observed flow rates from the injection and back pressure filters with the model simulation of the hydraulic test on sample 2.

The second alternative model adopted the approach of the alternative model for the first sample, having isotropic properties for the clay itself and adding thin surface leakage layers at either end of the sample. Thus the sample is given a permeability of 1.6×10^{-21} m^2 and a specific storage of 6.0×10^{-6} m^{-1}. Setting the injection surface transmissivity to 1.2×10^{-16} $m^2 s^{-1}$ and the backpressure surface transmissivity to 2.3×10^{-16} $m^2 s^{-1}$ gave fits to the data that were indistinguishable from those shown in Figure 4-47 and Figure 4-48. As for sample COx-1, with this model the anisotropy of the clay is undetermined, though with an upper limit of 5.5, since any anisotropy came be compensated for by adjustments to the surface transmissivities.

The heterogeneity introduced during the modelling exercise clearly illustrates the important role small-scale features play in determining the pressure distribution within the specimen. While this approach was not adopted for test COx-1, it may go some of the way to help explaining the low gas entry pressure and non-ideal response of the downstream guard-ring observed during gas test. It is also interesting to note, that the introduction of a bi-modal model had little effect on the advective flux.

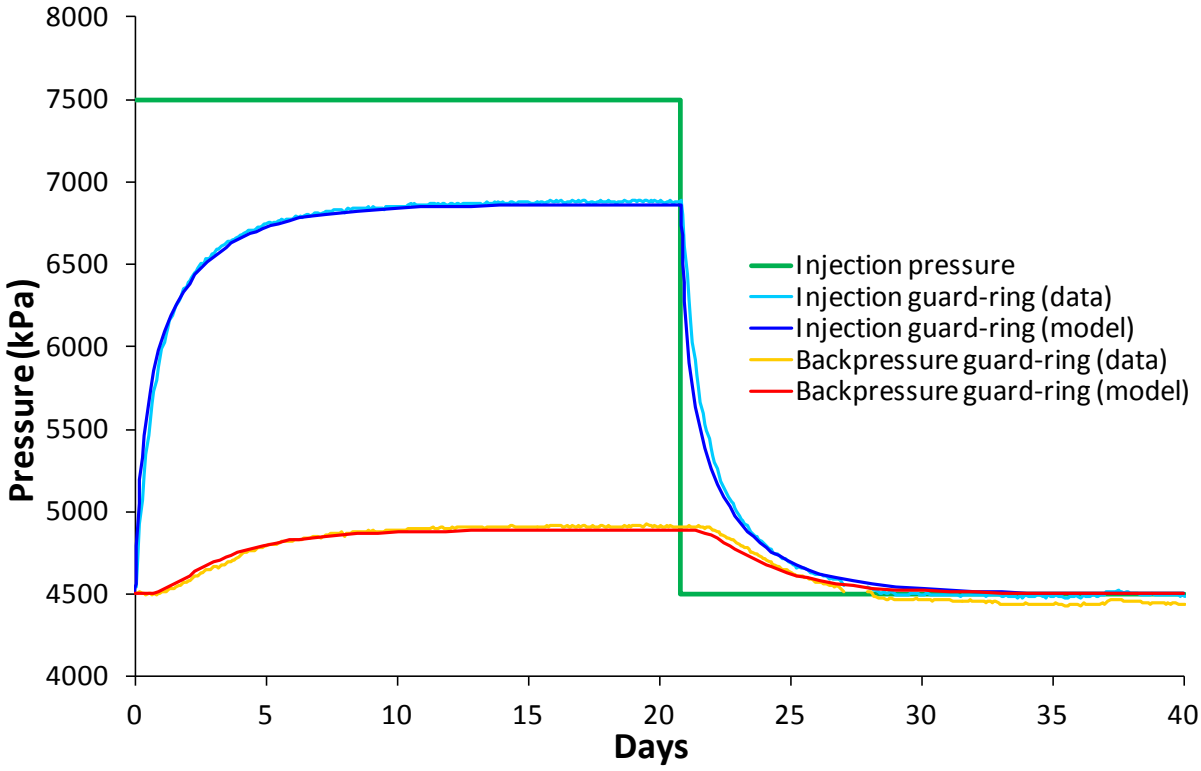

Figure 4-47 Comparison of observed guard ring pressures with a model simulation of the hydraulic test on sample 2 using a two layer representation of the sample.

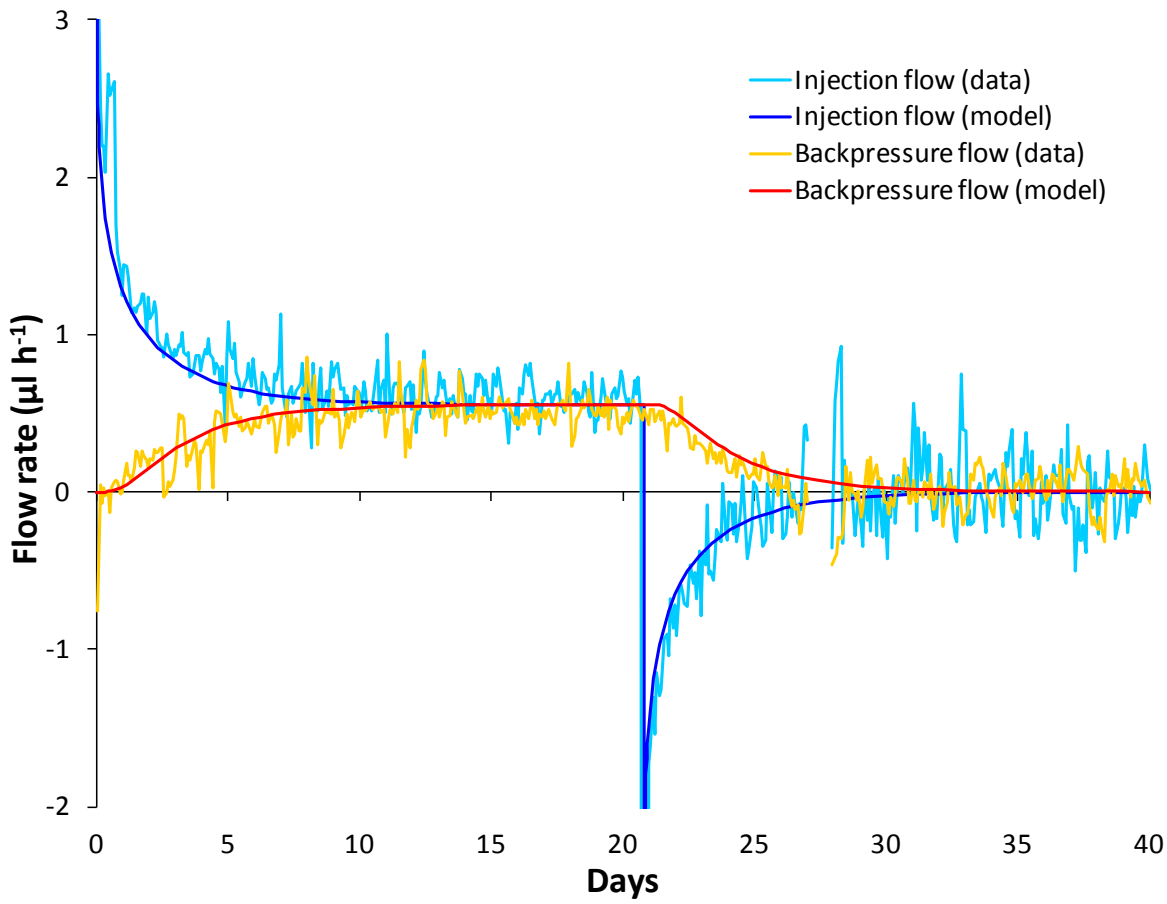

Figure 4-48 Comparison of observed flow rates from the injection and back pressure filters with a two layer model simulation of the hydraulic test on sample 2.

4.2.3 Gas injection

In a similar fashion to test COx-1, gas pressure was initially increased in a stepwise manner from 7.5 MPa, stage [6], to 11.25 MPa, stage [20], during the first 510 days of gas testing. At each stage, the injection pressure was maintained constant while flux into and out of the specimen monitored with time. During the first constant pressure gas stage [6], a small emergent flux of fluid was noted (Figure 4-49), which was also accompanied by an increase in both guard-ring pressures. This behaviour can be simply explained by the displacement of residual water, by gas, from the injection system/filter. By the end of the test stage flux and guard ring pressures all return to their original values. Gas pressure was then held constant at 7.5 MPa until day 171.8 with no obvious sign of gas flow (outflow values and guard ring pressures exhibit no conspicuous changes in behaviour).

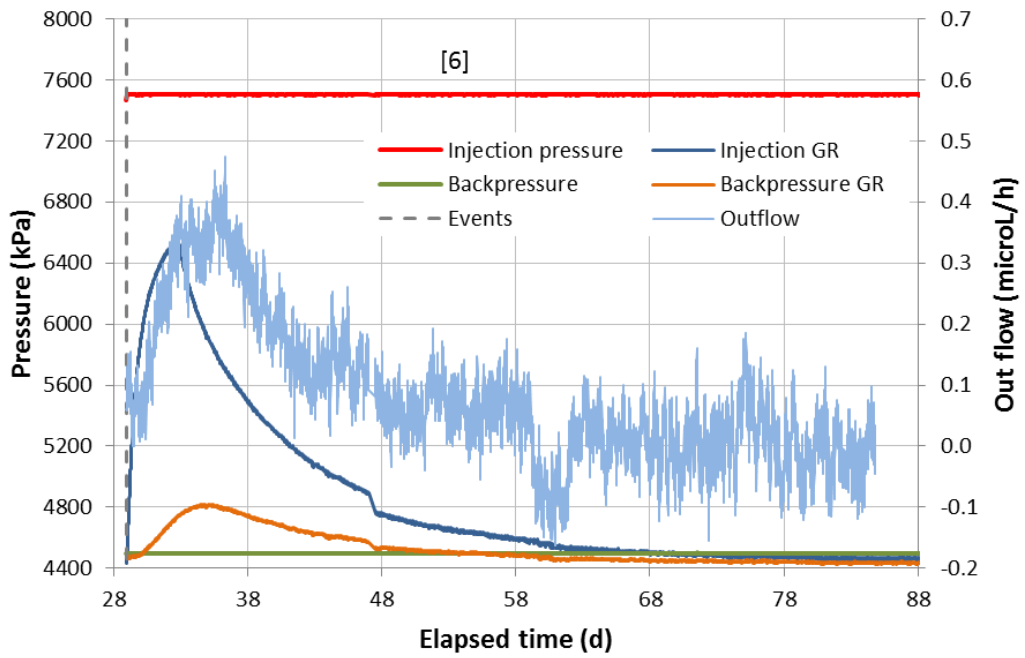

Figure 4-49 Plot showing initial slug flow through specimen COx-2 during test stage [6].

Gas pressure was then slowly increased to 8.0, 8.5, 9.0, 9.5, 10.0, 10.5 and lastly 11.25 MPa over a 338 day period. At each interval, gas pressure was held constant for between 17 and 326 days in order to observe the system response (Figure 4-50). During stages [6] through [16] there is no conspicuous sign of gas entry or breakthrough with guard ring pressures remaining fairly constant and flux out of the sample approximately equal to zero.

As gas pressure in the injection filter was then slowly increased over a 19 day period, stage [17], to the next target pressure of 10.5 MPa, the injection guard ring data (Figure 4-51) shows a conspicuous change in behaviour as the system pressure begins to increase. A similar response is observed in the backpressure guard ring a few days later. It is difficult to determine the absolute flux out of the clay during this stage due to a small leak in the backpressure pump. However, examination of the outflow data shows no conspicuous inflections or changes in response, suggesting that, if any outflow was occurring, it was fairly constant in nature. By around day 450, the leak in the back pressure pump had been fixed and a small but measurable positive flow (i.e. discharge) is observed emanating from the sample (Figure 4-50).

As seen in previous tests, inspection of the guard ring data during this phase of testing indicates underlying time dependent behaviour, with the development of conductive pathways which vary temporally and spatially within the sample (signified by changes in slope of the guard ring pressure traces). It is interesting to note that the gradual increase in IGR pressure observed from around day 418 onwards, occurs at an injection gas pressure of 10.1 MPa. This is only 0.1 MPa

larger than the previous value which was held constant for in excess of 26 days. While superposition of time dependent phenomena cannot be totally ruled out, the observation demonstrates COx is able to withstand significant gas pressure gradients for extended periods of time prior to this point of gas entry. This latter quantity is therefore estimated to be in the region of 10.1 MPa for sample COx-2. This value is in close agreement with gas entry data from the Andra/BGS triaxial test (Cuss and Harrington, 2012) which yielded a similar value of 10.2 MPa.

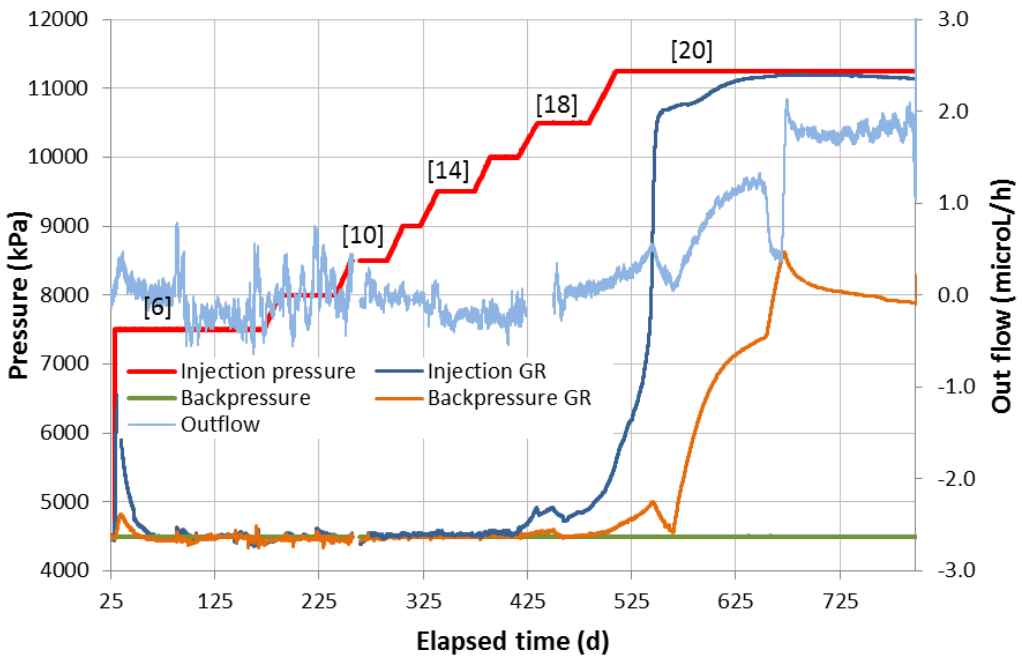

Figure 4-50 Plot showing the evolution in guard ring pressures and outflow due to changes in gas pressure gradient. The spike in data observed at around 257 days stems from the failure of the laboratory air conditioning system. However, it is clear from the GR response that this had no permanent effect on the behaviour of the claystone.

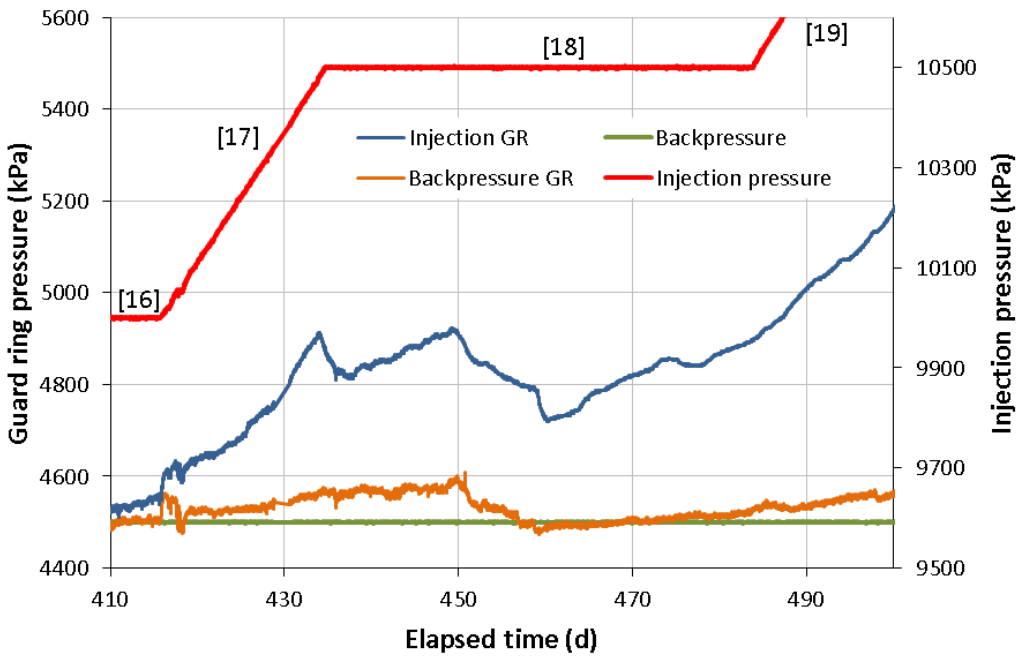

Figure 4-51 Detailed plot of guard ring and injection pressure evolution as gas begins to migrate through the sample.

By day 460, flux out of the sample asymptotes and thereafter remains fairly constant for the remainder of stage [18]. As gas pressure is then increased during stage [19], pressure in the injection guard ring filter begins to rise. This is accompanied by a much smaller increase in pressure in the backpressure guard ring. During this time out flow from the sample also begins to increase. This response is interpreted as the drainage of water displaced from the injection guard ring by the invasion of gas (Figure 4-52, zone A).

The injection pump is switched from constant flow rate to constant pressure mode (day 510) and the value maintained constant at 11.25 MPa. At around day 540 the rate of pressure increase in the IGR circuit begins to increase. This is followed 5 days later by a spontaneous reduction in both outflow and BGR pressure (Figure 4-52, zone B), suggesting most of the water from the IGR circuit has now been replaced by gas. A network of conductive gas pathways then continues to develop, reaching the BGR filter at around 565 days, inferred by the rise in filter pressure (zone C). Water then begins to drain from this circuit, resulting in a second increase in measured outflow. At around day 579, IGR pressure increases again, leading to a temporary asymptote close to the injection pressure, before declining slightly, for the remainder of the stage. These responses are symptomatic of the time-dependent increase in the number and/or conductivity of the nascent pathway network.

At around day 653, out flow decreases for a second time (zone D), thought to signify the end of water drainage from the BGR filter. Backpressure guard ring pressure then rapidly increases from day 654 onwards, reaching a peak value of 8.63 MPa at day 671, before slowly decaying to a projected asymptote of around 7.7 MPa. At day 669, out flow spontaneously increased, interpreted as the onset of major gas breakthrough (zone E). This yields a gas breakthrough pressure of 11.25 MPa. Thereafter, flux exhibited a minor peak, before entering a quasi-steady state condition.

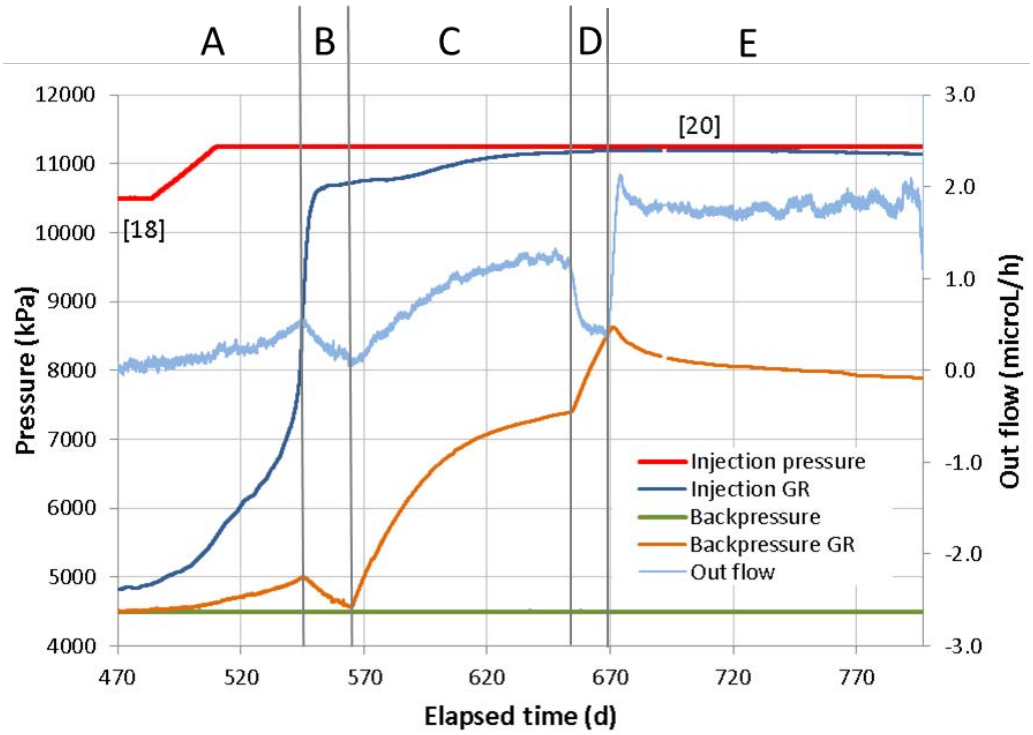

Figure 4-52 Sample COx-2: material response during gas entry and subsequent breakthrough. Zone index: A = dewatering of IGR filter; A-B = migration of gas across the sample; C = out flow dominated by drainage of water BGR filter; D = as BGR filter is drained of water gas pressure increases; E = gas breakthrough occurs.

As in previous tests, the volumetric strain before, during and after gas breakthrough has been calculated based on the pre-test volume of the sample and the change in confining pump volume (Figure 4-53). Like the data presented in Figure 4-29 and Figure 4-40, sample COx-2 shows evidence for sample dilation during the onset of gas and water flow. As with the data presented in Figure 4-40, COx-2 also appears to show some form of stress relaxation during steady-state (days 700 to 787) as volumetric strains reduce with time. This behaviour was not observed in high precision traixial tests and further work is required to better understand the coupling between gas flow and volumetric strain.

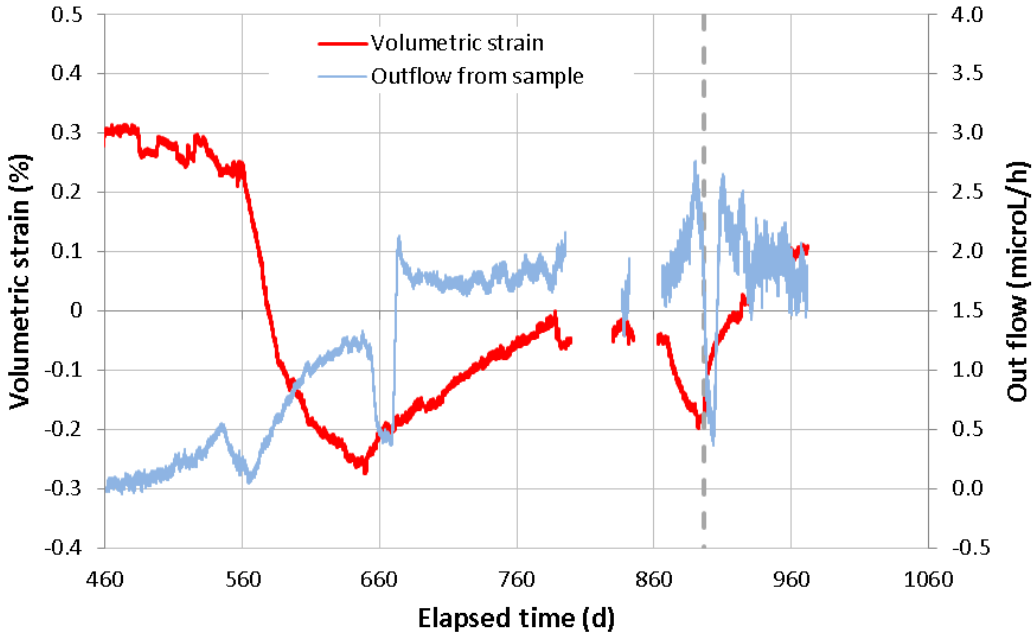

Figure 4-53 Sample COx-2: Out flow and volumetric strain plotted against time. Volumetric strain is estimated from the pre-test volume of the sample (Table 2-1) and the change in confining system volume. Negative strain represents dilation of the sample. The grey dotted line indicates the point at which confining stress was increased, stage [22].

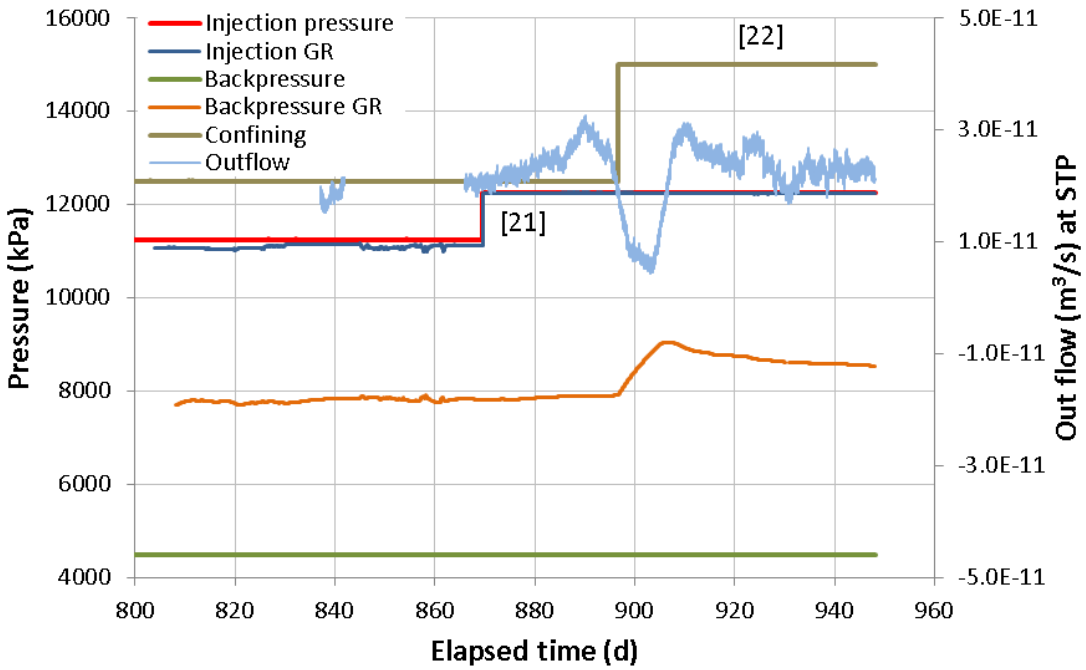

Figure 4-54 Sample COx-2: material response as gas pressure gradient and thereafter confining pressure are increased.

At the onset of stage [21], day 870, gas pressure in the inlet filter was increased to 12.25 MPa. This was followed by an increase in outflow, Figure 4-54, which peaked around day 890, before reducing to a quasi-steady state by the end of the test stage. This increase in outflow was accompanied by a second dilation event, Figure 4-53, which continued to evolve throughout the duration of the stage. At this point, confining stress was then increased to 15.0 MPa, stage [21], which, if fully transmitted to the conductive gas pathways, should be of sufficient magnitude to cause them to collapse and potentially reseal. The increase in confining stress (grey dotted line **Figure 4-53**) was accompanied by a spontaneous increase in volumetric strain (i.e. a reduction in sample volume) which continued to evolve for the following 100 days. By day 960, volumetric strain had reached an apparent asymptote of around 0.1%. During this time, outflow from the sample reduced by around 30% from 2.5 to 1.7 µl h^{-1}. While flux significantly reduced following the increment in confining stress, the data provides no clear evidence to suggest flow would ultimately asymptote at a zero flow condition. This suggests that a modest increase in confining is not sufficient to close the network of conductive gas pathways and that the interaction between gas permeability, dilatancy and confining stress is highly complex. As indicated above, further work is required to better understand these relationships.

4.2.4 Hydraulic test post gas injection

Upon completion of the gas test, all tubes and filters (including those in both guard ring circuits) were flushed with synthetic water to remove as much gas as possible. Injection and backpressure pumps were set to constant pressure mode at a calibrated value of 4.5 MPa. In/outflow and guard-ring pressure were monitored with time.

Figure 4-55 and shows the complex evolution of outflow and guard ring pressure response as sample COx-2 degasses following prolonged gas testing. While this stage is on-going, examination of the cumulative flow response exhibits a long duration transient response, suggesting an asymptote in flow at around day 250. Inspection of the guard ring data indicates rapid degassing occurs at the beginning of the stage with a higher rate of discharge at the injection end of the core (signified by a faster rate of guard ring pressurisation).

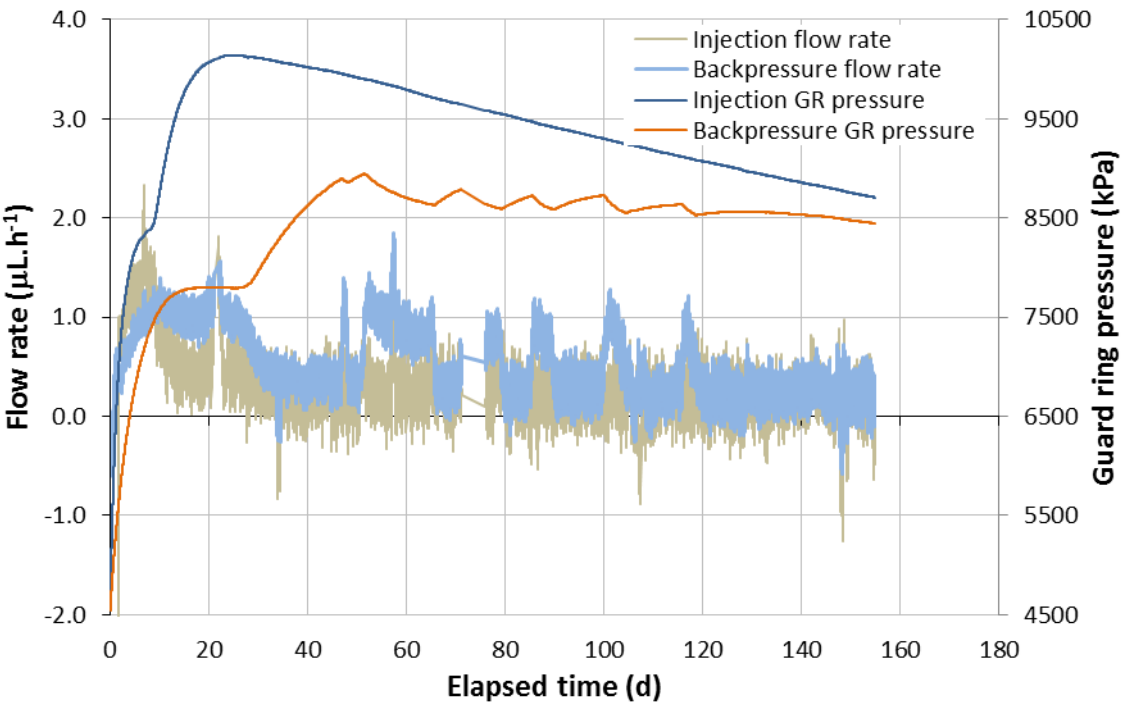

Figure 4-55 Evolution of flow and pressure after gas testing. Positive flux indicates flow out of the sample. Injection and backpressure filter pressures were maintained constant at 4.5 MPa during this stage of testing.

However, this is to be expected given the gas pressure gradient previously imposed across the sample. Around day 7 outflow to the injection filter spontaneous begins to decrease. This is accompanied by a second pressure transient resulting in a peak guard ring pressure of 10.14 MPa. Thereafter, injection GR pressure begins to decline in a linear manner which is mirrored in a small residual outflow to the injection filter.

Conversely, examination of the backpressure data clearly indicates outflow, rate of guard ring pressurisation and the absolute value of guard ring pressure are integrally linked, with changes in flow reflected in the other two responses. The asymptote in IGR pressure at around day 25 is followed by a spontaneous increase in BGR pressure, with flux out of the sample declining as gas preferentially flows to the backpressure GR filter. From day 60, the system appears to exhibit some degree of repeatability, with cyclic increases in backpressure guard ring followed by a breakthrough event, depressurisation and an increase in outflow. A cross plot of outflow to the backpressure filter versus the backpressure guard ring, Figure 4-56, illustrates this cyclic behaviour, with the plot comprised of a series of superimposed 'loops'. As gas drains to the BGR filter the pressure increases. During this time a residual outflow of gas (from background degassing of the sample) continues at a fairly constant rate. At a critical threshold pressure of around 8.72 MPa, gas begins migrates from the guard ring to the backpressure filter, resulting in a spontaneous reduction in GR pressure and an increase in outflow to the backpressure filter. As gas drains and the GR filter pressure declines, the pathways reseal (at around 8.53 MPa), flow returns to the residual degassing value, and the process begins again. The large differences in pressure between the backpressure and guard ring filters clearly demonstrates that very high gas pressure gradients exist within the clay and that much if not all of the drop in gas pressure (during advective gas flow) is within the last few millimetres (or less) of the clay.

While the test is on-going, the data indicates that advective gas transport remains possible in sample COx-2 at pressures above 8.72 MPa. While this is a little lower than the gas entry pressure quoted in Section 4.2.3 (10.1 MPa), it may reflect a range of issues associated with long term interactions between the clay and the gas phase. What is clear however is that the integrity of the seal between the platens and the sample remains intact and does not appear to act as a conduit for flow. Once testing draws to a conclusion, the asymptote of the guard ring pressures will provide important data on the anisotropy of the clay to gas flow and the distribution of gas pressure within the sample.

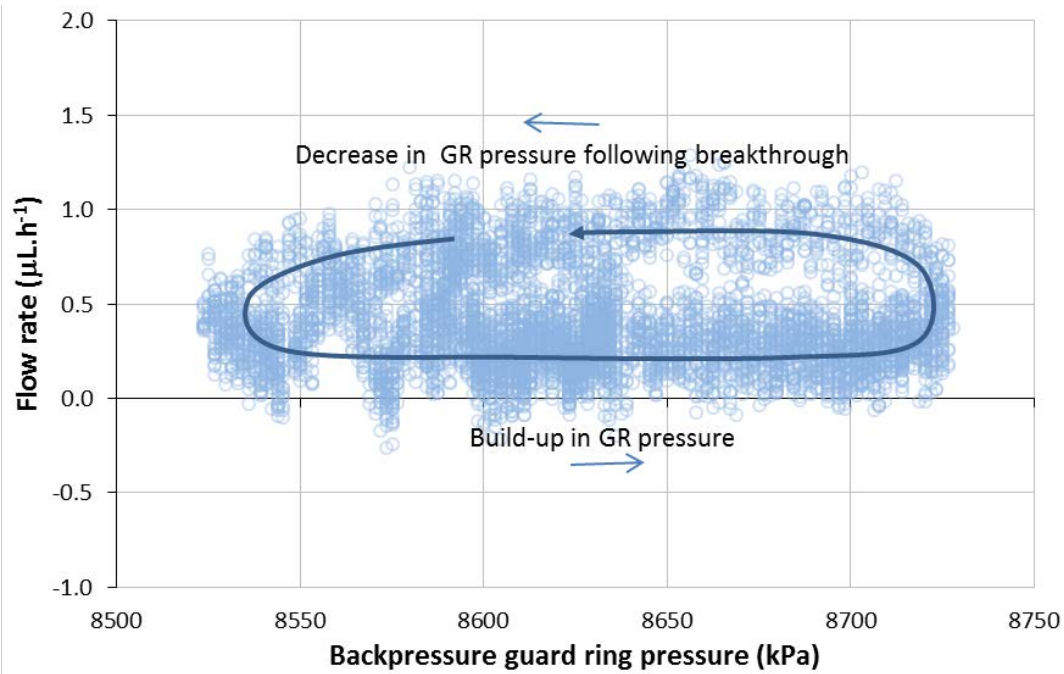

Figure 4-56 Cross plot of outflow against backpressure guard ring from day 60 to 120, showing cyclic behaviour between flow and GR pressure as the sample degasses.

4.3 CALLOVO-OXFORDIAN CLAY SAMPLE 3 (COX-3)

4.3.1 Consolidation behaviour

A two-step consolidation test was carried out after an initial equilibration period of 15 days with the confining pressure held at 9.5 MPa. In the first step the confining pressure was raised to 11.6 MPa for 6 days, test stage [2], and in the second step it was raised to 12.7 MPa for 8 days, stage [3]. Instantaneous flow rate and net cumulative flow volume data were collected.

Sample COx-3 has been taken with its cylindrical axis parallel to the bedding plane which makes the geometry of the test fully three dimensional. Unfortunately, the finite element code used for simulation of the consolidation tests on samples COx-1 and COx-2 treats only two dimensional and axisymetric problems, so it has not been possible to make a simulation of this sample. Analysis of the consolidation data based on the total volume of fluid expelled from the specimen at the end of each step is presented in Table 4-4

4.3.2 Hydraulic test

For the hydraulic test the confining pressure was maintained at a constant level of 12.5 MPa whilst the porewater pressure at the back pressure filter was kept at 4.5 MPa. The pressure at the injection filter was raised to 7.5 MPa for 16 days, stage [4], after which it was returned to 4.5 MPa, stage [5]. Flows at injection and backpressure filters were monitored together with the pressures at the two guard rings.

A 3D finite element model of porewater flow in the hydraulic test apparatus was created that included both the sample and the filters at either end. The symmetry of the experimental apparatus permits the model to consider just a quarter cylinder and flows into and out of the full system will be four times those obtained from this model. The material components and the mesh used are shown in Figure 4-57. It was assumed that the sample's bedding lay in the X-Z plane with the Y axis perpendicular to bedding. It can be seen that elements were included in the model to represent the end surfaces between the filters. These were initially given very low permeabilities so that the response of the sample alone could be considered. Further models were run with more conductive elements here to study the effects of leakages on these surfaces.

An initial model was run in which the clay sample was assumed to have an isotropic permeability and the value was adjusted to fit the data for flows into and out of the sample. The fit shown in Figure 4-58 was obtained using a permeability of 7.7×10^{-21} m^2 and a specific storage of 6×10^{-6} m^{-1}. It can be seen that a good fit has been obtained to the data. However, the model's predictions for the guard ring pressures are very poor as shown in Figure 4-59.

Since the sample is known to have bedding in the X-Z plane further models were run with the Y-axis component of permeability reduced to see if the fit of the guard ring pressure response to the data could be improved. Figure 4-60 and Figure 4-61 show results from a model with an anisotropy of 20, the X-Z plane permeability having been adjusted to fit the flow rate data. Here the X-Z plane permeability is 10^{-20} m^2 and the Y-axis permeability is 5×10^{-22} m^2. It can be seen that the guard ring pressure fit is in fact somewhat poorer than for the isotropic model.

It is apparent that the guard ring pressure data are incompatible with the models considered above and indeed the injection guard ring data in particular strongly suggest a highly permeable connection to the injection filter. To examine the effect of such connections further models were run in which the permeability of the surface zone elements was raised until improved fits to the guard ring pressures were obtained. The X-Z plane permeability of the sample was then adjusted to fit the flow data whilst maintaining the Y-axis permeability at 5×10^{-22} m^2 as in the previous model. Figure 4-62 and Figure 4-63 show the results obtained with the X-Z plane permeability at 4.5×10^{-21} m^2 after setting the injection surface zone transmissivity to 3×10^{-14} m^2s^{-1} and the backpressure surface zone to 8×10^{-16} m^2s^{-1}. Whilst this model shows a greatly improved fit to the guard ring data there remains a gradual increase in the back-pressure guard ring pressure that is

not reproduced by the model. One possible explanation would be that the back-pressure surface zone is gradually reducing in transmissivity over time.

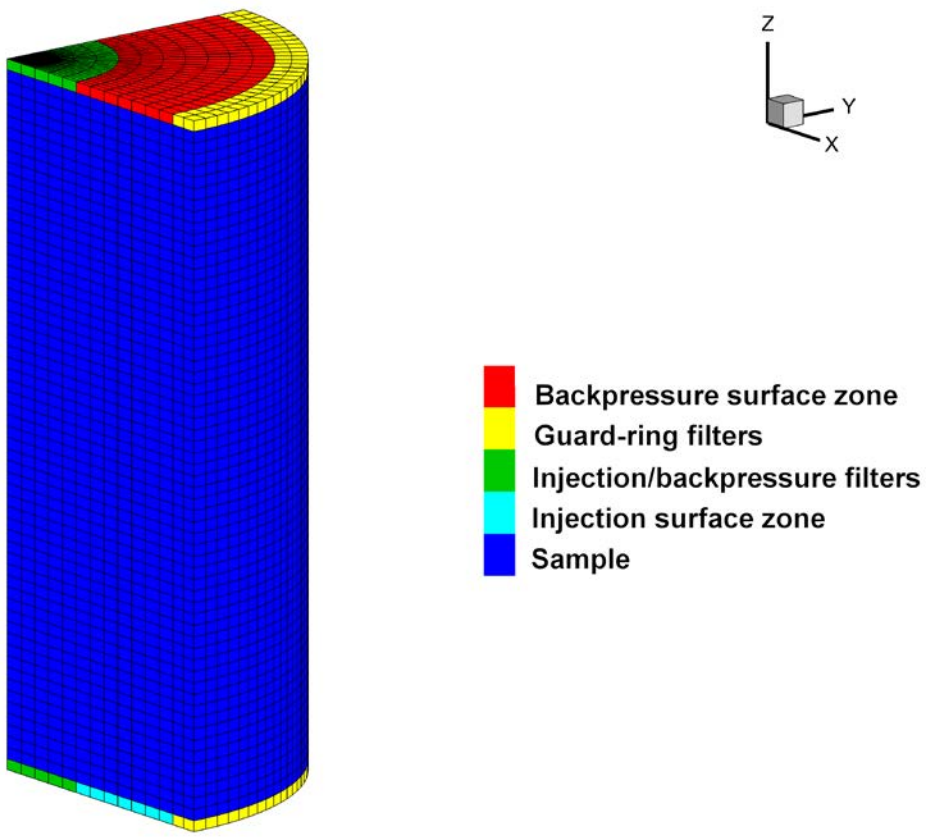

Figure 4-57 The material components and mesh of the quarter cylinder flow model used for simulation of the hydraulic test for sample COx-3.

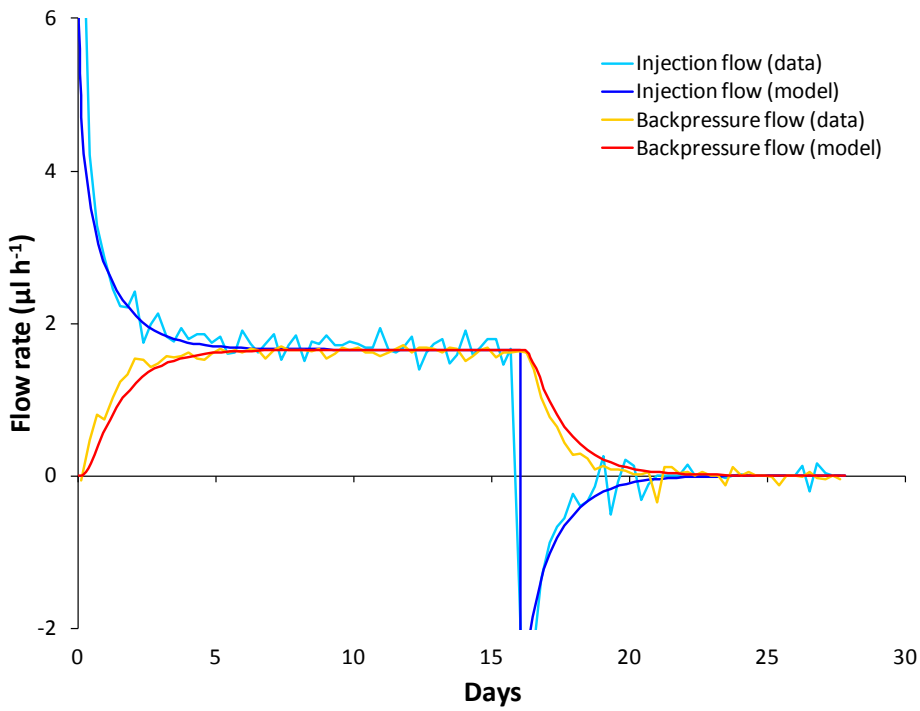

Figure 4-58 Comparison of an isotropic permeability model with flow data for sample COx-3.

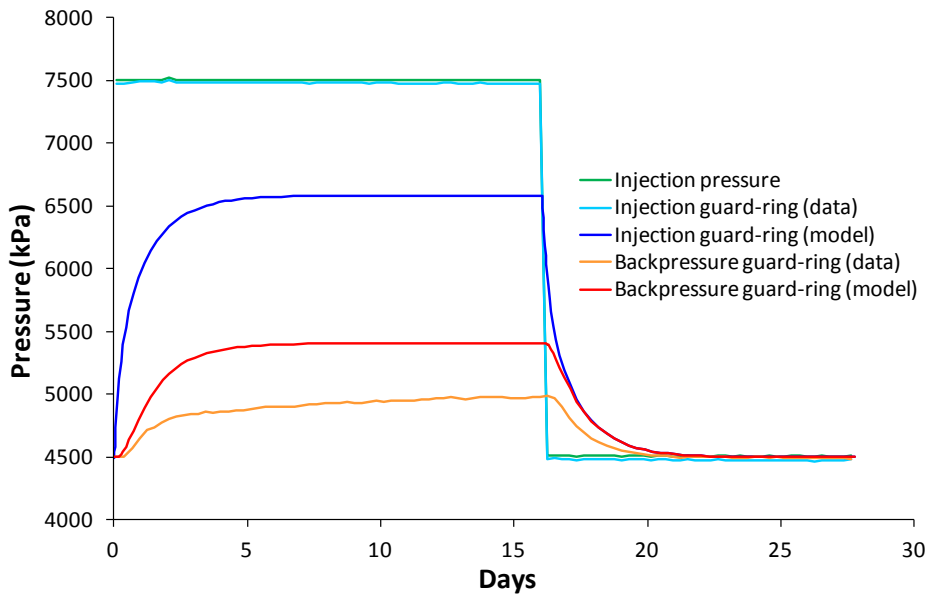

Figure 4-59 Comparison of an isotropic permeability model with guard ring pressure data for sample COx-3.

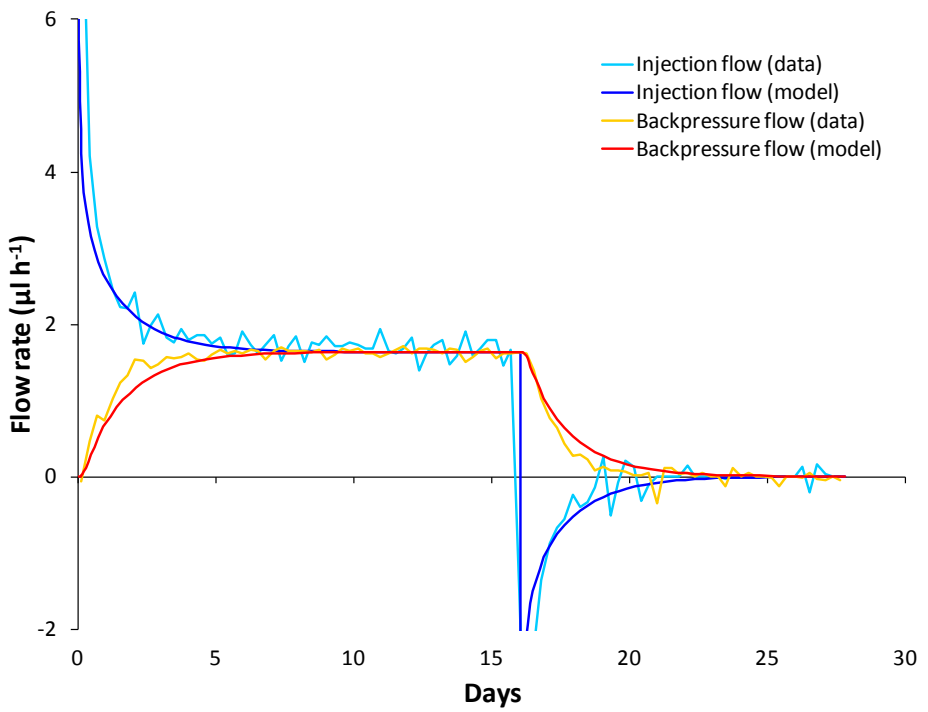

Figure 4-60 Comparison of an anisotropic permeability model with flow data for sample COx-3.

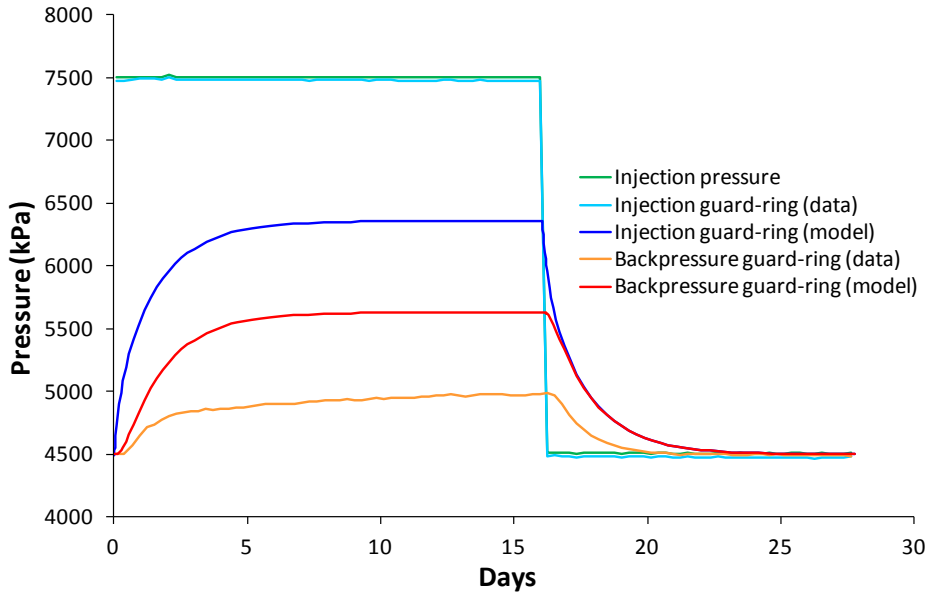

Figure 4-61 Comparison of an anisotropic permeability model with guard ring pressures for sample COx-3.

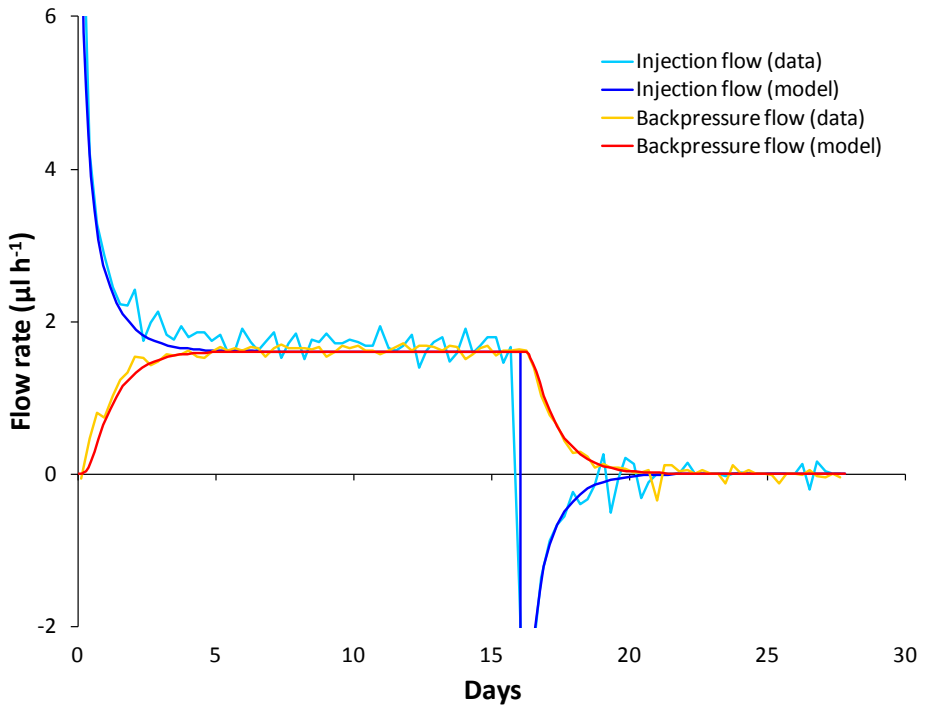

Figure 4-62 Comparison of an anisotropic permeability model with end surface leakage to flow data for sample COx-3.

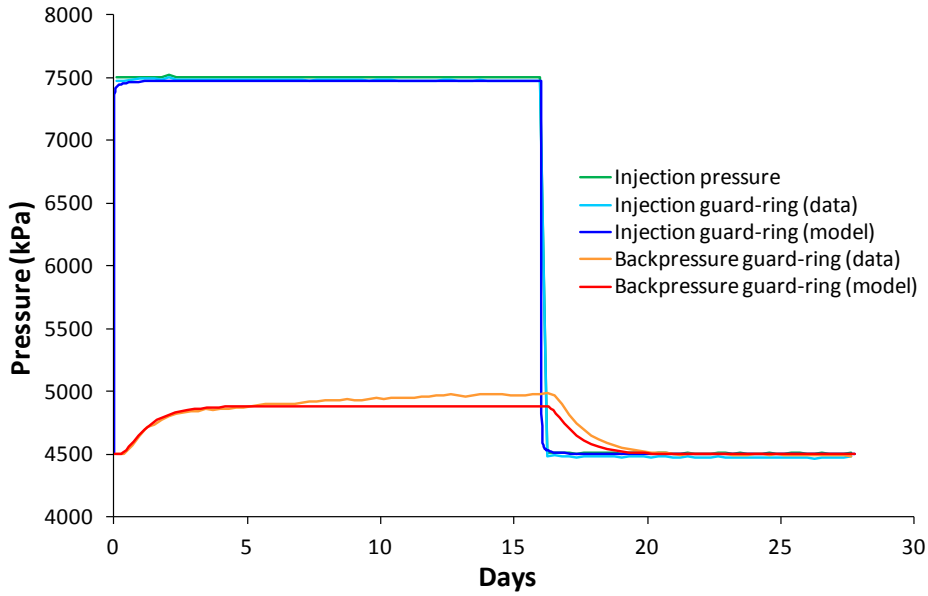

Figure 4-63 Comparison of an anisotropic permeability model with end surface leakage to guard ring pressures for sample COx-3.

One final model has been considered in which the sample has isotropic permeability. Figure 4-64 and Figure 4-65 show the results for a model in which the sample permeability on all three axies is set to 4.5×10^{-21} m^2, all other parameters being as for the previous model. It can be seen that the fit is essentially identical to that obtained before. This shows that, in the presence of these end surface leakage flows, the test is unable to make any determination of the sample anisotropy.

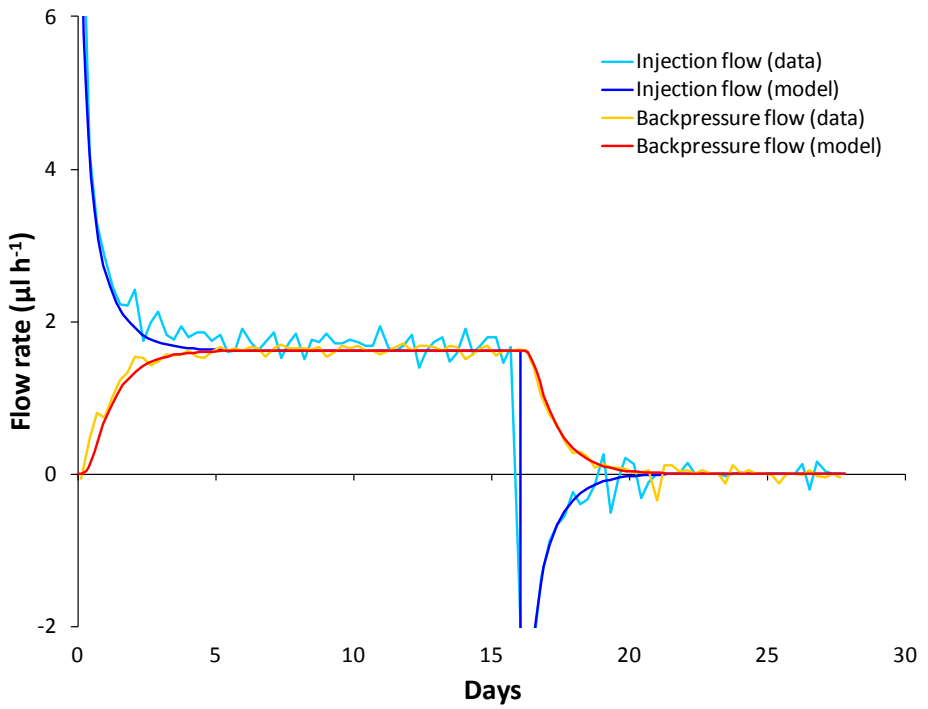

Figure 4-64 Comparison of an isotropic permeability model with end surface leakage to flow data for sample COx-3.

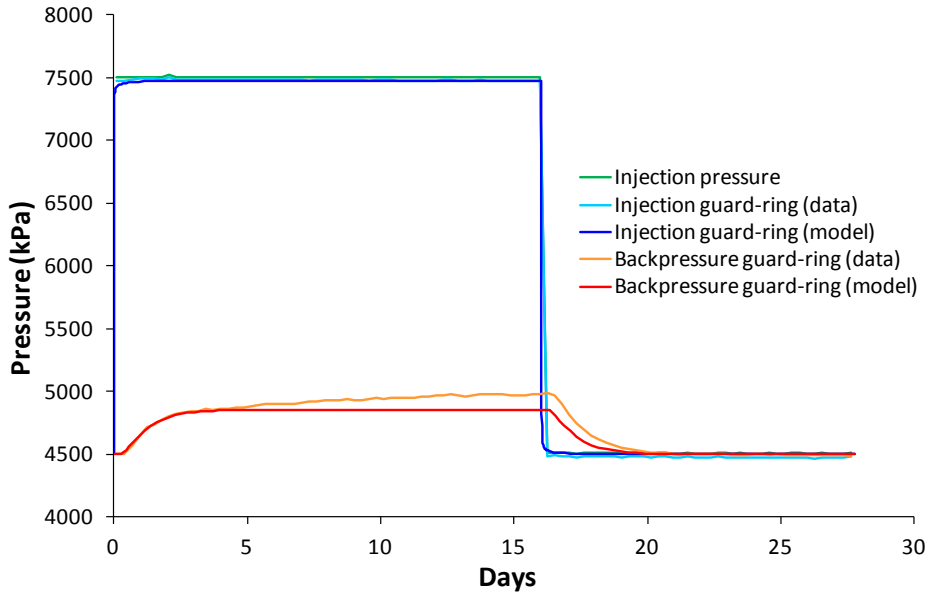

Figure 4-65 Comparison of an anisotropic permeability model with end surface leakage to guard ring pressures for sample COx-3.

4.3.3 Gas injection

The ethos behind gas test COx-3 was subtly different to that of previous experiments. Here the purpose of the test was to provide information on the stress state variables in an unsaturated medium (σ, p_g and p_w), in particular, the repeatability of the gas migration response to equal changes in gas and porewater pressure. With this in mind, helium gas was first equilibrated with the sample at the reference backpressure of 4.5 MPa, stage [6].

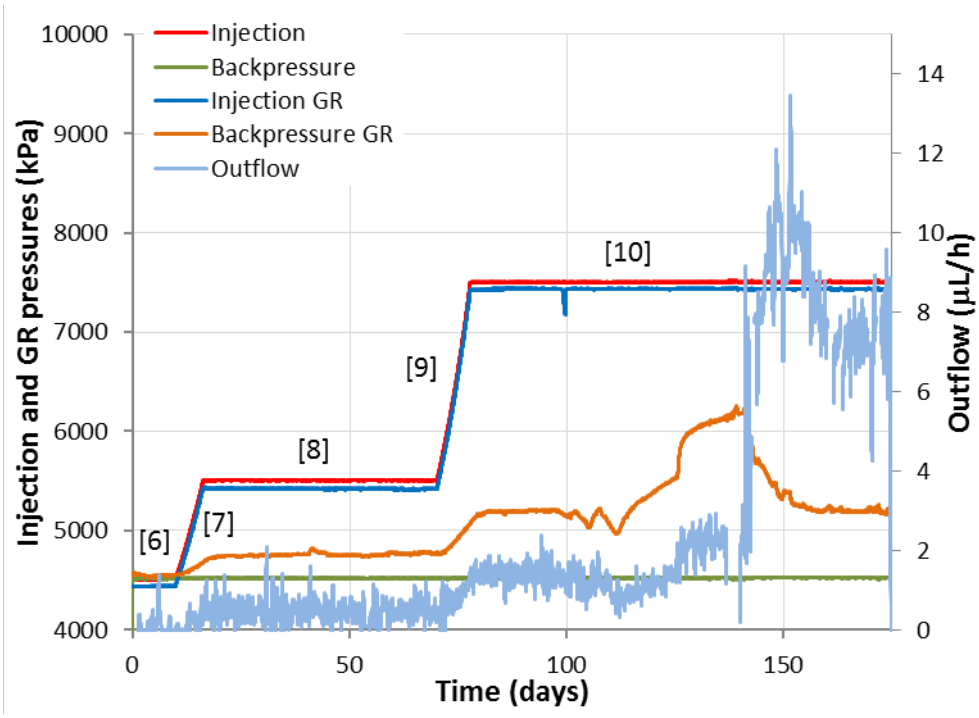

Figure 4-66 Evolution in pressure within sample COx-3 and outflow during test stages [6 to 10]. The small emergent flux is symptomatic of a low gas breakthrough pressure.

In a similar manner to previous gas tests, gas pressure was then increased in a stepwise manner from 4.5 MPa, stage [6], to 7.5 MPa, stage [10], during the first 175 days of gas testing. At each stage, the injection pressure was maintained constant while flux into and out of the specimen monitored with time. During the first constant pressure gas stage [8], a small emergent flux of fluid of around 0.5 $\mu l.h^{-1}$ was noted (Figure 4-66). By the end of the stage both guard ring pressures remained elevated and showed no sign of returning to the previous reference (backpressure) value. As the next gas pressure ramp began, stage [9], outflow and guard ring pressures began to increase. These continued to increase until the start of stage [10]. Thereafter, downstream guard ring and outflow reached an asymptote at values around 5.2 MPa and 1.4 $\mu l.h^{-1}$ respectively.

The system then remained in a quasi-steady state until day 98 when the backpressure guard ring began to fluctuate. This was accompanied by systematic changes in outflow as the pressure profile across the sample spontaneously moved into a transitory phase. Backpressure guard ring and outflow continued to evolve until major gas breakthrough occurred at day 140. This was accompanied by a sudden increase in outflow and decrease in backpressure guard ring. As permeability across the sample increased, outflow peaked before decrease to a quasi-steady state condition at around day 160. Major gas breakthrough was accompanied by a negative pressure transient in the backpressure guard ring trace, which was offset (i.e. predated the evolution in outflow) and asymptote at around 5.2 MPa, Figure 4-66. While this is very close to its the pre-major gas breakthrough value of 5.2 MPa, the offset in response strongly indicates the existence of multiple gas pathways across the sample.

To examine the sensitivity of gas flow to changes in porewater pressure, the pressure in the backpressure filter was increased to 6.5 MPa, stage [11]. This resulted in an inflow of fluid into the backpressure end of the sample, Figure 4-67. As inflow occurred, pressure in backpressure guard ring began to increase, reaching a peak value of 7.24 MPa at day 210 i.e. an excess pressure of 0.72 MPa. This value is very close to asymptote value for the guard ring during stage [10] i.e. 0.7 MPa, suggesting that conductive gas pathways connect the guard ring and backpressure filters at pressures in excess of 0.7 MPa.

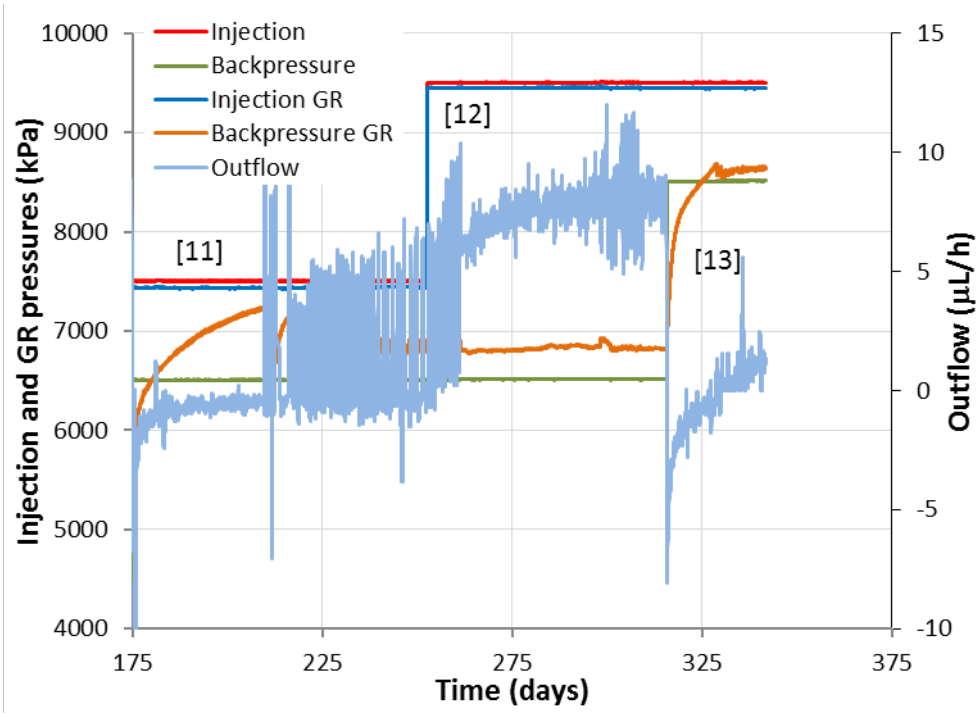

Figure 4-67 Evolution in pressure within sample COx-3 and outflow during test stages [11 to 13].

As the pathway(s) connect, pressure spontaneously decreases as permeability develops and outflow increases. The sudden increase in permeability results in a drop guard ring pressure,

which continues to fall until the pathway(s) can no longer be maintained and spontaneously close. This 'resealing' of the pathways is followed by a second pressurisation event, after which, the cycle begins anew. Figure 4-68 shows this behaviour in detail and suggests a cyclicity and repeatability to the response which lasts for the duration of stage [11]. Visual inspection of the data suggests there is a periodicity and repeatability to the response. This becomes evident in a cross plot between backpressure guard ring and outflow response from day 225 to 260, Figure 4-69, yielding a similar response to that of observed in Figure 4-56. As before the arrow denotes the direction of cycling with a small amount of noise in the plot introduced through the superposition of individual pressure cycles.

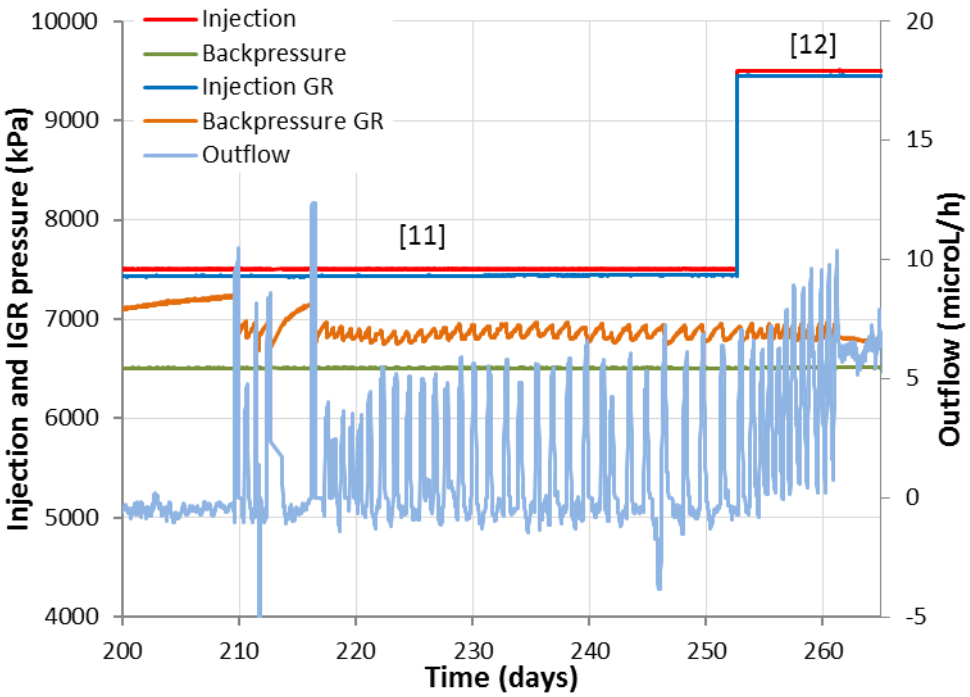

Figure 4-68 Cyclic behaviour between backpressure guard ring and outflow response indicating pathways formation and closure in response to changes in local gas pressure.

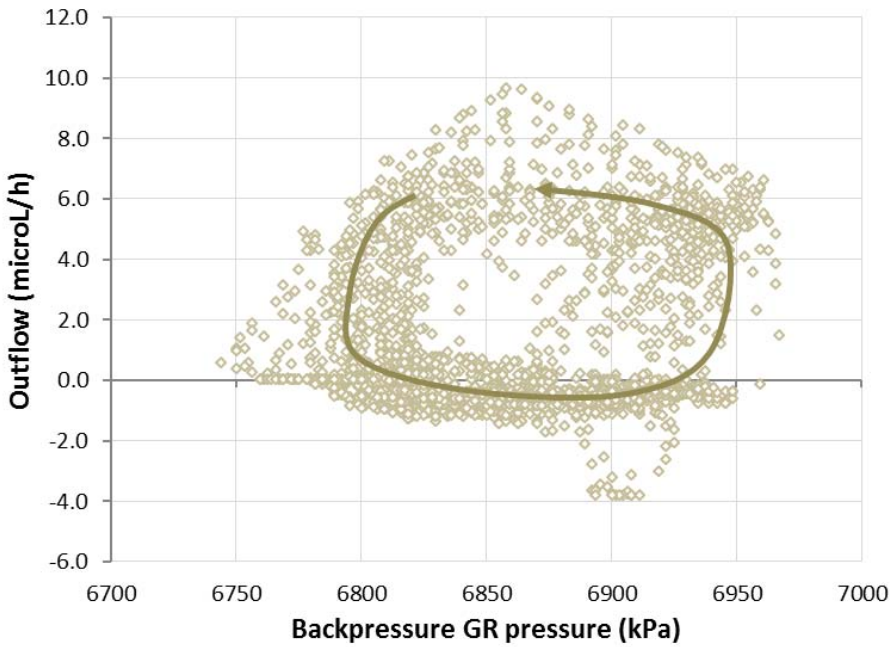

Figure 4-69 Cross plot of outflow versus backpressure guard ring from day 225 to 260. The underlying cyclic behaviour between flow and pressure becomes clear, with the arrow indicating the direction of the response.

In summary, as the gas pressure in the GR filter increased, it reached a critical value re-initiating gas outflow. However, unlike before, this outflow was highly episodic exhibiting clear burst-type behaviour. This would suggest that at very low gas pressure gradients COx does not always seal following a previous gas injection event. Interestingly this is in contrast to the triaxial test performed report by Cuss and Harrington (2012) who observed spontaneously self-sealed during advective gas flow. This difference in behaviour requires further work to better elucidate the main processes governing gas flow.

To investigate the symmetry of these processes and the validity of concepts such as axis translation, the previous gas pressure gradient was imposed across the sample on day 253, stage [12]. This was followed by a progressive increase in outflow. The burst-type behaviour noted in stage[11] continued at an increased periodicity until around day 261, then spontaneously stopped, probably when there is a sufficient number/density of pathways through the sample. Outflow is then much 'smoother' than before and the oscillation in pressure within the backpressure guard ring stops. By day 280, outflow had reached a well-defined asymptote of around 7.7 $\mu l.h^{-1}$, very close to the previous value of 7.3 $\mu l.h^{-1}$ from stage [10]. This suggests that the permeability of the sample remains approximately constant for the same gas pressure gradient as the test conditions repeatedly cycle between drainage and imbibition responses. However, the validity of this observation to COx in general requires more work to understand the differences in behaviour between this and COx-1 and COx-2.

In an attempt to better understand the relationship between gas and porewater pressure, pressure in the backpressure filter was increased to 8.5 MPa, stage [13], to apply the same excess gas pressure (and therefore driving gradient) across the sample as that imposed in stage [11]. As before, the change in boundary condition was followed by an inflow of fluid to the sample and a slow increase in backpressure guard ring Figure 4-70. As pressure in the backpressure guard ring increased above that in the reference backpressure filter, inflow reversed and a net outflow of fluid was observed. This initial change in flow direction occurred at a guard ring pressure of 8.68 MPa, an excess pressure of only 0.18 MPa. This is significantly lower than before and may reflect a change in system behaviour. As in stage [11], the guard ring pressure thereafter exhibits an episodic response, though this time with a much higher frequency. While there is some noise in the guard ring response, pressures appear to stabalise around 8.64 MPa from day 344. A slight upward trend in backpressure guard-ring is observed during the remainder of the stage which may relate to the evolution in conductive pathways. This test remains ongoing.

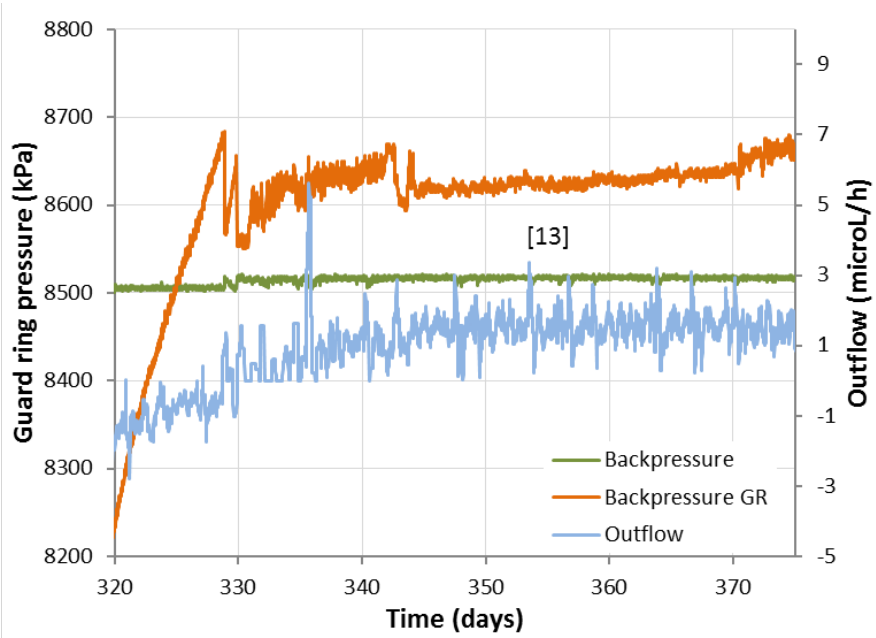

Figure 4-70 Evolution in guard ring pressure and outflow during stage [13], test COx-3.

5 Modelling of the gas data

A numerical model was set up to try to reproduce some of these features of the data and to help understand the properties of the sample. The multi-phase flow code TOUGH2 was used with the EOS3 equation of state module (Pruess et al, 1999). An axisymmetric mesh was used with some refinement towards the sample ends and including the various filters as separate elements of the model, as shown in Figure 5-1.

The clay sample 1 was assumed to have a radial permeability of $5\text{x}10^{-20}$ m^2 and an axial permeability of $2\text{x}10^{-21}$ m^2 as determined by the hydraulic test, while sample 2 was assumed to have a radial permeability of $8.8\text{x}10^{-21}$ m^2 and an axial permeability of $1.6\text{x}10^{-21}$ m^2. The porosity was set at 14.5% for both samples and their solid phase compressibilities at $4.8\text{x}10^{-10}$ Pa^{-1}. The filters were given an isotropic permeability of 10^{-16} m^2 and a porosity of 0.5.

In attempting to reproduce the test results the parameters of the relative permeability function for the clay were used as potential fitting parameters. The functions used by TOUGH2 in this study for relative permeability are slightly modified forms of the model due to van Genuchten (1980). The relative permeability for the liquid phase is given by

$$k_{rl} = \sqrt{S^*}\left\{1-\left(1-\left[S^*\right]^{1/\lambda}\right)^{\lambda}\right\}^2$$

and the relative permeability of the gas phase is given by

$$k_{rg} = 1 - k_{rl} \qquad \text{if } S_l = 0$$

$$k_{rg} = \left[\left(1-\hat{S}\right)^2\left(1-\hat{S}^2\right)\right]^n \qquad \text{if } S_{gr} > 0$$

where

$$S^* = \frac{\left(S_l - S_{lr}\right)}{\left(S_{ls} - S_{lr}\right)}$$

and

$$\hat{S} = \frac{\left(S_l - S_{lr}\right)}{\left(1 - S_{lr} - S_{gr}\right)}$$

The parameters for this model are λ a fitting parameter, S_{lr} the residual liquid saturation, S_{ls} the maximum liquid saturation, S_{gr} the residual gas saturation, and n an additional fitting parameter. In the current work, λ was set to 0.6, S_{ls} was set to 1.0, and S_{gr} was set to 0.001. Variations in S_{lr} and n were used to change the model response to compare with different aspects of the test data from sample COx-1. Figure 5-2 shows some experimental data from ANDRA (2009) together with the relative permeability curves used in the three models of sample 1 presented below. The curve labelled Model 5.1 was used for modelling sample COx-2.

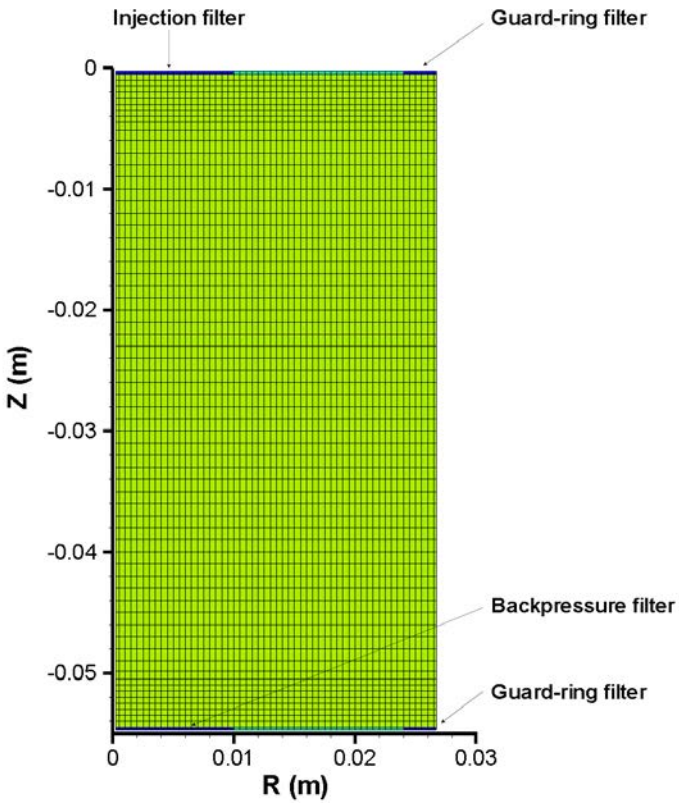

Figure 5-1 The main elements and calculational mesh used for the TOUGH2 models of the gas injection test. Cylindrical symmetry about the z-axis is assumed.

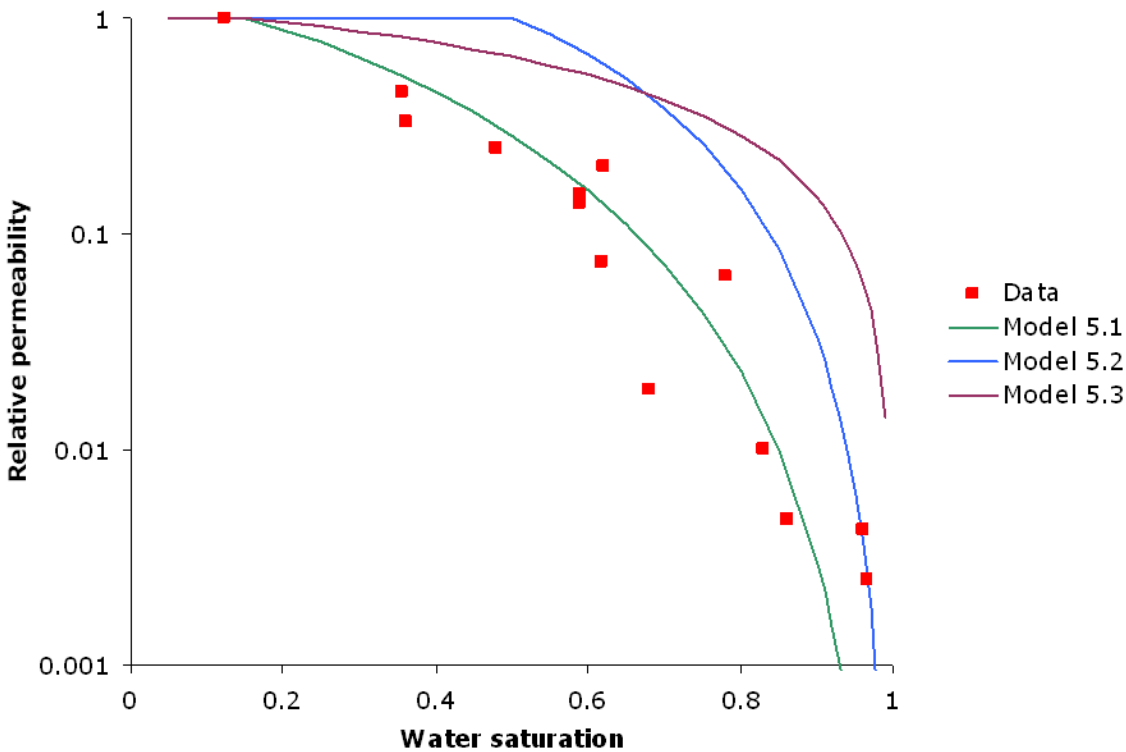

Figure 5-2 Relative permeability data compared to the models presented in sections 5.1, 5.2, and 5.3 below.

TOUGH2 also requires the definition of the capillary pressure functions and for this work the functions due to van Genuchten (1980) were also used. Thus the capillary pressure is given by

$$P_{cap} = -P_0\left(\left[S^*\right]^{-1/\lambda} - 1\right)^{1-\lambda}$$

subject to the restriction $-P_{max} \leq P_{cap} \leq 0$.

Here,

$$S^* = \frac{(S_l - S_{lr})}{(S_{ls} - S_{lr})}$$

The new parameter for this model is P_0, which is effectively the capillary entry pressure for this function. In this work the value of P_0 was set to 2 MPa for the clay sample 1 and to 20 kPa for the filters. P_0 was used as an adjustable parameter when modelling sample 2.

5.1 AN INITIAL MODEL FOR SAMPLE 1

A first model for sample 1 was obtained by setting S_{lr} to 0.15 and n to 1.0. As shown in Figure 5-2, this gives a relative permeability function that reproduces the experimental data of ANDRA (2009) quite well. The filter pressures obtained from the model are compared to the data in Figure 5-3 and the flow rate at the backpressure filter predicted by the model is compared to the data in Figure 5-4. It can be seen that this model gives a good fit to the injection guard-ring data after 170 days but there are significant differences before that time except for the initial pressure decline over the first 9 days. It may be noted that there is a step in the model pressure accompanying the arrival of gas at the injection guard-ring that is comparable in magnitude with that seen in the data, but it arrives at about day 32 instead of day 16. Modelled gas phase arrival at the backpressure filter and guard ring occurs at about 350 days whereas the data indicates its arrival at about 170 days, and the modelled inflow and outflow rates after arrival are much less than the measured values. The modelled water outflow rates before 170 days are comparable to the flow rates seen in the data at about 0.5 $\mu l.hr^{-1}$.

5.2 A MODEL FOR SAMPLE 1 FITTED TO GAS BREAKTHROUGH AT BACKPRESSURE FILTER.

One of the key features of the test that was not reproduced by the initial model was the time of first arrival of the injected gas at the backpressure filter. Adjustments to the model parameters were made to try to improve this. Figure 5-5 and Figure 5-6 show the output from a model in which S_{lr} has been increased to 0.5 and n reduced to 0.8. As shown in Figure 5-2, this gives increased gas phase relative permeabilities which allows the gas to break through at the backpressure filter earlier than in the initial model. It can be seen that the model predictions for pressures at the injection filter and injection guard-ring filter are little different from those of the earlier model. The modelled pressure at the backpressure guard ring shows a distinctive ‘double step’ in the middle of the 7.5 MPa injection pressure stage at the time of gas arrival which is similar to the shape of the test data between 170 and 200 days. However, the test data then show a steep drop back to pressures close to that of the backpressure filter, while the model predicts the pressure to continue to rise with further steps occurring in close association with those in the injection pressure. The flow rate data show that although the modelled gas breakthrough occurs at the same time as that seen in the test data, the modelled injection and outflow rates grow much more slowly than are observed.

5.3 A MODEL FOR SAMPLE 1 FITTED TO GAS OUTFLOW RATES.

As seen in the models above, predicted gas outflow rates are much lower than are seen in the test data. Further parameter changes were attempted to determine what would be required to obtain flow rates comparable to those observed. Figure 5-7 and Figure 5-8 show the results obtained

from a model with S_{lr} set to 0.15, as for the initial model, and n reduced to 0.33. It can be seen that this reduction in n, which increases the relative permeability to gas for a given gas saturation (see Figure 5-2), allows the gas to penetrate the sample more quickly and flow at a greater rate after breakthrough. Indeed, a good fit to the flow rates has been obtained between about 220 and 600 days apart from an anomalous event at about 460 days. However, this fit is obtained by allowing a gas breakthrough after only 50 days and it would appear that flow rates after the injection pressure step to 12 MPa at 600 days are again greater than predicted by the model. This model also has a poor representation of the very early pressure response at the injection guard-ring filter where the rapid gas movement has eliminated the early pressure decline seen in the data for the first 12 days.

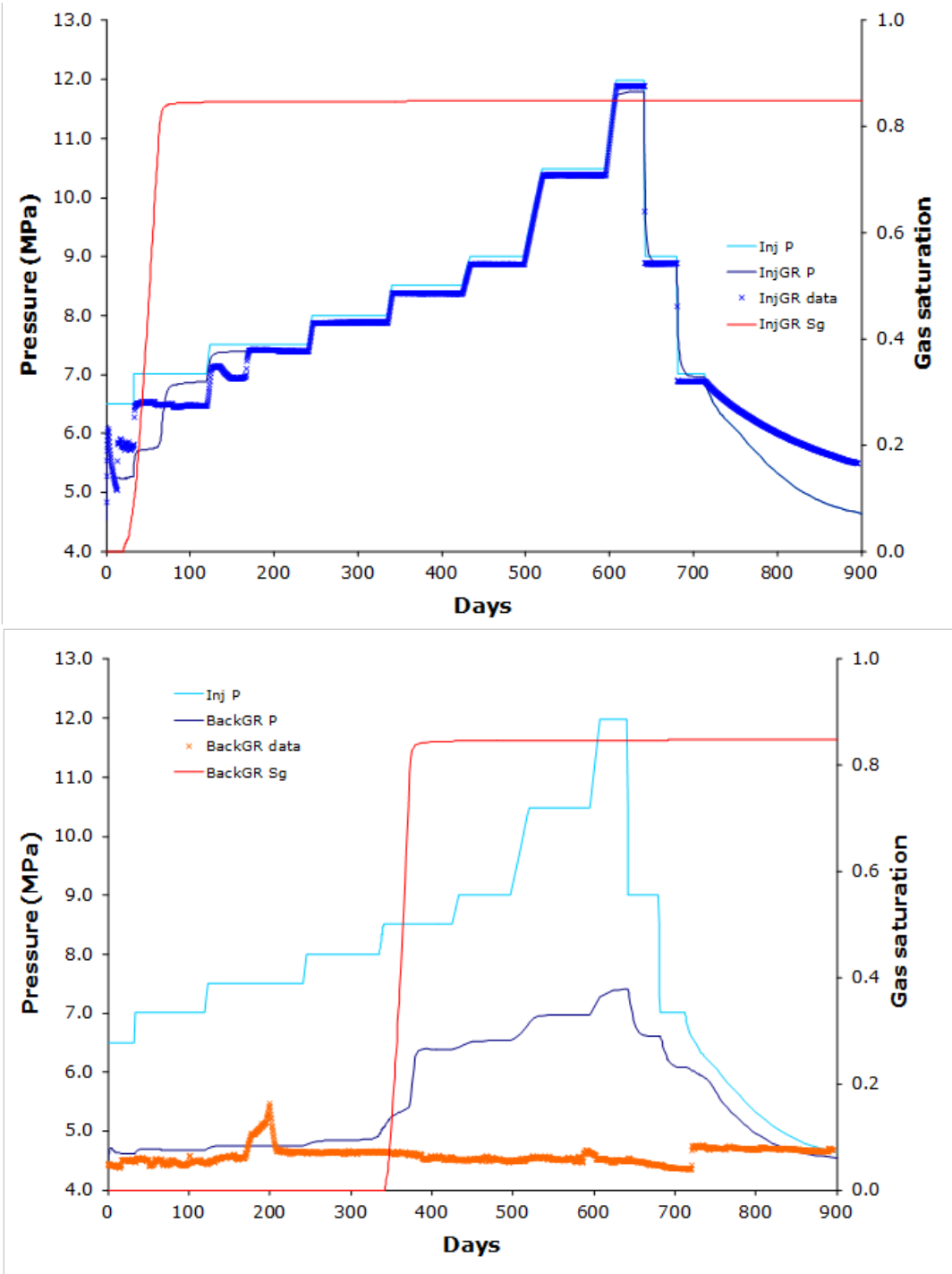

Figure 5-3 Initial model pressures compared to guard-ring data from sample 1.

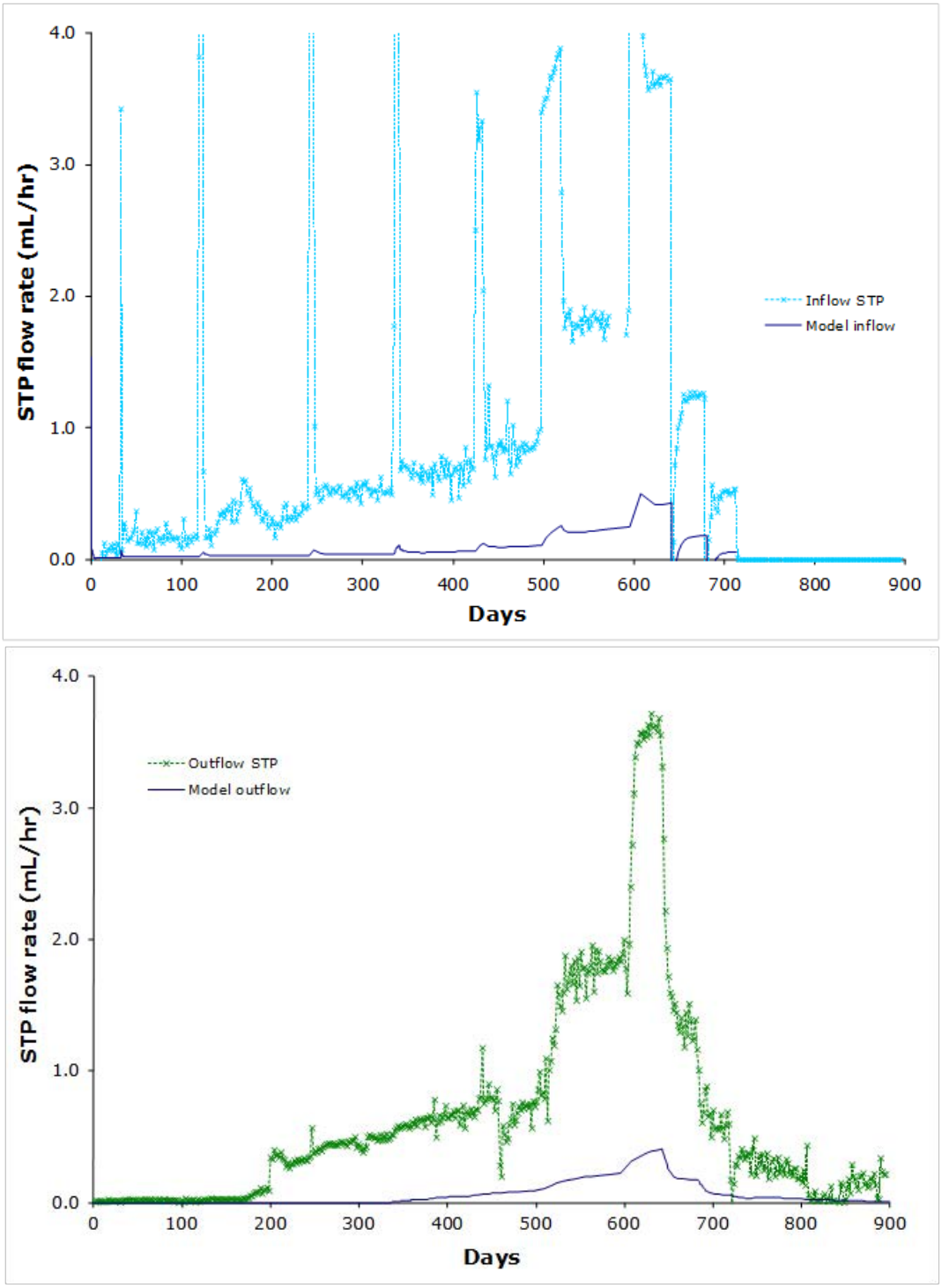

Figure 5-4 Initial model flow rates compared to the injection and backpressure filter data from sample 1.

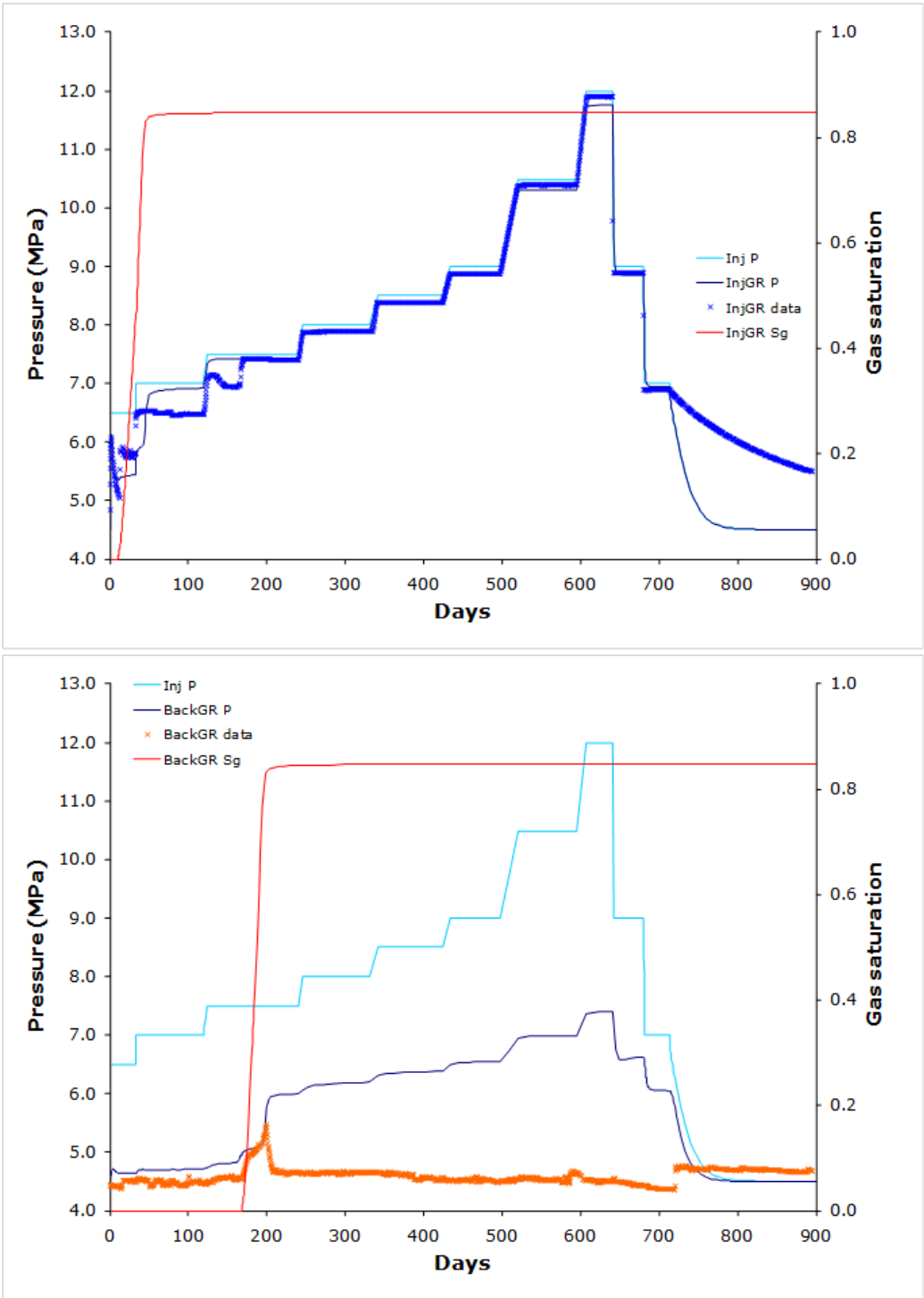

Figure 5-5 Pressures from a model fitted to the gas breakthrough time at the backpressure filter compared to test data from sample 1.

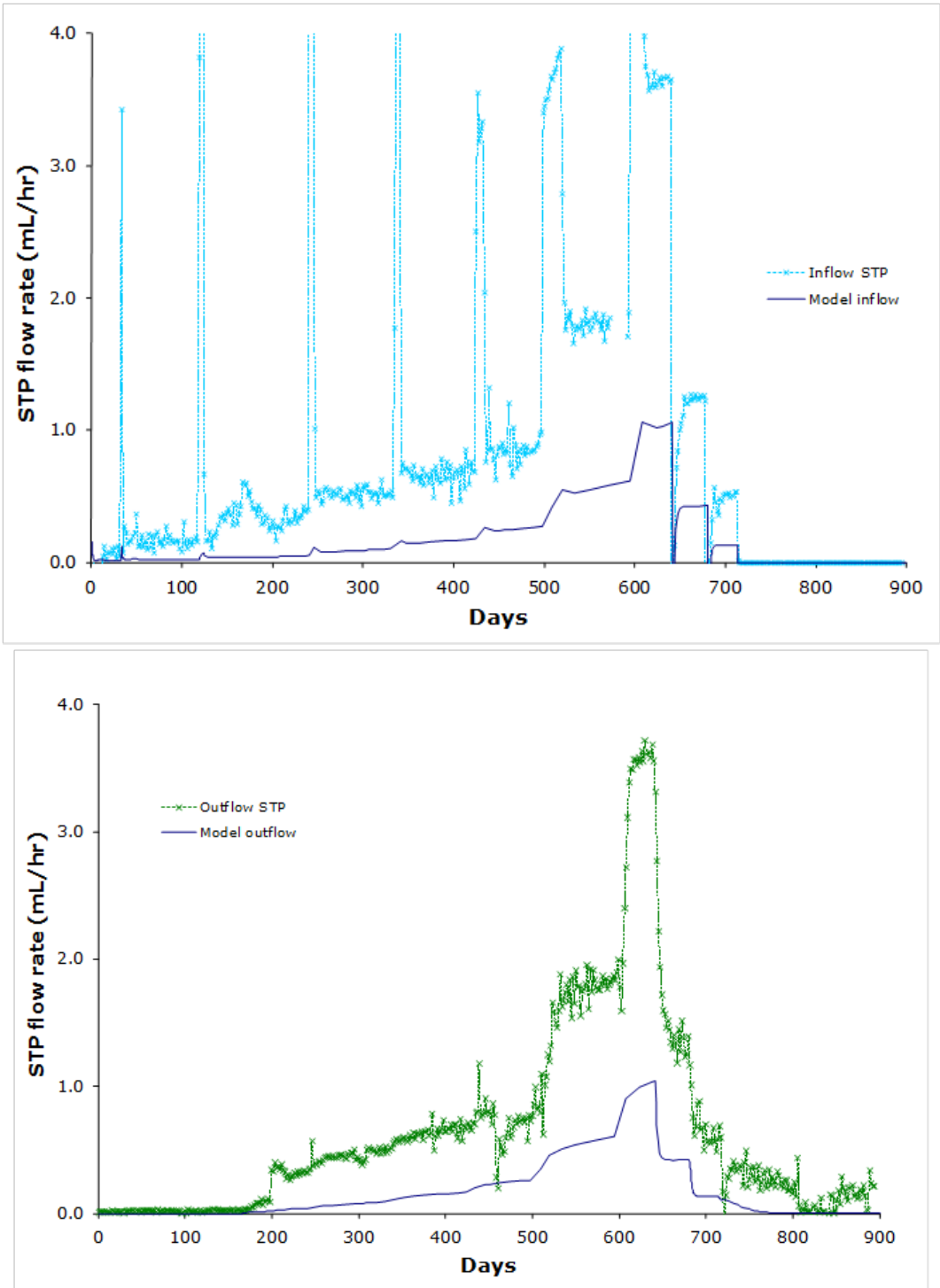

Figure 5-6 Flow rates at the injection and backpressure filters from a model fitted to the gas breakthrough time compared to test data from sample 1.

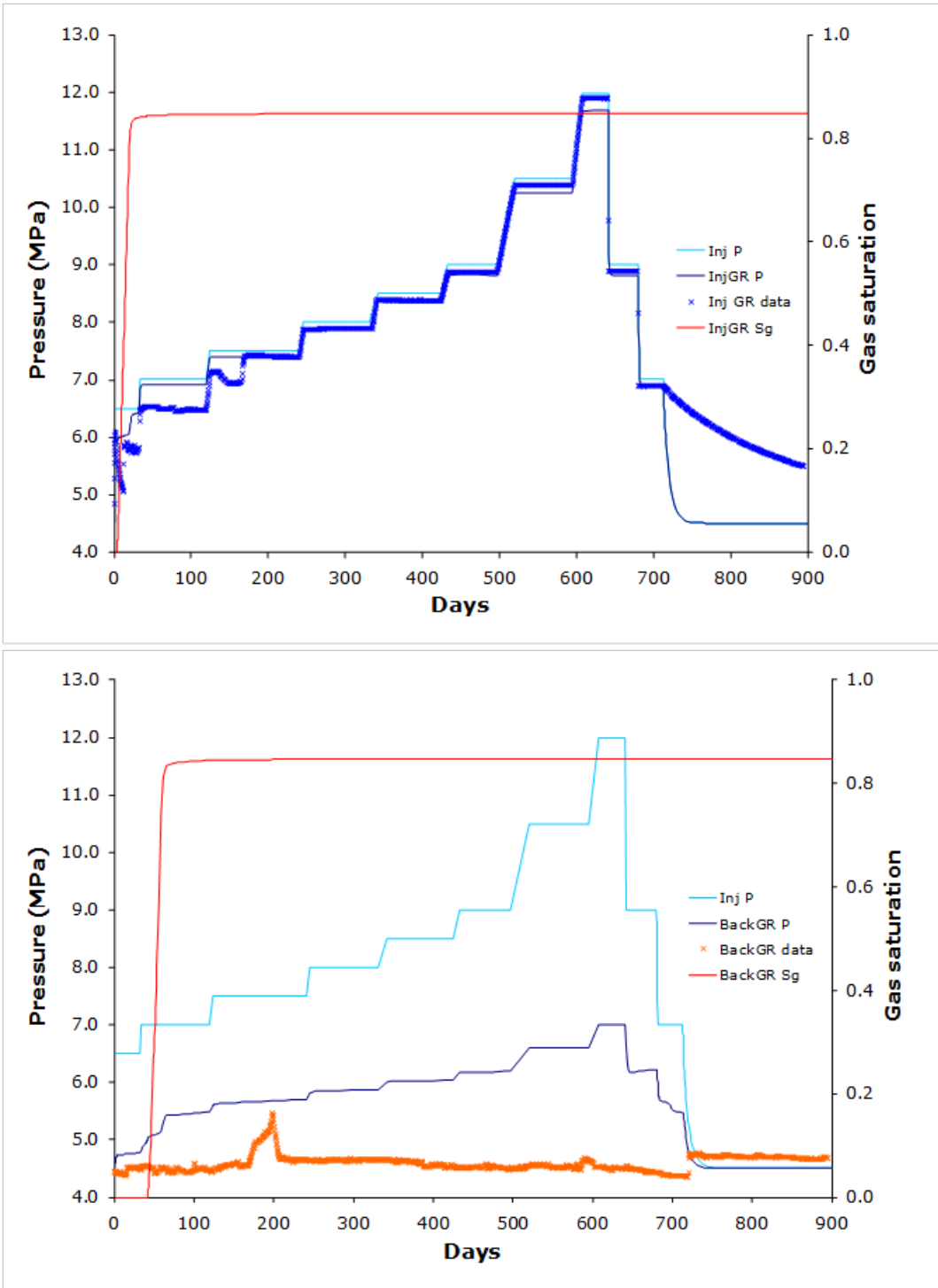

Figure 5-7 Pressures from a model fitted to the gas flow rates at the backpressure filter compared to test data from sample 1.

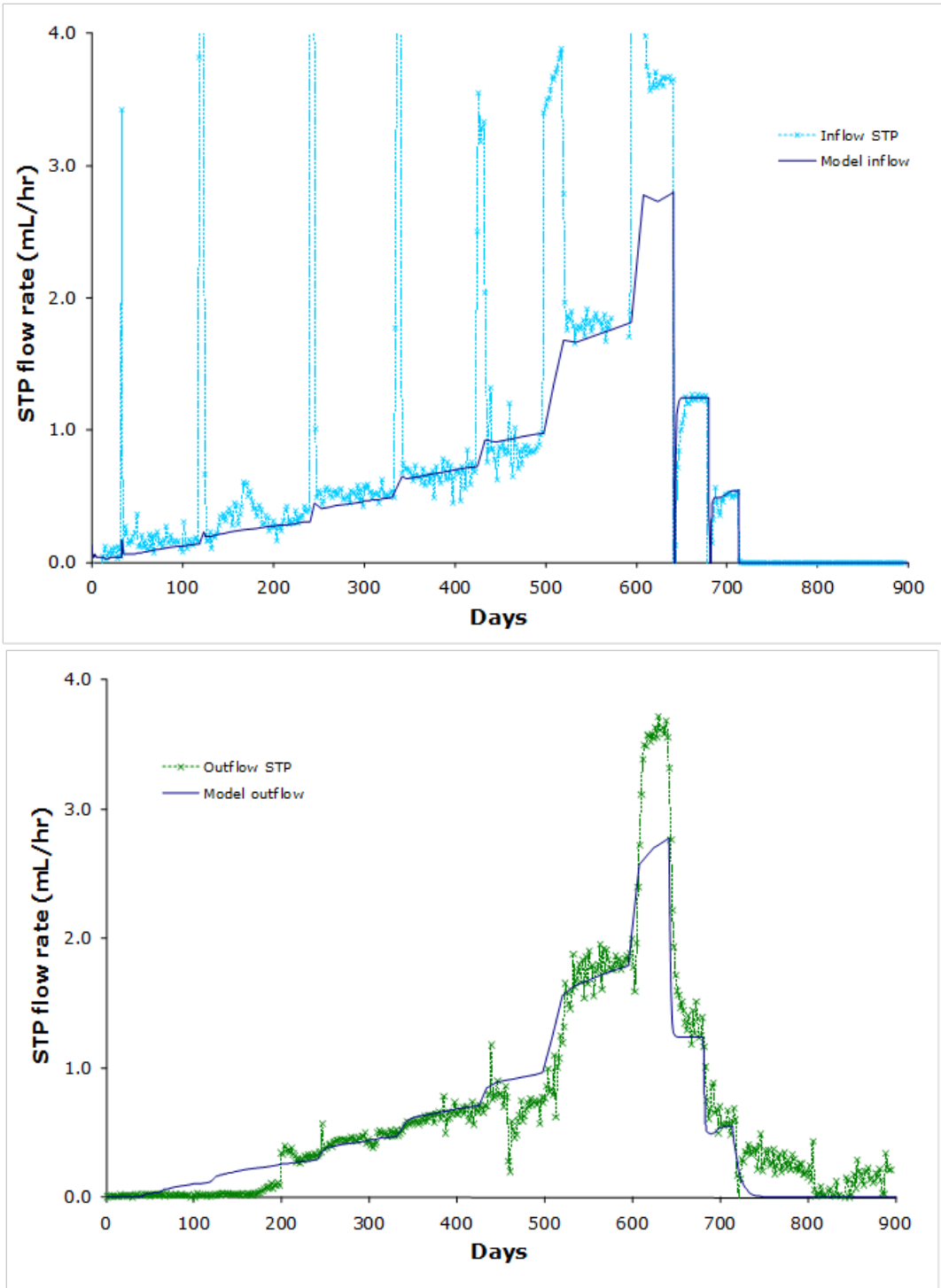

Figure 5-8 Flow rates at the backpressure filter from a model fitted to the gas flow rates compared to test data from sample 1.

5.4 A MODEL FOR SAMPLE 2 FITTED TO BACKPRESSURE GUARD RING ARRIVAL TIME

For the purposes of this modelling the multiple steps to the ramp up of the injection pressure were approximated by a single continuous rate of increase of the pressure between the initial value of 7 MPa and the final value of 11.25 MPa, as shown in Figure 5-9. It was found that setting the parameter P_0 to 5 MPa gave a good agreement between the model and the observed time of pressure change at the backpressure guard ring filter. However, as shown in Figure 5-9, this model has a very poor representation of the pressure at the injection guard ring filter.

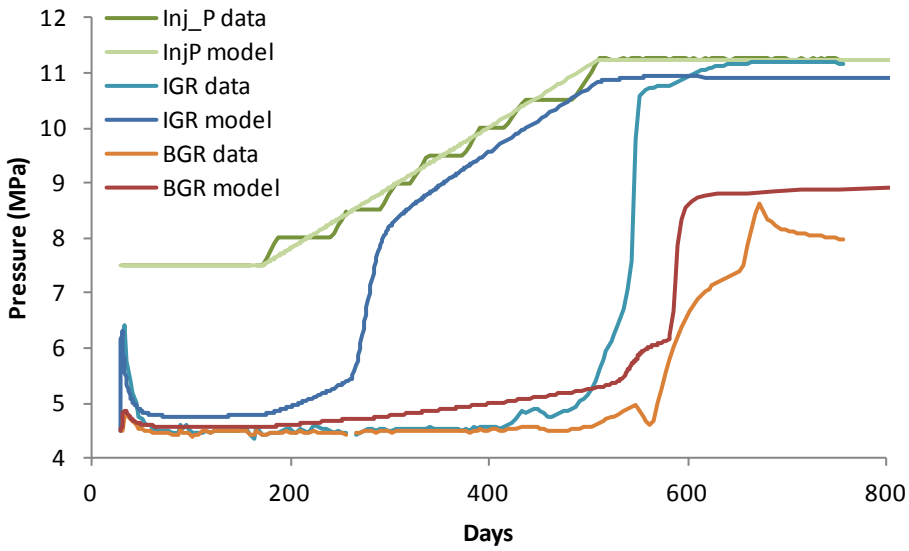

Figure 5-9 Comparison of model pressures to the data for sample 2 from the injection, injection guard ring, and backpressure guard ring filters. P_0 = 5 MPa for this model.

As shown in Figure 5-10, this model also provides quite a good representation of the gas flow rates observed at the outflow (backpressure) filter.

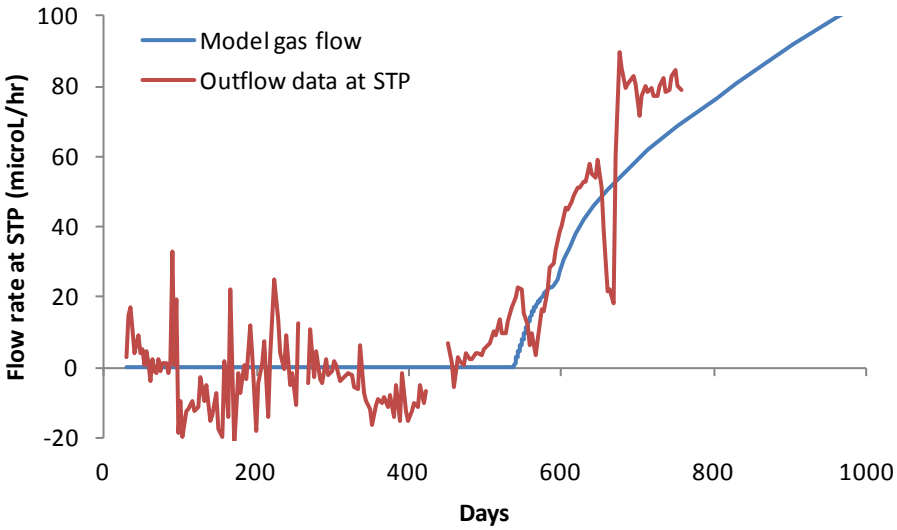

Figure 5-10 Comparison of the data for sample 2 for gas outflow rate, converted to STP, with the values calculated from the model with P_0 = 5 MPa.

The model discussed above does not include diffusion of the gas within the aqueous phase. A variation was run in which the diffusion coefficient, D, was set to 2.0×10^{-10} m^2 s^{-1}. The pressures calculated from this model are shown in Figure 5-11 and the gas outflow rates in Figure 5-12. It can be seen that some smoothing of the model curves has occurred, but otherwise the main features are much the same.

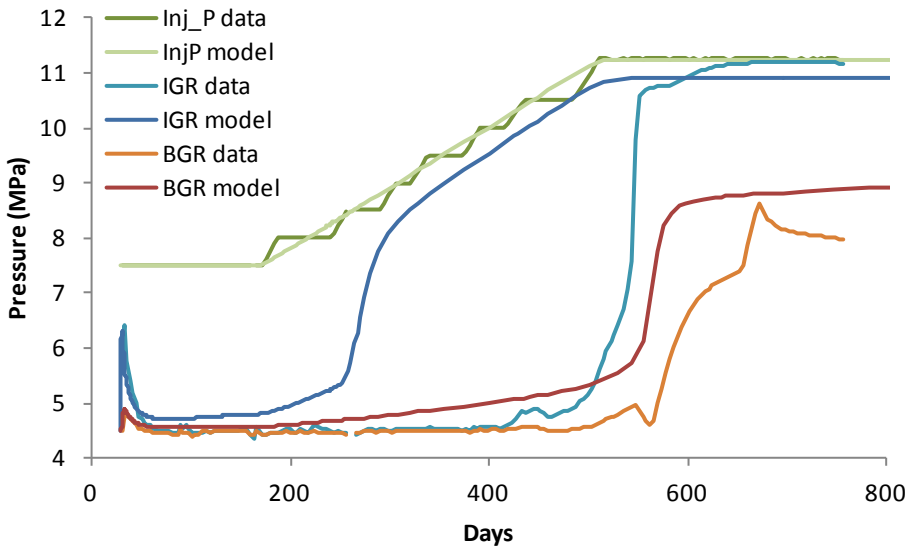

Figure 5-11 Comparison of model pressures to the data for sample 2 from the injection, injection guard ring, and backpressure guard ring filters. P_0 = 5 MPa and D = 2.0x10^{-10} m^2 s^{-1} for this model.

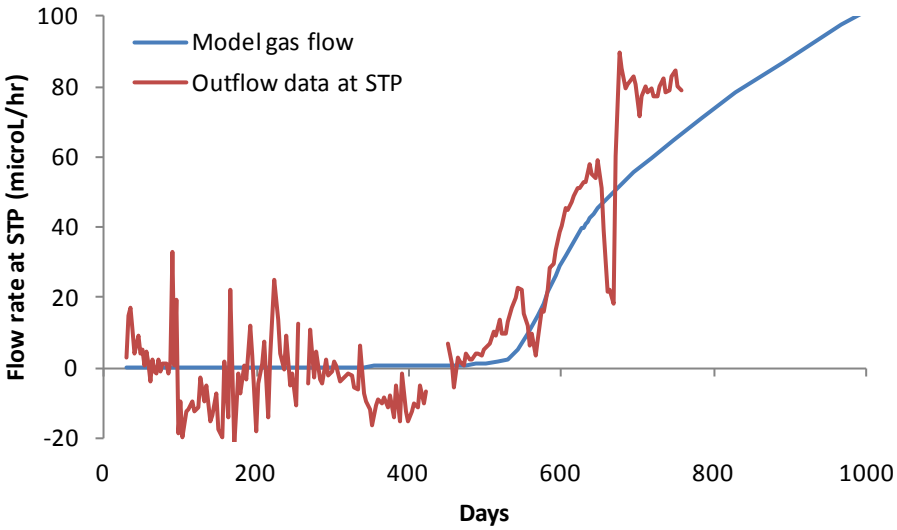

Figure 5-12 Comparison of the data from sample 2 for gas outflow rate, converted to STP, with the values calculated from the model with P_0 = 5 MPa and D = 2.0x10^{-10} m^2 s^{-1}.

5.5 A MODEL FOR SAMPLE COX-2 FITTED TO INJECTION GUARD RING ARRIVAL TIME

Further runs of the model were made to try to fit to the pressure data from the injection guard ring filter. Figure 5-13 shows the results obtained with a value of P_0 = 11 MPa. The time of arrival of the pressure step at the injection guard ring is reproduced well but the model shows no response at the backpressure guard ring within the first 800 days. Figure 5-14 shows the continued model behaviour with the backpressure guard ring responding at about 1300 days.

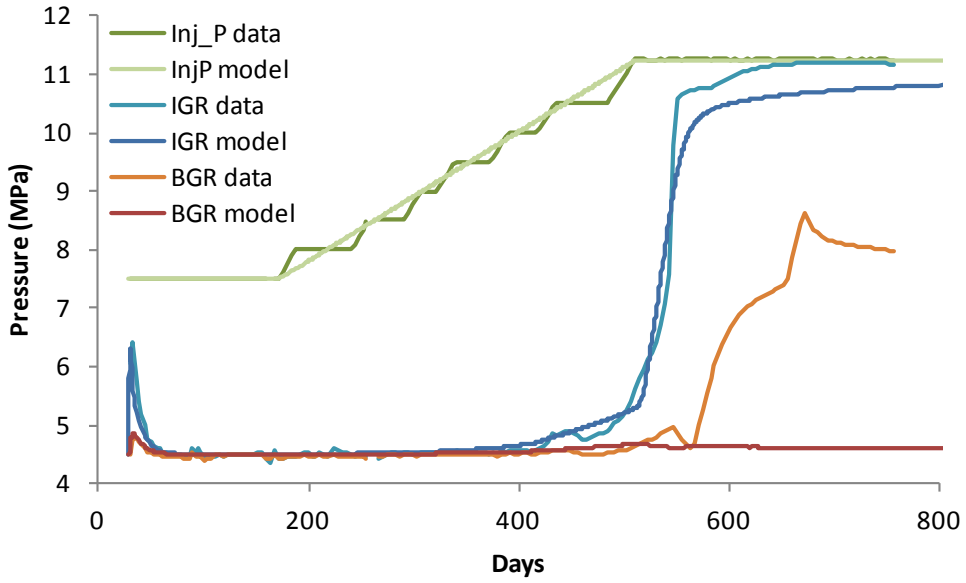

Figure 5-13 Comparison of model pressures to the data for sample 2 from the injection, injection guard ring, and backpressure guard ring filters. P_0 = 11 MPa for this model.

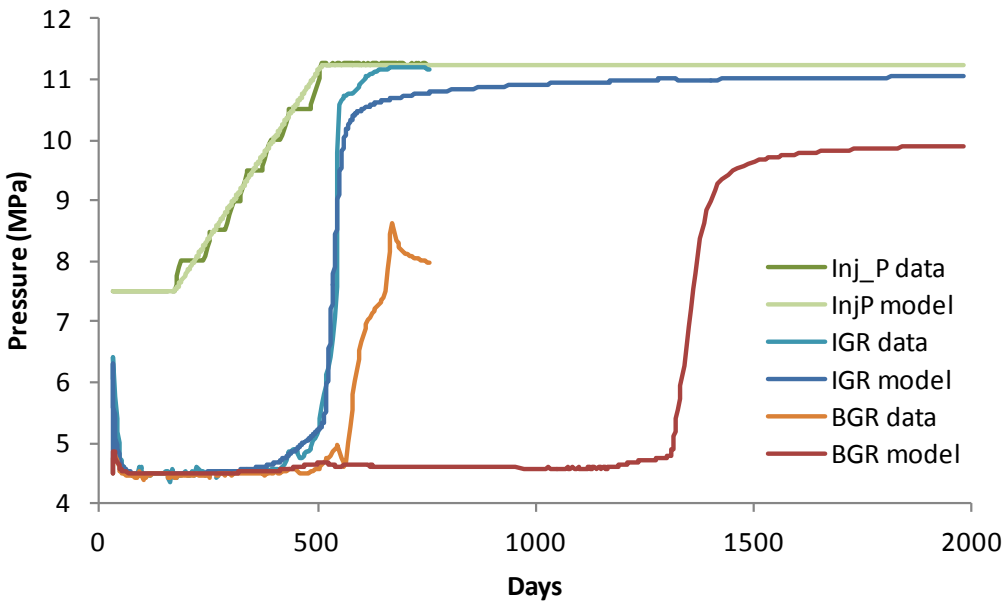

Figure 5-14 Comparison of model pressures to the data for sample 2 from the injection, injection guard ring, and backpressure guard ring filters. P_0 = 11 MPa for this model.

Similarly, the gas outflow from this model is greatly delayed, as shown in Figure 5-15. The first signs of flow from the backpressure filter occur at about 1200 days and thereafter the flow rate is approximately one tenth of the magnitude seen in the data.

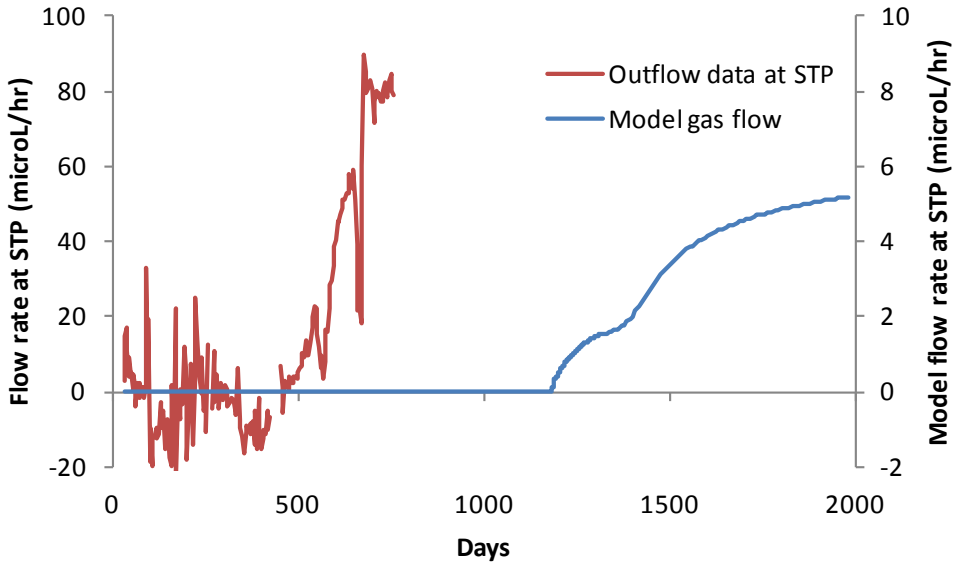

Figure 5-15 Comparison of the data from sample COx-2 for gas outflow rate, converted to STP, with the values calculated from the model with P_0 = 11 MPa.

The effect of diffusion on this model is slightly more significant than before and it was found that using a diffusion coefficient of $2x10^{-10}$ m^2 s^{-1} as before it was necessary to increase the value of P_0 to 12.5 MPa to get the good fit to the timing of the injection guard ring pressure response, as shown in Figure 5-16. Figure 5-17 shows that the response at the backpressure guard ring first occurs much earlier than before at about 800 days, but still much later than is seen in the data and the pressure build up is much more gradual.

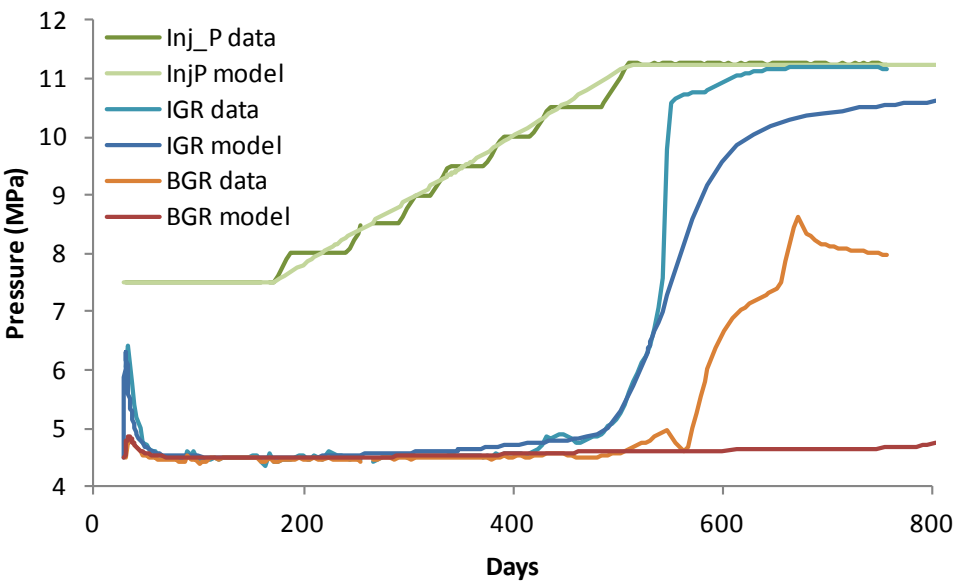

Figure 5-16 Comparison of model pressures to the data for sample 2 from the injection, injection guard ring, and backpressure guard ring filters. P_0 = 12.5 MPa and D = $2.0x10^{-10}$ m^2 s^{-1} for this model.

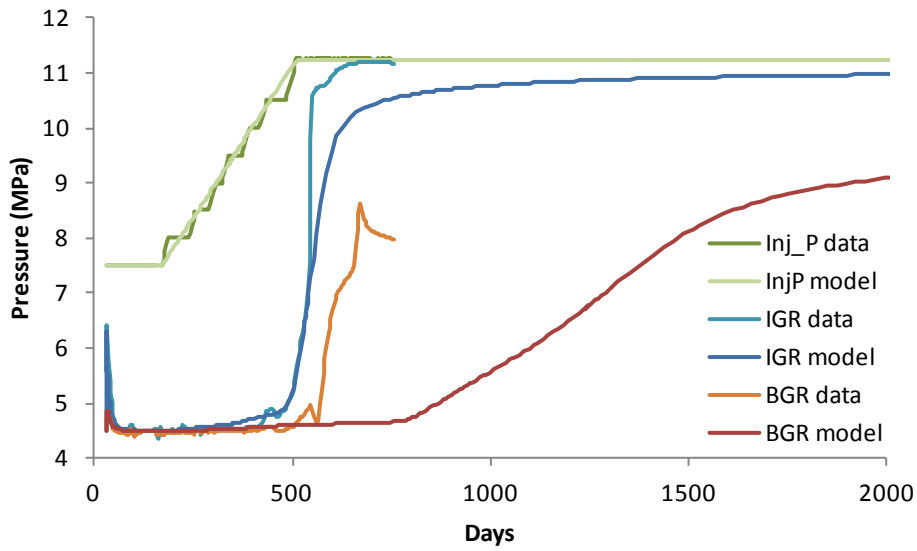

Figure 5-17 Comparison of model pressures to the data for sample COx-2 from the injection, injection guard ring, and backpressure guard ring filters. P_0 = 12.5 MPa and D = 2.0x10^{-10} m^2 s^{-1} for this model.

Figure 5-18 shows that outflow from the backpressure filter also occurs much earlier than before, at about 350 days which is comparable to that seen in the data. However, the magnitude of the flow is still much smaller than in the experimental data.

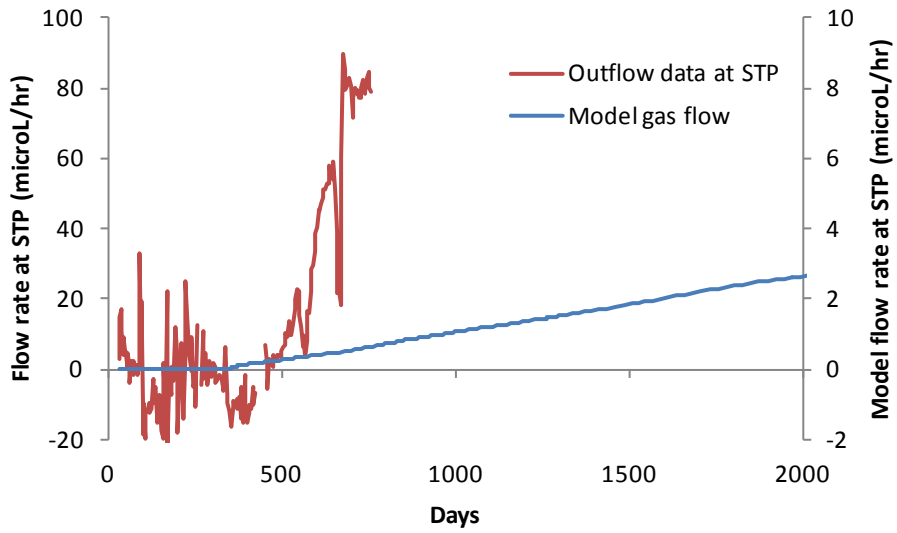

Figure 5-18 Comparison of the data from sample 2 for gas outflow rate, converted to STP, with the values calculated from the model with P_0 = 12.5 MPa and D = 2.0x10^{-10} m^2 s^{-1}.

6 Implications for process understanding

Clearly, none of the models presented in Section 5 provide a good representation of the whole data set and indeed there are some features in the data that none of the models are able to reproduce such as the pressure reduction on the injection guard-ring filter in the middle of the 7.5 MPa stage and the abrupt pressure loss on the backpressure guard-ring at 200 days. A possible explanation for the latter event could be the development of a discrete conductive flow path between the guard-ring and backpressure filters. Alternatively, the substantial increase in

the gas flow rate at the backpressure filter at the same time might indicate the development of a discrete flow path between injection and backpressure filters, by-passing the backpressure guard-ring.

Despite these indicators of discrete path flow it is notable that the growth of gas flow rates between 220 and 600 days of the test on sample Cox-1 seems to follow the form of a porous medium path, with the flow rate growing as the gas saturation increases which in turn allows the gas phase relative permeability to rise. The change in gas saturation through the sample during this period is shown in Figure 6-1 and axial profiles of gas saturation and gas phase relative permeability are given in Figure 6-2. It can be seen that in this model, which provides a good fit to the gas flow rates during this period, the gas saturations and relative permeabilities approximately double between these two dates. It should be noted that the gas saturations continue to increase during the periods when the injection pressure is held constant, and this is reflected in the gradually rising gas flow rates seen during in a number of the test stages. This has implications for any attempt to re-interpret the test data in terms of discrete path flow since it would be necessary to include a mechanism for the paths to continue to expand over the periods of constant injection pressure in such a way that the gas flow rate rises in the same way as for the porous medium model.

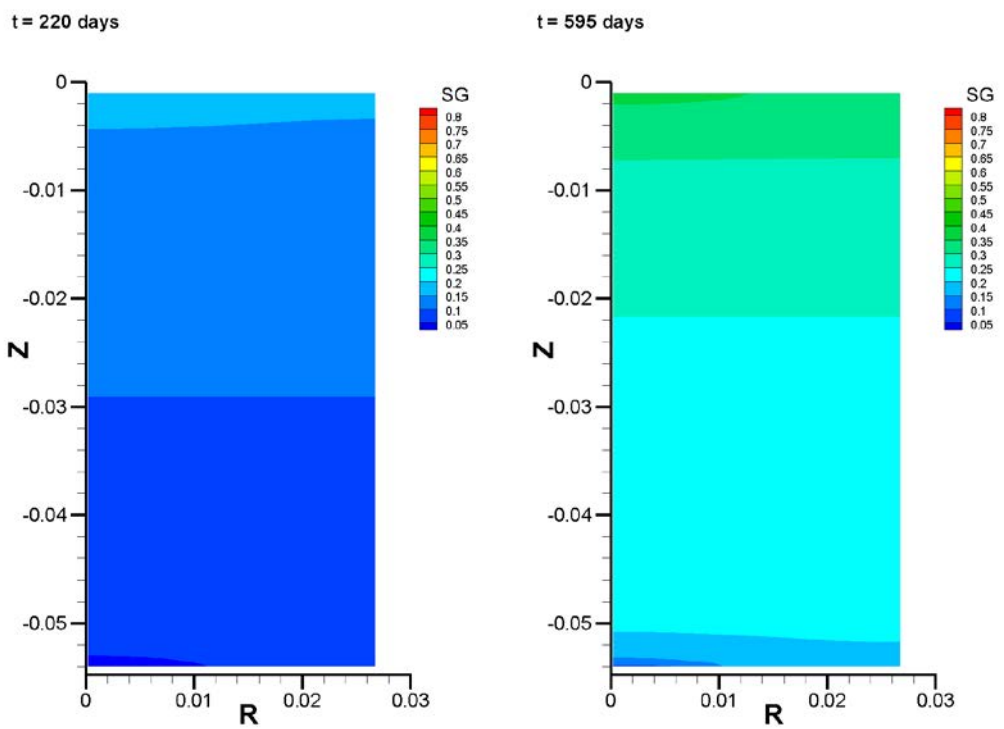

Figure 6-1 Contour plots of gas saturation (SG) at two times from the model of Section 5.3.

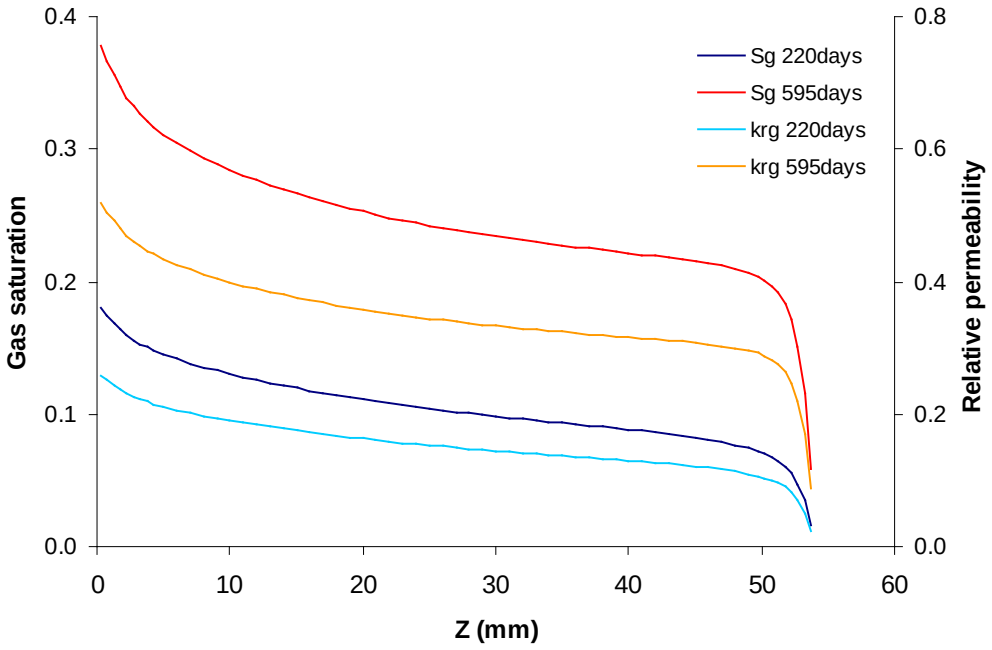

Figure 6-2 Axial profiles of gas saturation (S_g) and relative permeability of the gas phase (k_{rg}) at two times from the model of Section 5.3.

However, the existence of time-dependent discrete pathway flow coupling gas pressure gradient, porewater pressure and stress has been well documented in pure clay systems (Horseman and Harrington, 1997; Horseman et al. 1996, 1999; Harrington and Horseman, 2003; Cuss et al., 2010) and natural plastic clays (Horseman and Harrington, 1994; Ortiz et al, 1996; Sen et al., 1996; Harrington and Horseman 1999; Rodwell et al., 2000, Cuss and Harrington , 2012; Harrington et al., 2012 (i) and (ii)).

More recent work by Angeli et al. (2009) provides important new data regarding gas flow in indurated shale. These researchers performed a highly-instrumented test on a sample of Draupne shale from the Troll East Field located in the Norwegian Section of the North Sea (Figure 6-3). Inspection of the data indicates that at excess gas pressures <3.0 MPa, the sample exhibits no discernable strain or discharge from the base of the specimen[4]. However, two days after the gas pressure gradient is increased to 3.5 MPa (still well below the effective stress applied to the sample), the specimen starts to dilate, exhibiting considerable radial strain. This is then followed 5 days later by an increase in discharge rate out of the core which coincides with a reduction in radial strain of around 0.6% (the negative sign of the strain denoting an increase in sample volume), and is interpreted by the authors as the point of gas breakthrough. This is also accompanied by a notable reduction in P-wave velocity which the authors ascribe to the penetration of the sample by the carbon dioxide (which is around 2 orders of magnitude more compressible than the interstitial fluid) and to the opening of “cracks” within the shale.

From the start of dilation (day 26) to the end of the radial expansion phase (day 36) the sample undergoes a radial strain of around 1% (as a percentage of the porosity this would be significantly larger). During the following 26 days the radial strain data shows signs of time-dependent volume change with a slight reduction in value as conductive pathways within the shale are established. This mechanism may provide an explanation for the apparent over- and under-shooting of the ultimate steady-state value observed in Figure 4-22.

[4] The resolution of the second y-axis on Figure 6-3 precludes examination of the data for precursor flows.

It is also interesting to note that the evolution of strain in Figure 6-3 does not correlate with measured changes in P-wave velocity. While the authors pass no comment on this behaviour, it strongly suggests that following initial dilation and penetration of the shale by CO_2, the gas saturation within the sample continues to increase. It is unclear from the data available if this is associated with time-dependent deformation of the fabric (accompanied by drainage of interstitial fluid from the surrounding clay[5]), structural changes due to chemical alteration of the shale by the CO_2, or displacement of porewater from higher porosity zones within the shale (classic two-phase flow).

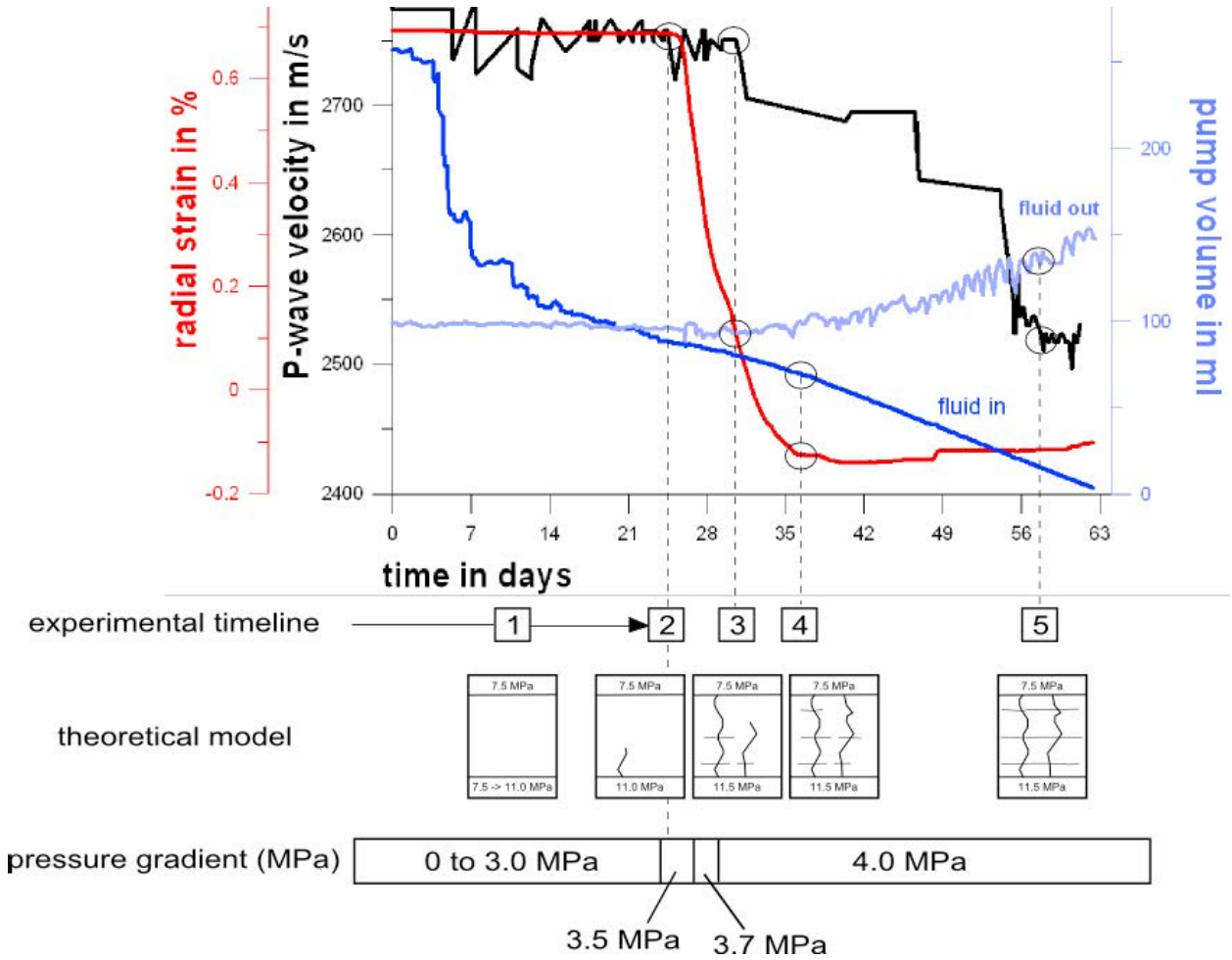

Figure 6-3 Data from Angeli et al. (2009), showing a significant change in radial strain prior to and during gas breakthrough for a test performed on Draupne shale taken from the Troll East Field in the Norwegian Section of the North Sea. The change in P-wave velocity following breakthrough is symptomatic of gas penetration of the fabric due to the change in compressibility of the CO_2 compared with that of the original porewater.

What is absolutely clear from the data is that dilatancy and time-dependent processes are key factors in the development of gas permeability within the Draupne shale. The Draupne shale has a similar clay fraction (around 40% by weight) compared to that of the Callovo-Oxfordian clay but has a significantly higher porosity (around 24%). While site specific factors will play a role in determining the multi-phase flow and hydro-mechanical behaviour of the Bure argillite, it seems highly likely that similar processes to those observed in the Draupne shale will apply. If

[5] This should not be mistaken for displacement of water through visco-capillary flow.

correct, this would explain a number of the observations reported during this experimental study and would address the apparent inability of the numerical modelling to adequately predict the system response.

7 References

British Geological Survey holds most of the references listed below, and copies may be obtained via the library service subject to copyright legislation (contact libuser@bgs.ac.uk for details). The library catalogue is available at: http://geolib.bgs.ac.uk.

ANDRA, 2009. Rapport mi-parcours pour le Groupment de Laboratoires «Transfert de Gaz». C.RP.ASCM.09.0002.

ANGELI, M., SOLDAL, M., SKURTVEIT, E. AND AKER, E., 2009. Experimental percolation of supercritical CO_2 through a caprock. *Energy Procedia* 1, 3351-3358.

CUSS, R.J., HARRINGTON, J.F. AND NOY, D.J., 2010. Large scale gas injection test (Lasgit) performed at the Äspö Hard Rock Laboratory. Summary report 2008. *Report TR-10-38*. Svensk Kärbränslehantering AB (SKB), Stockholm, Sweden.

CUSS, R.J., and HARRINGTON, J.F. (2012) Final Report of FORGE WP4.1.1: The stress path permeameter experiment conducted on Callovo-Oxfordian Claystone. *British Geological Survey Commissioned Report*, CR/12/140. 116pp.

ESTEBAN, L., BOUCHEZ, J., L. AND TROUILLER, A., 2006; The Callovo-Oxfordian argillites from the eastern Paris Basin: Magnetic data and petrofabrics, *Comptes Rendus Geosciences* **338**, pp 867-881

GALLÉ, C., 2000. Gas breakthrough pressure in compacted Fo–Ca clay and interfacial gas overpressure in waste disposal context. *Applied Clay Science*. 17 (1–2), 85–97.

GAUCHER, E., ROBELIN, C., MATRAY, J.-M., NÉGREL, G., GROS, Y., HEITZ, J.-F., VINSOT, A., REBOURS, H., CASSAGNABÈRE, A. AND BOUCHE, A. T, 2004. ANDRA underground research laboratory: interpretation of the mineralogical and geochemical data acquired in the Callovo-Oxfordian formation by investigative drilling, *Phys. Chem. Earth* **29**, pp. 55–77.

HARRINGTON, J.F. AND HORSEMAN, S.T., 1999. Gas transport properties of clays and mudrocks. In. Aplin, A.C., Fleet, A.J. and Macquaker, J.H.S. (eds) Muds and Mudstones: Physical and Fluid Flow Properties. *Geol. Soc. London, Spec. Pub.* 158, 107-124.

HARRINGTON, J.F. AND HORSEMAN, S.T., 2003. Gas migration in KBS-3 buffer bentonite: Sensitivity of test parameters to experimental boundary conditions. *Report TR-03-02*. Svensk Kärbränslehantering AB (SKB), Stockholm, Sweden.

HARRINGTON, J.F. MILODOWSKI, A.E., GRAHAM, C.C., RUSHTON, J.C. and CUSS, R.J. (2012 (i)). Evidence for gas-induced pathways in clay using a nanoparticle injection technique. Mineralogical Magazine, Vol. 76(8), pp3327-3336.

HARRINGTON, J.F., de La VAISSIERE, R., NOY, D.J., CUSS, R.J. and TALANDIER, J. (2012 (ii)). Gas flow in Callovo-Oxfordian Clay (COx): Results from laboratory and field-scale measurements. Mineralogical Magazine, Vol. 76(8), pp. 3303-3318.

HORSEMAN, S.T. AND HARRINGTON, J.F., 1994. Migration of repository gases in an overconsolidated clay. *British Geological Survey, British Geological Survey*, Technical report WE/94/7.

HORSEMAN, S.T., HIGGO, J.J.W., ALEXANDER, J. AND HARRINGTON, J.F., 1996. Water, gas and solute movement in argillaceous media. Rept. No. CC-96/1 to OECD/NEA Working Group on Measurement and Physical Understanding of Groundwater Flow through Argillaceous Media. Nuclear Energy Agency, OECD, Paris.ISBN 92-64-1488-1.

HORSEMAN, S.T., HARRINGTON, J.F. AND SELLIN, P., 1996. GAS migration in Mx80 buffer bentonite. In: Symposium on the Scientific Basis for Nuclear Waste Management XX (Boston), *Materials Research Society*, Vol. 465. 1003-1010.

HORSEMAN, S.T. AND HARRINGTON, J.F., 1997. Study of gas migration in Mx80 buffer bentonite. British Geological Survey, Technical Report WE/97/7.

HORSEMAN, S.T., HARRINGTON, J.F. AND SELLIN, P., 1999. Gas migration in clay barriers. In: Pusch, R. and Yong, R.N. (eds) Microstructural Modelling of Natural and Artificially Prepared Clay Soils with Special Emphasis on the Use of Clays for Waste Isolation (1999 Special Edition), *Engineering Geology*, Vol 54, pp 139-149, Elsevier, Amsterdam.

HUYAKORN, P.S. AND G.F. PINDER, 1983, Computational methods in subsurface flow. Academic Press.

INTERA ENVIRONMENTAL CONSULTANTS INC., 1983, STAFAN: A Two-Dimensional Code for Fluid Flow and the Interaction of Fluid Pressure and Stress in Fractured Rock for Repository Performance Assessment. *Office of Nuclear Waste Isolation Report ONWI 427*.

MARSILY, G. DE, 1986, Quantitative Hydrogeology for Engineers, *Academic Press*.

Ortiz, L., Volckaert, G., Mallants, D., 2002. Gas generation and migration in Boom Clay, a potential host rock formation for nuclear waste storage. *Engineering Geology* 64 (2–3), 287–296.

ORTIZ, L., VOLCHARET, G., DE CANNIERE, P., AERTSENS, M., HORSEMAN, S.T., HARRINGTON, J.F., IMPEY, M., AND EINCHCOMB, S. (1996). MEGAS - Modelling and Experiments on Gas Migration in Repository Host-rocks. Proc. EU PEGASUS Meeting at Rapolina-Terme, Italy, 14-15 June 1995. *Nuclear Science and Technology Series*, EUR 16746 EN, Luxembourg, 127-147.

PRUESS K., OLDENBURG C., MORIDIS G., 1999. TOUGH2 user's guide, version 2.0. *Lawrence Berkeley National Laboratory report* LBNL-43134.

RODWELL, W.R. (ED.), 2000, Research into Gas Generation and Migration in Radioactive Waste Repository Systems (PROGRESS Project). *Nuclear Science and Technology* EUR 19133 EN, European Commission, Luxembourg.

ROUSESET, D. AND CLAUER, N., 2003; Discrete Clay Diagenesis in a Very Low-Permeable Sequence Constrained by an Isotopic (K-Ar and Rb-Sr) Study, *Contributions to Mineralogy and Petrology*, **145**, pp 182-198.

SEN, M.A., HORSEMAN, S.T. AND HARRINGTON, J.F., 1996. Further studies on the movement of gas and water in an overconsolidated clay: Contribution to MEGAS Phase 2 Report (PEGASUS Project). *British Geological Survey, Technical Report* WE/96/8 To: Commission of European Communities (CEC), Brussels.

VAN GENUCHTEN M.TH., 1980. A Closed-Form Equation for Predicting the Hydraulic Conductivity of Unsaturated Soils, *Soil Sci. Soc*., Vol. 44, pp. 892 – 898.

WENK, H.-R., VOLTOLINI, M., MAZUREK, M., VAN LOON, L.R. AND VINSOT, A., 2008, Preferred Orientations and Anisotropy in Shales: Callovo-Oxfordian Shale (France) and Opalinus Caly (Switzerland), *Clays and Clay Minerals*, **56**, pp 285-306.

WILEVEAU, Y., AND BERNIER, F. 2008. Similarities in the hydromechanical response of Callovo-Oxfordian clay and Boom Clay during gallery excavation. *Physics and Chemistry of the Earth*, 33, S343–S349.

ZHANG, C-L, ROTHFUCHS, T., SU, K., AND HOTEIT, N. 2007. Experimental study of the thermo-hydro-mechanical behaviour of indurated clays. *Physics and Chemistry of the Earth*, 32, 957–965.

.